Toward Reproducible Domain-Wall Conductance in Lithium Niobate Single Crystals

Master-Arbeit
zur Erlangung des Hochschulgrades
Master of Science
im Master-Studiengang Organic and Molecular Electronics

vorgelegt von

Iuliia Kiseleva

Institut für Angewandte Physik
Fakultät Physik
Bereich Mathematik und Naturwissenschaften
Technische Universität Dresden
2023

Eingereicht am 03.01.23

1. Gutachter: Prof. Dr. Lukas M. Eng

2. Gutachter: Prof. Dr. Holger Fritze

Abstract

Conductive domain walls (DWs) in lithium niobate ($LiNbO_3$, LNO) are promising constituents for potential applications in nanoelectronics, due to their high conductance, as compared to the surrounding bulk material, their high local confinement at the nanometer scale, and the ability to be created quasi-on-will through dedicated high-voltage poling. However, electrically contacting the DWs unavoidably leads to the formation of a potential barrier between the DW itself and the electrode material. Thus, the focus of this work is the investigation of the various factors influencing the electronic transport across that barrier, namely, the type of electrode material, the quality of the LNO surface (atomically-smooth versus mirror polished), the quality of the crystal lattice (i.e., the presence of higher concentrations of lithium and oxygen vacancies V_{Li} and V_O), and the magnitude of the applied voltages during the domain-wall conductivity (DWC) enhancement procedure.

It is found that all the above-mentioned factors have a significant impact on the current-voltage characteristics of the DW-electrode system. For example, the metal electrodes deposited onto the surface of the LNO crystal, once, impede the DW motion, while, secondly, stabilizing the DWs inclination across the LNO crystal. Another important finding is the major role played by large negative voltages in the DWC-enhancement procedure that strongly influences the near-surface structure of the DW, and hence the qualitative characteristics of the formed potential barrier, such as characteristic voltage and saturation current. The application of moderate voltages from – 50 V to – 100 V is also found to influence the structure of the near-surface DW. The creation of a variety of vacancy defects inside the bulk LNO that accompanies the formation of an atomically-smooth surface, is found to have far more influence on the DW charge transport than the quality of the surface, due to the formation and repulsive interaction of a multitude of spike domains stemming from these defects.

In summary, the results demonstrate the importance of providing known and reproducible sample surface conditions and identifying promising directions for implementing reproducible domain wall conductivity.

Contents

1 Introduction **7**
2 Theoretical Background and Literature Review **9**
2.1 Physicochemical Properties of Lithium Niobate Single Crystals 9
2.1.1 Domain Walls in Lithium Niobate 10
2.1.2 Equivalent Circuits for Systems with Lithium Niobate Domain Walls 12
2.2 Metal-Semiconductor Junctions 16
2.2.1 Formation of Schottky Contacts 16
2.2.2 Transport Mechanisms Across a Schottky Barrier 18
2.3 Surface Properties of Lithium Niobate 21
2.3.1 +Z- and –Z-Surface Reconstruction 21
2.3.2 Practical Processing Methods of Lithium Niobate Surfaces 23
2.4 Geometrical Structure of Domain Walls Near the Surface 25
2.5 Electronic Transport in Lithium Niobate 27
2.5.1 DC Conductivity and Transport Mechanism 27
2.5.2 Temperature Influence on Electronic Transport in LNO Domain Walls 27
2.5.3 Application of AC Measurements for Charge Transport Investigations 31
3 Experimental Methods and Setup **35**
3.1 Lithium Niobate Samples and Sample Preparation Process 35
3.2 Experimental Setup for Domain Inversion and Poling Protocol 35
3.3 Deposition of Metal Electrodes and Enhancement of the Domain Wall Conductivity ... 38
3.4 Annealing Procedure of Lithium Niobate Crystals 38
3.5 Setup for DC Measurements at Room and Lower Temperatures 39
3.6 AC Measurements 40
4 Results and Discussion **41**
4.1 DC Conductance of Domain Walls and Circuit Characteristics 41
4.2 Reproducibility of the Domain Walls Produced with Laser-Assisted Poling 50
4.3 Electrode Re-Deposition Influence on the Schottky Barrier 56
4.4 Electrode Influence on the Processes of Poling, DWC Enhancement, and Charge Transport 60
4.4.1 Influence of the Electrode Material on the Schottky Barrier Parameters 60
4.4.2 Poling of the DW with a Deposited Electrode 65
4.5 Influence of the Lithium Niobate Surface Quality on the Characteristics of the Schottky Barrier 68

5 Summary and Outlook **75**
Appendix **79**
A1. Pre-enhancement IV curves of the samples used in this work 79
A2. Temperature-Dependent DC Conductance 81
A3. Higher-Harmonic Current Generation in Domain Wall Structures 85
References **91**
Acknowledgment **99**
Eidesstattliche Erklärung **100**

1 Introduction

Domain Walls (DW) in a ferroelectric crystal are interfaces of down to only a few unit cells in width, which separate regions of different orientations of dielectric polarization, and show physical properties that are drastically different from those of the surrounding (bulk) material [1]. Along with certain functional chemical [2], mechanical [1], magnetic [3], and optical properties [4], one of the main sources of interest for industrial application are the altered electrical properties of the DWs. Due to their confined nature and, in some cases, high conductivity, DWs can form 2D electron systems [5]. Coupled with the possibility to engineer and modify DW structures, this fact allows for the creation of nanocontacts and conductive paths on the nm-length scale [6] in the surrounding isolating material in the fields of data storage, energy harvesting, and nanoelectronics [7].

An example of a material that is best suited for such purposes is lithium niobate ($LiNbO_3$, LNO), one of the most investigated ferroelectric materials [7]. Due to its high Curie temperature [1], thermal and chemical stability [8], easy fabrication of high-quality crystals, and variety of functional physical properties (piezo- and pyroelectricity, acoustic, non-linear optical, and electro-optical properties) [1], LNO crystals have multiple applications in wave guides [9], microwave filters [10], in nonlinear optics (second-harmonic generation) [11] or non-volatile memories [12], to name a few. The spontaneous polarization in LNO is directed along the crystallographic ±z (also referred to as ±c) axis of hexagonal unit cell and, consequently, exclusively 180° domain walls can be formed on the atomic. Being an insulating ferroelectric with a wide bandgap of around 4 eV and low optical damage, LNO is one of the best known materials for domain-wall conductivity (DWC) investigations [13]. DWC in lithium niobate was discovered in 2012 [14]. It was also found that non-zero inclination of domain wall α relative to the z-axis was imperative for the existence of the high DW conductance. Within a simples approximation, a proportionality of the conductance to $\sin(\alpha)$ is expected. Subsequently, a method for DWC enhancement by three to four orders of magnitude by using high-voltage biasing was proposed by Godau et al. [6].

The current-voltage characteristics of the system, consisting of plate metal electrodes in contact with the inclined DW, obtained by the above-described DWC enhancement method, tend to demonstrate several features: firstly, at low voltages near zero, the dependence has non-linear, diode-like behavior; secondly, at higher voltages, the dependence becomes linear, and thirdly, IV-curve is asymmetrical with respect to the voltage polarity. For the description of the electrical behavior of such a system, Manuel Zahn has proposed in his Master's thesis [15] the equivalent circuit model, consisting of two parallel diodes in opposite voltage polarities, each connected in series to resistors,

describing the forward and backward behavior. Such a model characterizes the DWC-electrodes system by six parameters: resistance values R for the resistors, values of saturation current I_s, and the so-called characteristic voltage U_c for diodes in forward and backward directions. This allows fitting the obtained IV-curves with excellent accuracy [15] with the consequent obtainment of these parameters, which makes possible an investigation of the reproducibility of domain walls using methods of production and enhancement proposed by Godau et al. [6] with subsequent categorization – bidirectional or rectifying. Additionally, it was established that field emission is the main mode of electron transport trough the Schottky contact. Such studies allow a quantitative characterization of the investigated devices, and, consequently are a great help in the research of production parameters' influence (e.g., magnitude of the electric field, time of electric-field application, etc.) on the domain wall-metal contact electrodes system and finally, on its electrical characteristics.

The formed Schottky barriers also present a great deal of scientific interest; considering the possibility to form, erase, and modify DWs [16] and their dielectric, electronic, and electromechanical properties. Prospective applications for the lithium niobate DWs as a conductive paths between the elements of highly planar integrated circuits or as a rectifying element of the circuit is of a great significance. In the same work, temperature-dependent DC conductivity measurements were conducted; for the intrinsic DW conductivity thermally activated conduction mechanism was established.

In this work additional DC (Direct Current) conductivity measurements at low temperature will be presented. In Chapter 2 of this work, theoretical background on the lithium niobate properties, the Schottky barrier formation, AC and DC transport along DWs (including low temperature transport) is introduced. Chapter 3 contains the description of the setups that were used in the course of this work. In Chapter 4, the results of the research are presented: reproducibility of the lithium niobate domain walls covered with the planar electrodes in the UV-laser assisted poling setup is presented. The effect of the lithium niobate surface quality on the formed Schottky barrier was investigated and is also presented in Chapter 4; the clean, atomically smooth surface close to ideal was achieved by high-temperature annealing. The influence of electrode material on the formed domain walls was also studied; the role the metal electrode plays during the poling and DWC enhancement process as compared to the liquid electrode, is also presented. Chapter 5 contains the summary of all these results obtained during the course of this work as well as an outlook on the further investigation that should bring close the practical application of the studied system.

2 Theoretical Background and Literature Review

2.1 Physicochemical Properties of Lithium Niobate Single Crystals

$LiNbO_3$ is an artificial material that does not occur in nature; first it was synthesized at Bell Laboratories in 1949 and was discovered to be a ferroelectric with a Curie temperature of approximately 1210 °C [17]. The crystal structure of the material in its para- and ferroelectric states is presented in Fig. 1. In the paraelectric phase, the crystal consists of oxygen atoms (white circles) in a distorted hexagonal close-packed configuration; interstices of this matrix are periodically filled with lithium atoms (black circles in oxygen layer), niobium atoms (red circles between oxygen layers) and vacancies in equal proportion. For temperatures below the Curie point, niobium and lithium atoms are forced into new positions by elastic forces of the crystal, thus LNO is classified as displacement ferroelectric. In the electric phase the crystal belongs to the 3m point group and the rhombohedral R3c space group [18]. Dislocations of Li and Nb atoms take place only along the crystallographic c-axis (also designated as z-axis or [0 0 0 1]), thus the formation of c+ and c- sides of the crystal with a permanent dipole moment of 75 - 80 $\mu C/cm^2$ [19] occurs.

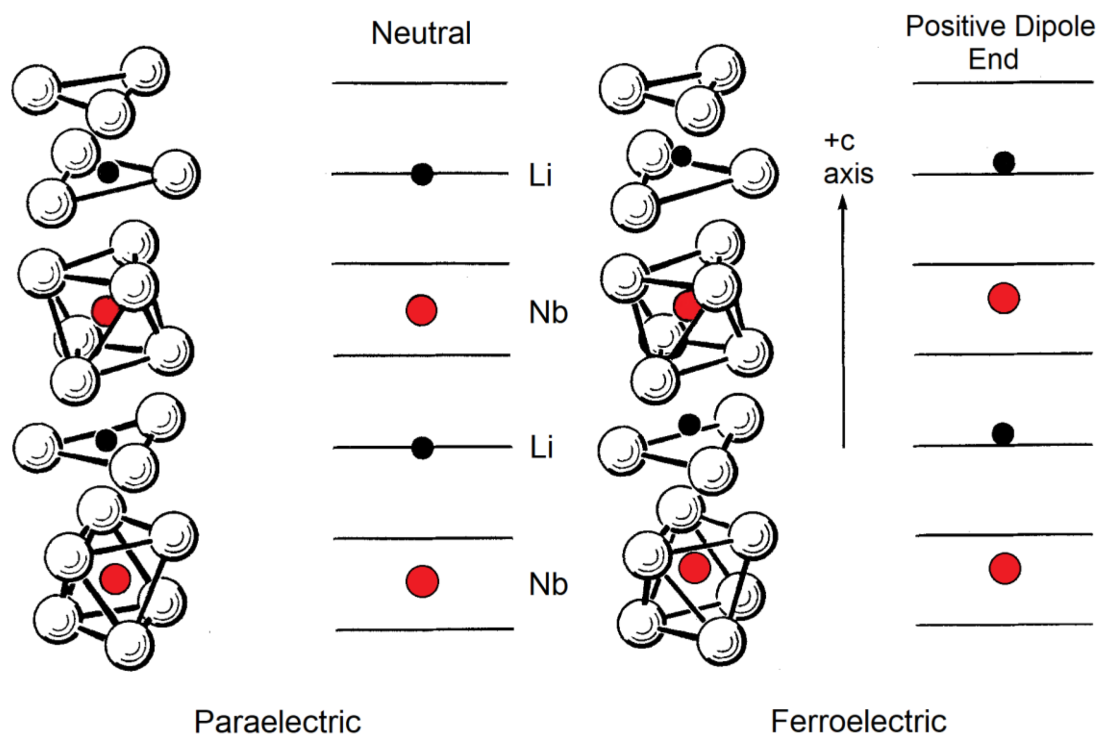

Figure 1. Crystal structure of lithium niobate. Oxygen atoms are represented by white circles, lithium atoms are represented by black circles, niobium atoms are represented by red circles. Reproduced from [17] with changes.

LNO crystals are industrially grown by the Czochralski method from the melt of Li_2O and Nb_2O_5; their proportion can be varied from 47 to 49 mol% of Li_2O [20]. The most prevalent compositions are stochiometric ([Li]/([Li] + [Nb]) = 0.5) and congruent ([Li]/([Li] + [Nb]) = 0.484). The latter, due to fast growth and better homogeneity, is the most commonly used, although due to lithium deficiency it demonstrates higher concentration of vacancies (V_{Li}) and anti-site defects (Nb_{Li}). Adding ~ 5 % MgO to the congruent melt reduces the number of V_{Li} and Nb_{Li}, defects and the properties of this composition are close to the stochiometric case (less defects, hence higher quality lattice); the addition of Mg^{2+} ions also increases the conductivity of the domain walls due to larger inclination angles α [14, 21] and provides high optical damage threshold, which is very important for optical modulators. In this work, only samples made of Mg:LNO are investigated.

LNO is a highly inert substance from the chemical point of view; only very few chemicals, including HF, mixtures of HF and HNO_3, and H_3PO_4 are used for wet etching [20]. Even at the boiling points, the etch rates for these reactants are several nm/min [22]. The –c-side is more reactive than the +c-side, and also defects increase the rate of reaction [2].

2.1.1 Domain Walls in Lithium Niobate

As was pointed out earlier, cations in the crystal lattice can be displaced only along the c-axis. Consequently, typically 180° domains can be formed [23]. The conductivity of domain walls with different inclination angles was investigated comparatively; it was found out that only domain walls with non-zero inclination are conductive [14]; the conductance of the head-to-head (h2h) DWs is at least 10 times higher than that of tail-to-tail (t2t) DWs (Fig. 2) [13]. Such phenomena are explained by the accumulation of screening mobile charges (electrons) on the positively charged interface of neighboring domains.

The following relation between inclination angle α and surface charge density σ was proposed:

$$\sigma = 2P_s \sin\alpha, \tag{1}$$

where P_s denotes the spontaneous polarization of LNO. The conductivity is thus directly proportional to sinα [13]. It was also demonstrated that the conductive path lies inside the domain walls since the current is only detected when both electrodes are contacted to a DW. The measured current on as-grown DWs was of the order of 10 pA at voltages below 10 V under UV illumination; current-voltage (IV) curves demonstrated the ohmic (bidirectional) behavior of DWs. IV curves

also showed a dependence on the electrode material – this can imply the formation of a Schottky contact between the electrodes and the DW [24].

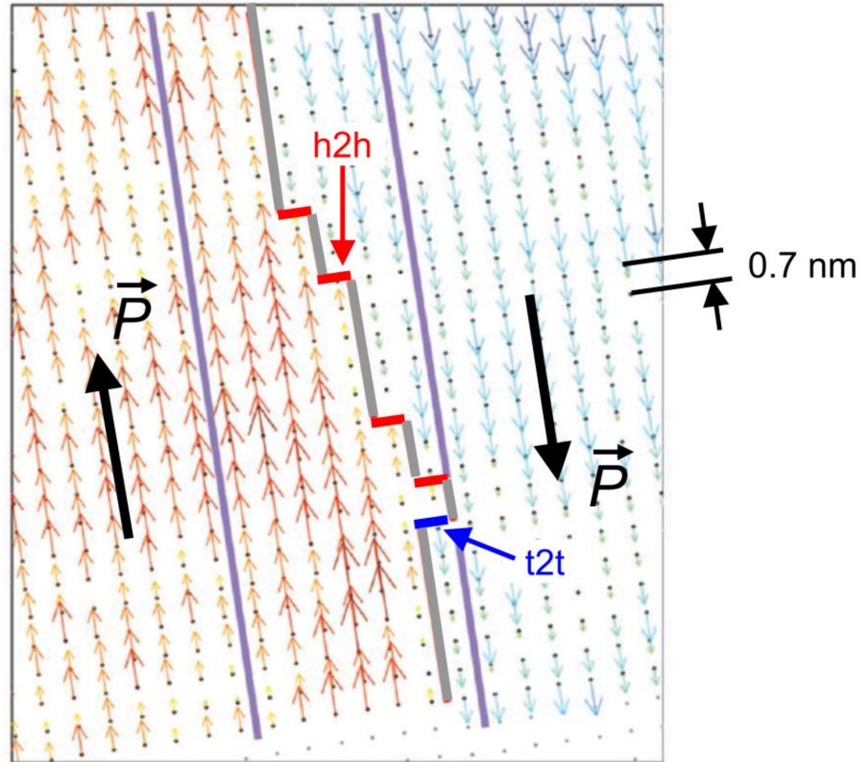

Figure 2. Image of the Nb sublattice in LNO made with high angular annular dark field transmission electron microscopy (HAADF-TEM) in the vicinity of the domain wall (the region roughly defined inside the two purple lines) that separate two regions with opposite spontaneous polarization (marked with large black arrows). Value of Nb atoms' displacement allows the calculation of the polarization in each individual unit cell. The DW on the image is not inclined, consequently on average it is neutral (grey lines signify the neutral "lateral" interface between the unit cells). Head-to-head (h2h) contact has the largest positive charge between the unit cells (in red), tail-to-tail (t2t) signifies the largest negative charge between the unit cells. Reproduced from [23].

Subsequently, a method for DWC enhancement by three to four orders of magnitude was proposed by Godau et al. [6]. After the creation of DWs with UV-laser and high electric-field poling, moderate electric fields up to 10^4 V/cm were applied to the z- side of the DW. That method allows to reproducibly move and bend DWs (to both positive and negative values of α) and thus form the conductive paths between two chromium electrodes. Consequently, the detection of a current requires no more illumination and the signal-to-noise ratio becomes acceptable; the current is increased by several orders of magnitude. The charge transport through the electrode-DW contact depends on the electrode material, and for example with a chromium electrode, the contact forms a Schottky barrier (although there is some conflicting evidence concerning this material [24]; in case the domain inversion occurs in the presence of the Cr electrode, the contact formed can show a bidirectional linear IV-curve). For the description of the electric characteristics of such a system,

which demonstrates non-linear (diode-like) behavior at low voltages, linear (ohmic) behavior at larger voltages, and asymmetricity in relation to the polarity of the voltage, an equivalent circuit, consisting of two diodes, representing the Schottky barriers between CDW and contact chromium electrodes, and two resistors, representing the intrinsic DW conduction (Fig. 3), was proposed.

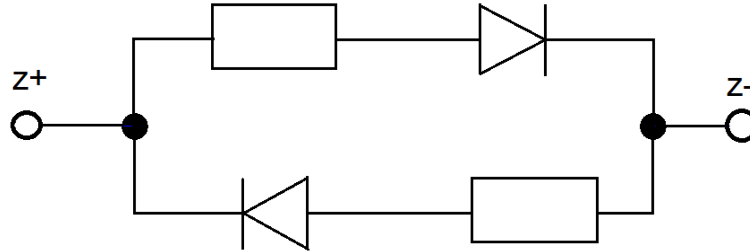

Figure 3. The equivalent circuit proposed by Zahn [15] for interpretation of IV-curves of the DW-Cr electrode system.

2.1.2 Equivalent Circuits for Systems with Lithium Niobate Domain Walls

The circuit, suggested by Zahn, is not the first alternative circuit, proposed in the literature. One of the examples, that stands somewhat asides from the others, is a two-dimensional Resistor Network (2D RN) system, consisting of hundreds of resistors, whose resistance values depend on the local inclination angle α, suggested by Wolba et. al [13] (Fig. 4(b)). Unlike other alternative circuits, the 2D RN was suggested for the purpose of modelling the intrinsic charge transport inside the LNO domain wall (and not as an element of a larger device) and does not take into account non-linear effects, stemming from DW-metal interfaces (although boundary conditions for the cases of two metal plate electrodes and metal tip-metal plate electrodes was used for the solution of the Kirchhoff equation).

In Fig. 4(a), a “world map” view of the tuned DW, obtained by Cherenkov-Second-Harmonic Generation (CSHG) microscopy is depicted. Azimuthal angle φ is unrolled along the x-axis, and local inclination angle α of the DW is color coded. Under the assumption that $\sigma = \sigma_0 \cdot \sin\alpha$ and that for h2h DWs (marked in red) σ_0 is ten times larger than for t2t DWs, each region of the DW can be represented by a resistor with a respective resistance value (Fig. 4(b)). For more than 45000 resistors the model gives good results, and, consequently, allows to make predictions on the intrinsic conductivity based on the CSHG inclination angles.

Other equivalent circuits were proposed on the basis of AC frequency-dependent macroscopic impedance measurements – with two metal-plate electrodes [25] and the metal tip-plate electrode system [1]. Both of the suggested systems take into account non-linear electrical properties of the contact between the domain wall and the metal electrode, and describe them with RC-circuits. In

Fig. 5(a) an analogous circuit for multidomain LNO between two metal plates is presented. In this scheme, a low-pass RC filter represents the capacitor formed by two plate electrodes and LNO crystal (without influence of DWs, “Bulk” frame in Fig. 5(a)); it was suggested on the basis of the AC measurements of the single-domain sample. The DWs in contact with metal electrodes is described here as constant phase element (CPE_{DW}) in series with a capacitor (C_{DW}). On a microscopic level, CPE can be presented as a serial combination of RC circuits, each corresponding to a unit cell in the DW with its individual capacitance and resistance, depending on the local inclination angle.

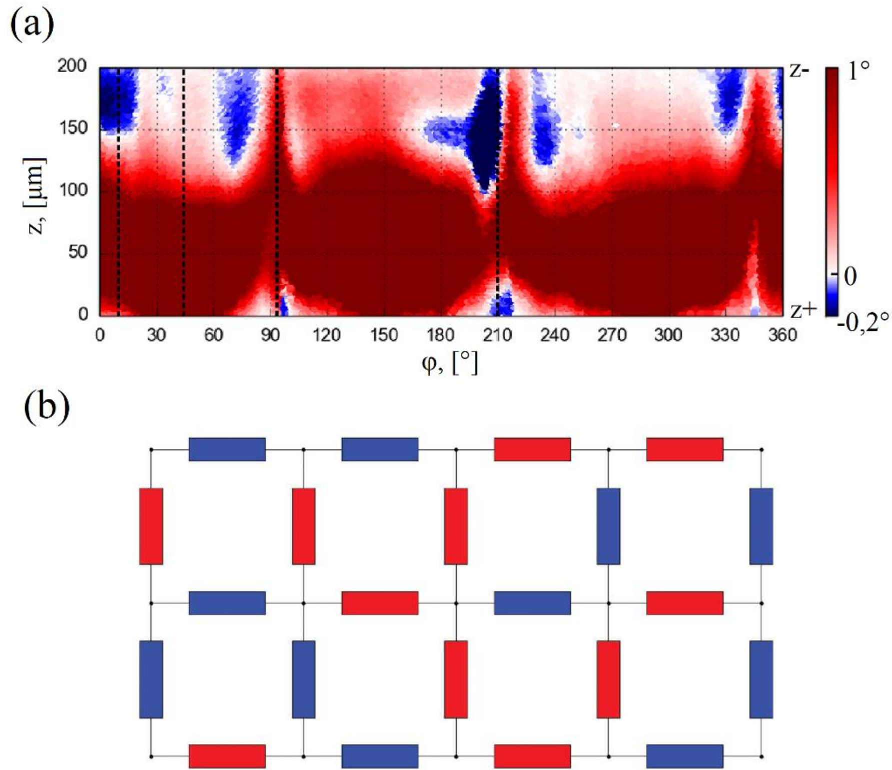

Figure 4. (a) “World Map” of a “tuned” domain wall obtained by CSHG microscopy. Vertical axis corresponds to the z-coordinate of the wall, while the horizontal axis corresponds to the polar angle ϕ in cylindrical coordinates. The inclination angle α of the domain wall is color-coded – red for h2h DWs and blue for t2t DWs. As seen from the image, after DWC tuning, the domain wall mostly consists of h2h segments (in red). (b) Equivalent circuit consisting of a resistor network, where the resistance of each resistor is proportional to sinα. This model allows to predict intrinsic DW conductivity based on the CSHG image (a). Reproduced from [13].

Another system with a tip of AFM probe as electrode was suggested by Schultheiß et al [1]. It is very similar to the previous one in the sense that it also consists of RC circuits, however, in a slightly different configuration. In Fig. 5(b), tip-sample system and corresponding equivalent circuit are presented; the two main impedance contributions are highlighted in the dashed boxes.

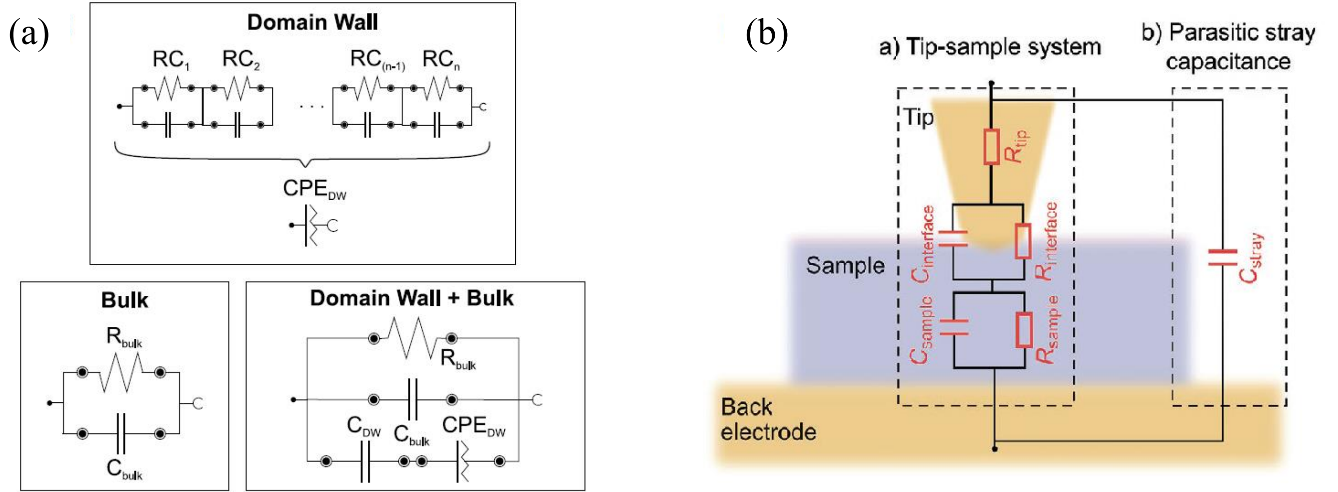

Figure 5. (a) Equivalent circuit of a LNO sample and two metal plate electrodes suggested by Schröder et al. Intrinsic conductivity of the DW is represented by the constant phase element (CPE), consisting of multiple RC circuits, with resistors and capacitors connected in parallel, with R and C depending on the local DW inclination, connected in series. The interface between DWs and electrodes can be presented as a capacitor, and LNO bulk covered with eletrodes is a simple RC circuit. Reproduced from [25]. (b) Equivalent circuit suggested by Schultheiß et al. for tip-interface contact. In this circuit two main impedance contributions exist: firstly, the parasitic stray capacitance, produced by the AFM cantilever, and secondly, tip-interface contact (of the tip with resistance R_{tip}), presented as the parallel RC circuit, and bulk contribution with the same RC circuit representation. Reproduced from [1].

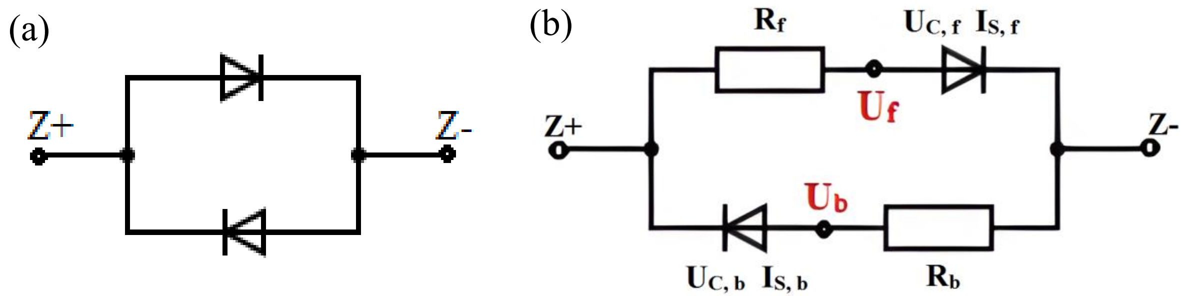

Figure 6. (a) Equivalent circuit suggested by Zhang et al. [26], for DW between two Pt electrodes, consisting of two parallel diodes with opposite polarity. (b) Equivalent circuit model, suggested by Zahn [15] for multidomain LNO with plate Cr electrodes, consisting of two parallel pairs of resistor and diodes with opposite polarity. Resistors represent the intrinsic resistance of the DW, signified as R_f and R_b (forward and backward), and diodes signify contact between the DW and metal electrodes with corresponding characteristics of saturation current I_S and characteristic voltage U_C.

The first contribution is the tip-sample system itself; it consists of the AFM tip with resistance R_{tip}, the tip-interface contact is a Schottky barrier, being analogous to a leaky capacitor, and represented by the RC circuit including $R_{interface}$ and $C_{interface}$ in parallel; the intrinsic impedance of a sample is determined by the geometrical size of the sample and can also be represented by a RC-circuit with R_{sample} and C_{sample} in parallel. All these sub-systems are connected in parallel (see Fig. 5(b)). The second contribution is the parasitic stray capacitance C_{stray}, originating from the cantilever of the atomic force microscopy (AFM). Its contribution to the impedance is usually significantly larger (~ eight orders of magnitude) than that of the tip-sample system. Presence of

this stray capacitance is a common problem in scanning probe microscopy; usually it should be suppressed, for example, by including a compensating RC circuit in the chain.

Another approach was taken by Zhang et al. [26]. Here, the suggested analogous circuit contains diodes instead of the RC circuits, used to describe the non-linear IV-properties. DC and AC current measurements for a mesa-like memory cell in x-cut LNO have demonstrated full-wave rectification in the device and a circuit consisting of two parallel diodes of opposite polarity was suggested, see Fig. 6(a). Another very similar alternative circuit was suggested by Werner at el. [24]. Here, a periodically-poled LNO crystal, created with c-AFM (method of calligraphic domain writing) with silver electrodes on the –z-side of the LNO crystal and chromium electrodes on the +z-side of the crystal is represented by the alternative circuit in the Fig. 7. The bottom chromium electrodes were deposited before the poling process; the contact between them and the DWs is represented by resistors. Silver paste was deposited on the top of the crystal after domain inversion; silver-DW contact here act as the diode. Intrinsic conductivity of the DWs has a linear IV-curve characteristics, and, consequently, can be represented as a simple resistor. Interestingly enough, after the removal of the initial Cr electrodes and deposition of new Cr electrodes, Cr-DW contact loses its linear characteristics and becomes diode-like.

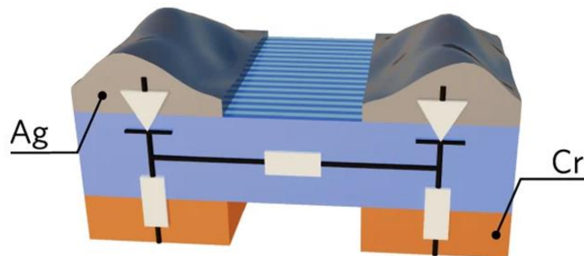

Figure 7. Alternative circuit, suggested by Werner at el. for the multidomain LNO crystal (sixteen 13-mm-long domain lines, marked in blue and light blue on the surface of the crystal), covered with Cr electrodes on the +z-side of the crystal before the poling procedure and with silver paste on the other side after the poling procedure. Based on the IV-curves obtained with the current measurements between two varying electrodes (e.g., using only two bottom Cr electrodes, or one Ag upper electrode and one bottom Cr electrode, and so on), this circuit was suggested. It should be noted, that after the re-deposition of the Cr electrodes, the character of the Cr-DW contact changes from ohmic to diode-like. Reproduced from [24].

As was mentioned earlier, an equivalent circuit very similar to the one suggested by Zhang [26], was proposed by Zahn [15]. Here, besides two parallel diodes of opposite polarity (and with saturation current I_S and characteristic voltage U_C corresponding to each of the diodes in forward and backward directions), two resistors were added, see Fig. 6(b). As we will see later, the

contact between a metal and DW strongly influences current-voltage characteristics of such a device, both resistance values and diode characteristics, such as I_S and U_C. Thus, in the next section formation and properties of the Schottky barrier at the DW-metal-electrode interface, which is the physical origin of the diode behavior, will be discussed.

2.2 Metal-Semiconductor Junctions

2.2.1 Formation of Schottky Contacts

When a contact is formed between a metal and a semiconductor surface, Fermi level alignment of both materials happens. Depending on various properties such as the work function of the metal φ_m, electron affinity of the semiconductor χ, doping concentration of the semiconductor N_d, and several other properties [27], either a rectifying (also named *Schottky* contact) or a non-rectifying (with linear current-voltage characteristics), also named *Ohmic* contact can be formed.

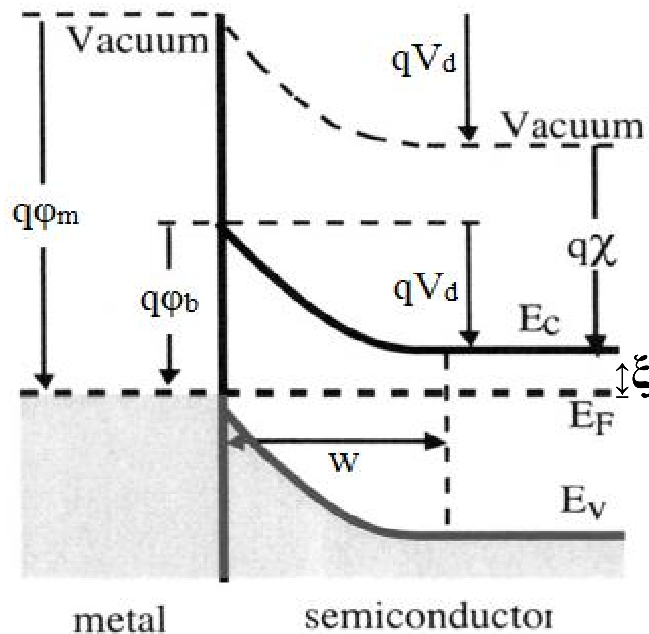

Figure 8. Energy level diagram of the Schottky contact between a metal and n-doped semiconductor; ϕ_m – metal work function, χ – electron affinity of semiconductor, ϕ_b – height of the potential barrier, V_d – diffusion voltage (or band bending), ξ – energy difference between the conduction band E_C and Fermi energy E_F, w – width of the space charge layer. Image reproduced from [28].

In Fig. 8, the energy level diagram of the Schottky contact between a metal and a n-doped semiconductor is depicted; the metal work function φ_m is larger than semiconductor work function $\varphi_s = \xi + \chi$ (the most relevant case in practice [28]). This case is very similar to the p-n junction; upon contact electrons from the semiconductor flow into the metal due to difference in the Fermi levels in materials, and thus a depletion layer is formed (comparable in size with the one in a p-n junction); in thermal equilibrium electrostatic diffusion and movement under electrostatic field of

the barrier are mutually compensated. As can be seen from the energy band diagram, the height of the barrier has the following form:

$$\varphi_b = \varphi_m - \chi. \qquad (2)$$

The situation described above is an ideal one; in most real cases the height of the barrier is not described by eqn. (2). Interfering factors such as the presence of surface states on the materials (due to the existence of crystal defects), the presence of a thin dielectric layer at the interface (SiO_2 on silicon, for example), interdiffusion or even chemical reaction between the materials can have the effect, that φ_b will be fairly insensitive to the value of φ_m. If all these contributions are taken into account, the height of the barrier can be calculated according to the eqn. (3), as it is presented by Rhoderick and Williams [27]:

$$\varphi_b = \varphi_b^0 + \frac{\varphi_1}{2} - \left\{\varphi_1\left(\varphi_b^0 + \frac{\varphi_1}{4} - U - \xi - \frac{k_B T}{q}\right)\right\}^{1/2}, \qquad (3)$$

where $\varphi_b^0 = \frac{\varepsilon_i}{\varepsilon_i + q\delta D_s}(\varphi_m - \chi) + \left(1 - \frac{\varepsilon_i}{\varepsilon_i + q\delta D_s}\right)\left(E_g - \varphi_0\right)$ and $\varphi_1 = \frac{2qN_d\delta^2\varepsilon_s}{(\varepsilon_i + q\delta D_s)}$.

In this case, the existence of a dielectric layer of width δ and dielectric constant ε_i is assumed; also, the presence of surface states of density D_s (per unit area per eV; and assumed to be constant) and neutral level φ_0 of surface states is taken into account; ε_s is the permittivity of the semiconductor. As can be seen, the expression has a complex form and the barrier height is dependent on the applied external voltage U. For a high density of surface states, the barrier height ceases to be a function of the φ_m and becomes equal to $E_g - \varphi_0$. It is said, that a "pinning" of the Fermi level occurs. An increase of the doping concentration N_d of the semiconductor leads to the decrease of the potential barrier φ_b.

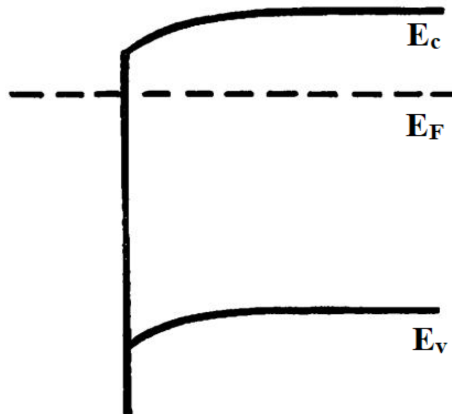

Figure 9. Energy diagram of n-doped semiconductor and metal junction in case of $\phi_s > \phi_m$ (Ohmic case). Reproduced from [27].

Considering the influence which interface defects have on a Schottky barrier, semiconductor technology processes strive to utilize only these processes that will lead to formation of so-called *intimate* contact; such a contact can be produced only under high vacuum conditions by cleaving the crystal. Molecular beam epitaxial growth is also one of the methods for creation of atomically-clean semiconductors. It is also desirable for a metal film to be epitaxial, and, consequently, highly ordered. However, it is not always the case, since deposited metal layers often tend to be polycrystalline. Even under these conditions, metal and semiconductor surfaces will be changed after contact; besides possible interdiffusions and chemical reaction, other intrinsic effects may take place, such as penetration of metal atom orbitals into the semiconductor bandgap in form of an evanescent wave function, so-called metal induced gap states (MIGS). All in all, formation of the Schottky barrier close to ideal is very tricky and thus requires highly sophisticated technological processes [29].

If we have materials, for which the semiconductor work function φ_s is larger than φ_m, no barrier will form upon contact, see Fig. 9. In this case, under both forward and reverse voltage, the contact will exhibit linear IV-characteristics and the current will be determined by a bulk resistance of the semiconductor. In industry such contacts are obtained using a very high concentration of donor atoms in the semiconductor. No energy barrier exists in the interface in such a case, and electrons moving under the bias ±U encounter no contact resistance. For lithium niobate DWs, where the majority charge carriers are electrons thermally excited to the bottom of the conduction band (as was proved by Zahn in his work [15] by thermal measurements), we can assume that for the majority of the samples studied in this work the case of $\varphi_m > \varphi_{DW}$ is relevant.

2.2.2 Transport Mechanisms Across a Schottky Barrier

Two of the main possible conduction mechanisms through the barrier are thermionic emission and field emission. In the Fig. 10(a) transport properties of the Schottky barrier are schematically represented.

Thermionic-emission theory (TE), developed by Bethe, is based on several assumptions [30]. The first one is that the transport-limiting process is an electron passage through the potential barrier, while the influence of drift and diffusion through the space-charge layer is neglected. The second one is that just like in the p-n junction, the quasi-Fermi level in the depletion region is flat and coincides with the bulk Fermi level. Therefore applying a bias voltage U leads to an increase of the electron concentration near the junction by a factor of $\exp\left(\frac{qU}{k_B T}\right)$. The third assumption is that

in the immediate vicinity of the junction, electrons obey Maxwell's distribution of velocities, and consequently the kinetic theory can be applied. Calculations, based on these assumptions, give an expression for the current density dependence on voltage U for $U > 3k_BT/q$ as:

$$J = J_0 \left\{ \exp\left(\frac{qU}{nk_BT}\right) - 1 \right\}, \quad (4)$$

where $J_0 = A^{**}T^2 \exp(\frac{-q\varphi_{eff}}{k_BT})$, with A^{**} being the Richardson constant that accounts for the effective mass of the electrons in the semiconductor, and quantum mechanical effects (for example reflection from the potential barrier); φ_{eff} is the effective height of the potential barrier, and n is the ideality factor, which reflects the dependence of the barrier height on the bias voltage (caused by surface states, the image force of electrons that is always present even in the most ideal contact, etc.).

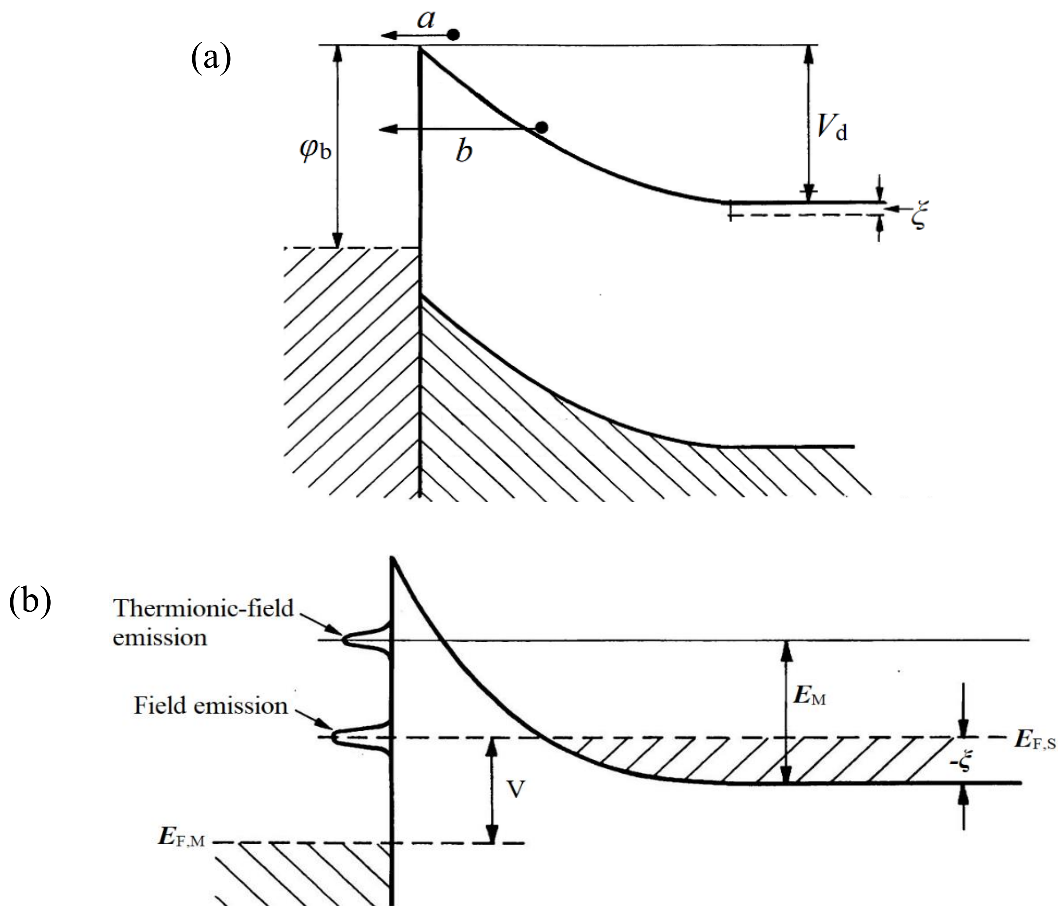

Figure 10. (a) Schematic representation of the most prevalent transport processes across a Schottky barrier; **a** – thermionic emission, the process occurring at sufficiently high temperatures, when thermal energy of the electrons is higher than the energy barrier; **b** – field emission, mechanism prevalent at low temperatures or/and for highly doped semiconductors, when tunnelling of electrons through the barrier takes place; ϕ_b – barrier height, V_d – diffusion voltage; ξ – energy difference between the conduction band E_C and Fermi energy E_F (negative for the degenerate diodes); (b) Field and Thermionic-field emission under the forward bias. TFE is a process, in which concentration of the electrons and the barrier thickness decrease with increasing energy, consequently, the main conductivity contribution comes from the electrons with some energy E_M, at which both barrier thickness and charge carrier concentration "equilibrate" each other. Reproduced from [27] with modifications.

For Schottky diodes, produced under conditions close to ideal, *n* is approximately equal to 1.01-1.02 [29].

Ordinary thermionic process may be modified under certain circumstances by quantum mechanical effects such as tunneling [30]. For example, if we take a heavily-doped or degenerate semiconductor (Fig. 10(b)), electron tunneling can be very significant, while at lower temperatures field emission (FE) can be the only mode of transportation. For higher temperatures, due to the higher concentration of electrons in the vicinity of the thinner barrier, the current is increased and the main contribution comes from the electrons on a certain energy level within the conduction band; such mixed mode of transportation is known as *thermionic-field* emission (TFE). Calculations of the current value based on the tunneling probability through the triangular barrier give the following expression:

$$J = J_s\left(exp\left(\frac{qU}{nk_BT}\right) - 1\right) = J_s\left(exp\left(\frac{U}{U_C}\right) - 1\right), \quad (5)$$

where $U_C = nk_BT/q$. Equations (4) and (5) have completely equivalent form, however, J_s in eqn. (5) has a more complex form [27], than in presented in eqn. (4) for J_0. Parameter E_d plays an important role in tunneling theory:

$$E_d = \frac{q\hbar}{2}\left(\frac{N_d}{m^*\varepsilon_s}\right)^{1/2} \quad (6)$$

$$U_C = E_{00}coth\left(\frac{qE_{00}}{k_BT}\right). \quad (7)$$

In these equations, N_d is the concentration of charge carriers in the semiconductor (accepted to be equal to the concentration of the dopant), m^* is the electron effective mass, and ε_s is a full dielectric constant of the semiconductor. Since $E_d \approx U_C$, values of the characteristic voltages, obtained from the fitting of the DC curves allow calculating the charge carrier concentration in the semiconductor. The physical meaning of the parameter E_d is that it is a *diffusion* potential of a Schottky barrier for which a transmission probability of an electron at the bottom of the conduction band at the edge of the depletion layer is equal to e^{-1}; consequently, the ratio k_BT/qE_{00} signifies the dominant process: for $k_BT>>qE_d$ TE is the dominant process, for $k_BT<<qE_d$, FE (or tunneling) dominates. For $k_BT\approx qE_d$ TFE is the main contributing process.

From the above information, it is quite obvious that for low barrier height and a high doping concentration, the resistance created by the barrier significantly decreases and the contact becomes ohmic. In industry, such contacts are created by ultra-high doping; lowering of the barrier by

choosing a metal of lower work function usually is not an option, since the value of φ_m does not vary much between different metals.

2.3 Surface Properties of Lithium Niobate

As can be seen from the previous section, the surface configuration significantly influences the device operation; it concerns not only diodes, as researched in this work, but also already mass-produced devices. For example, LNO is widely applied in surface acoustic wave (SAW) devices [31]; such devices often include interfaces (in the form of an electrode or a waveguide), consequently, interface properties are of crucial importance. Another example is the application of lithium niobate as a substrate for GaN growth [32] due to their very low lattice mismatch. Surface catalysts, gas sensors, and potential memory devices [32] on the basis of ferroelectrics (and LNO in particular [33]) are also very demanding to the quality of a surface. And although research of the LNO surface structure is several decades old, microscopic knowledge of LNO surfaces is still poor [33]; due to the presence of surface charge (both screening charge and permanent dipole moments), the application of scanning probe microscopy (both AFM and STM – scanning tunneling microscopy) for obtaining atomic resolution images of the surface is highly challenging.

In this work exclusively z-cut $LiNbO_3$ samples will be investigated; consequently, in this section only the description of ±z-surfaces of the crystal will be given. These surfaces are the most intensively investigated ones (both experimentally and computationally), since they are the most relevant for practical purposes [32]. It should be also noted that it is not systematically known, how material composition (stoichiometric, congruent, or doped) of LNO influences its surface properties (and whether it has any influence at all), so the following description can be applied to any LNO surface [32].

2.3.1 +Z- and –Z-Surface Reconstruction

Uniaxial ferroelectrics, cut perpendicularly to the polarization axis, will have two surfaces with opposite polarization. In order to stabilize such charged surfaces, the formation of an electric field, otherwise known as *depolarization* field, occurs [34], which lowers the dipole moment near the surfaces. The formation of such a field can happen through multiple mechanisms that can be separated into two large groups: external and internal. External mechanism include the adsorption of charged (or partially charged) atoms and molecules and other foreign adsorbates from the outside [35]. Internal mechanisms are much more varied and include the modification of surface morphology (through surface reconstruction) and stoichiometry (the process occurs through spontaneous desorption of atoms) [31]. In some cases, the electronic structure of the ferroelectric

near the surface can be changed, which can lead to partial surface metallization [36]. As a rule, surface configuration in ferroelectrics (and, more generally, in materials with polar surfaces) differs drastically from the bulk configuration of the material, and surface physical and chemical properties are mainly determined by a multitude of stabilization processes.

Correspondingly, in LNO the surface type is a defining characteristic; +z- and –z- sides are noticeably different in their physical and chemical properties. Concerning external stabilization mechanism, both sides at ambient conditions contain a multitude of adsorbed gases. For positive z-cut a desorption of O_2, CO, and H_2O will happen at temperatures of approximately 1075, 450, and 325 K correspondingly (for ambient pressure); negative z-cut is a stronger adsorbate; for molecules of O_2, CO_2, H_2O, and N_2 desorption temperatures are 1450 K (very close to the Curie point), 500, 450, and 400 K respectively. A full phase diagrams for adsorption can be found in Hölscher et al. [37]. It should be noted that even at ultra-low pressures, adsorbed oxygen can still be retained on the surface, and consequently influence the metal-LNO contact.

As for the surface structure and internal depolarization mechanisms, a variety of surface investigations was conducted in the last decades. Electron diffraction methods have shown that z-cut surfaces of LNO exhibit (1×1) surface periodicity without long-range reconstruction [38]. ultraviolet photoelectron spectroscopy (UPS) and x-ray photoelectron spectroscopy (XPS) of positive and negative z-cut surfaces have not shown any significant differences between the surfaces; however, the ionization energy I of +z- and –z-sides varies significantly: 6.2 eV and 4.9 eV correspondingly [39]. For semiconductor (and dielectric) materials ionization energy consists of two contributions: $I = E_g + \chi$. The electron affinity is the quantity that is heavily influenced by surface configuration and electric surface dipoles specifically, hence such a dramatic difference is understandable.

Density-functional theory (DFT) calculations of the z-cut surface structure of LNO have shown that the most thermodynamically stable surface configurations, determined by the thermodynamics of the growth conditions, are O-Li- termination for –z-side and -Nb-O_3-Li_2 termination for +z-side, see Fig. 11 [33, 40]. As can be seen, the +z-side is more oxygen rich than the –z-side, although under O-rich conditions the amount of oxygen in termination groups is higher. Ion scattering spectroscopy (ISS) indeed demonstrates that both thermally untreated surfaces are O-terminated [38] (due to its small atomic number and mass, Li atoms cannot be detected with ISS method).

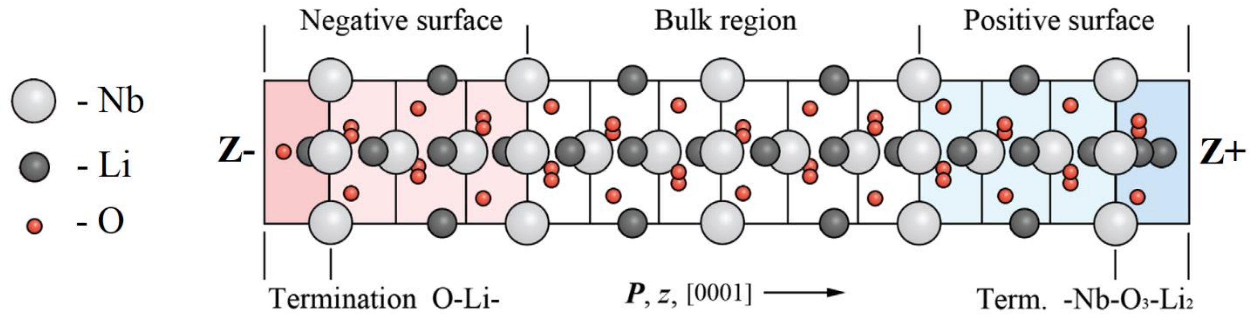

Figure 11. Schematic representation of LNO bulk and surfaces, obtained by DFT method. Reconstruction of the z+ and z- surfaces occurs, induced mainly by the tendency of the system to surface charge compensation. As a consequence, z+ side is more oxygen rich than z- side; no displacement of Nb atoms from equilibrium positions is predicted. The results of this DFT prediction are in accordance with practical analysis. Reproduced from [40] with modifications.

Such a surface configuration has a dipole moment opposite to the spontaneous polarization of the lithium niobate bulk and consequently reduces the surface charge, lowering the free energy of the structure. Compared to the very high value of the bulk spontaneous polarization of 700 mC/m^2, the measured surface charge of 0.14 mC $/m^2$ is more than three orders of magnitude lower [41], which demonstrates an excellent charge compensation. And although some other surface configurations have higher values of compensatory dipole [42], this configuration turns out to be the most stable, hence other stabilization mechanisms also influence the surface reconfiguration. *Ab initio* analysis also gives values of the ionization energy: 6.5 eV for +z-side and 4.6 eV for –z-side. These values excellently agree with the experimental numbers, given in the previous paragraph, and the slight difference can be explained by the presence of adsorbed gases under experimental conditions.

Taking into account the facts that both external and internal mechanisms are temperature dependent and that LNO has strong ferro-, pyro-, and piezoelectric properties, the final surface configuration (and its physical and chemical properties) will be highly dependent on the interplay of a multitude of environmental factors, such as temperature, atmospheric composition, and pressure. Because of that, the magnitude of the surface charge can oscillate around zero, taking both positive and negative values due to over- or undercompensation [32].

2.3.2 Practical Processing Methods of Lithium Niobate Surfaces

AFM of a mirror-polished, optical quality z-cut LNO wafers indicates a very poor quality of the surface – it demonstrates a polycrystalline surface with large number of grains and irregular corrugations [31]. It is also heavily contaminated with carbon compounds [43, 44]. A proofed

method of obtaining clean, atomically flat z-cut LNO surfaces is annealing at high temperatures (~1000 °C, close to the Curie point) for several hours. During the annealing, at approximately 500 °C a reconfiguration of the surface begins, and at temperatures higher than 600 °C step and terrace structures start to form. For prolonged annealing at high temperatures terraces become atomically flat and wide, and the step height corresponds to 0.22 nm – a value close to theoretically calculated 0.23 nm – the size of Nb, Li and O ions along the z-axis [31]. At temperatures of 400-600 °C, desorption of Li and O atoms begins [32, 33, 45]; at the +z-side the desorption rate of LiO is one order of magnitude higher than at –z-side, which is not surprising, considering the fact that the –z-side is oxygen-poor. XPS and co-axial impact collision ion scattering spectroscopy (CAICISS) were utilized for determining the topmost structure of annealed LNO. During annealing, out-diffusion of Li and O occurs; consequently, V_{Li} and V_O in the vicinity of the surface are constantly refilled. XPS analysis also showed that the ratio of compounds after annealing is as follows: Li/Nb is 1/3 (stoichiometric is 1) and Li/O is 2.88 (stoichiometric is 3), consequently; after annealing of the z-cut crystal, both sides are Nb terminated and partial reduction occurs, as evidenced by the detection of Nb^{4+} and Nb^{3+} ions. The surface also retains the threefold symmetry of the bulk $LiNbO_3$, as shown by CAICISS, Nb atoms are not shifted from their bulk position [31]. DFT-calculated phase diagrams predict Nb- termination for –z-side and -Nb-O termination for +z-side [33]. Loss of Nb has not been predicted by DFT, nor has it ever been observed.

As shown by experiment [44, 45], high-energy Ar^+ ion bombardment of LNO leads to the alteration of the substrate surface with destruction of Nb-O bonds, and consequently, reduction of Nb^{5+}, as evidenced by the appearance of the band emission at 1.3 eV below the Fermi edge. This line disappears after the thermal treatment at 800°C. It is suggested that such a line appears due to vacancies and other lattice defects, thus its disappearance after annealing is consistent with theory. In sum, ion (and electron) bombardment is a destructive method that is detrimental to the LNO surface and thus should not be used for surface cleaning. Treatment with RF-plasma [44], however, is a neat, non-destructive method that allows to clean heavily carbon-contaminated LNO surfaces without influence on surface roughness or ions valence states. Both Ar and He plasma can be used, although He plasma is preferable due to its lower sputter yield (as a consequence of its lower mass). Use of this methods allows to reduce carbon contamination below XPS detection limit (less than 1 at.-%), and makes this method ideal for metal deposition pre-treatment.

Some of the other physicochemical properties of LNO surfaces are heavily polarization dependent and are still not fully explained. For example, lithium niobate is a notoriously inert

material from the chemical point of view; only fluoric acid HF or its mixture with nitric acid HNO_3 is used for etching [22, 46], etch rates are heavily dependent on the surface polarization: at –z-side the rate is an order of magnitude higher than at +z-side [47], in some cases the +z-side seems to be unaffected by the chemicals at all [22]. Consequently, chemical etch can be used as a method for a study of microdomain redistribution, e.g., Holstein et al. [2] presents spatial characterization of microdomains, both on the surface and those "buried" in the bulk of a sample.

Currently, the reason for such a highly anisotropic behavior is not known [32]. It should be also noted that even for the –z-side at the boiling point of acidic mixture etching rates are approximately equal to few $nm \cdot min^{-1}$ [22]; consequently, it is very seldomly used for creation of structures of several μm in depth in the industry. However, regions with high concentration of lattice imperfections, such as dislocations have an etching rate that is significantly higher than that of a material with a perfect lattice. Consequently, such methods are suggested for wave guide production in refs. [48] and [49]. With respect to the production of defined interfaces, wet etching is a highly unreliable method for an atomically flat surface obtainment, unless the initial surface is already having a configuration close to structurally regular lattice; otherwise, the irregularities and other defects in the vicinity of the surface become even more pronounced.

2.4 Geometrical Structure of Domain Walls Near the Surface

The geometrical structure of the domain walls near the surface can be significantly different from their structure in the bulk. Theoretical calculations by Eliseev et al. [50, 51] based on the Landau–Ginsburg–Devonshire (LGD) phenomenological approach show that DWs near the surface break the double electric layer, that was formed near the surface by the intrinsic polarization and the screening charges. As a consequence, a *stray depolarization field* is induced, which influences the domain wall structure: bending and broadening of the DW near the surface occur (Fig. 12); as can be also seen, the structure itself is asymmetric near the surface. In some cases, the bending can be so strong that the DW does not reach the surface. It was also calculated that in the DW region stress occurs; the stress causes the deformation of the surface itself [51, 52].

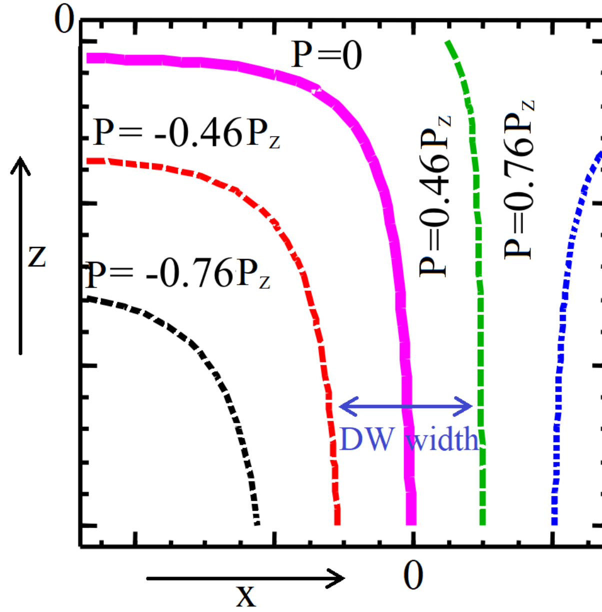

Figure 12. Schematic representation of the domain wall near the surface in the form of the order parameter (spontaneous polarization P) spatial distribution (in the x-z plane; further away from the surface the center of the DW has x = 0 coordinate; surface has an z = 0 coordinate). Boundary of the DW is considered as 0.46 of the maximum value of polarization (dashed lines) and 0.76 of the maximum value (dotted lines). Bending and broadening of the domain wall near the surface due to presence of the built-in surface field is calculated based on the LGD phenomenological approach. Picture reproduced from [51] with modifications.

Results of practical investigations, namely scanning non-linear dielectric microscopy (SNDM) and piezoelectric force microscopy (PFM) support these calculations. According to Choudhury et al. [53], the surface width of the DWs takes on values from 20 to 100 nm with statistical variation, while the size of the structure in the bulk (50-100 nm from the surface) lies in the region of 1-2.5 nm. The broadening of the DW structure heavily depends on the nature of the surface (way of surface preparation, presence and type of defects, etc.). The movement of the DWs is also width- and defect concentration-dependent (defects serve as pinning sites against DW movement); this can come into play in the course of the domain wall conductivity (DWC) enhancement. The nature of charged and dielectric defects adjacent to the wall and their concentration can also lead to the broadening of the DW structure; that is why for stoichiometric $LiTaO_3$ (ferroelectric material very close in its properties to $LiNbO_3$) the surface broadening of the DW is significantly smaller than that of congruent $LiTaO_3$ [54]. Other experiments demonstrate that the average width of the DW structure depends on the thickness of the bulk crystal (5.33 nm in the 50 nm-thick $LiNbO_3$ sample vs. 26.18 nm in the 500 nm-thick sample) [55]; the inclination of the DW also plays a role in its width, e.g., for 0.1° tilt the width is 0.5 nm, for 5° tilt the width is 10 nm [56]. The widths of the DW on the opposite sides of the crystals are also different [52]. All such evidence leads to the conclusion that a multitude of factors exists, which can have a

significant influence on the DW-metal contact, and that for achievement of reproducibility in device production, high uniformity of conditions and some other sophisticated procedures, such as annealing and high vacuum deposition under clean-room conditions are necessary.

2.5 Electronic Transport in Lithium Niobate

2.5.1 DC Conductivity and Transport Mechanism

As was established by Zahn in his Master's thesis [15], the temperature dependence of the conductance in LNO domain walls in the temperature range between 100 K and 300 K has a thermally activated form:

$$\sigma(T) = \tilde{\sigma}_0 \exp\left(-\frac{E_a}{k_B T}\right), \tag{8}$$

where E_a is the activation energy, $\tilde{\sigma}_0$ is a preexponential factor; variable range hopping transport model was not supported by the measurements. Two other processes, adiabatic and non-adiabatic polaron hopping was suggested; they are characterized by multiplication of the eqn. (8) by factors T and $T^{3/2}$ correspondingly. Because these multiplicators have a power temperature dependence that is multiplied by the member with exponential temperature dependence, determination of power temperature dependence is complicated. Consequently, it was not established in the cited work; other optical methods are required for such a determination [57]. The measured activation energy value was in the range of 0.1 – 0.25 eV. Such differences between the samples serves as a further motivation for improvement of reproducibility in the DW production process.

As was mentioned in the introduction, the equivalent circuit shown in Fig. 6(b) was postulated by Zahn in his thesis. Fitting of obtained DC curves demonstrated 1) an excellent agreement with the suggested model; 2) very high values of the characteristic voltage U_c (as compared to the one of commercially available Schottky diodes), which, according to equation (6) is evidence of the extraordinary high charge carrier concentration (of the order of 10^{20} cm^{-3}).

2.5.2 Temperature Influence on Electronic Transport in LNO Domain Walls

As mentioned above, the main charge carriers in the h2h LNO domain wall structure are screening electrons; consequently, in such a many-electron system the occupation of energy states is described by the Fermi-Dirac statistics [58]:

$$f(E) = \frac{1}{1 + \exp\left(\frac{E - E_F}{k_B T}\right)}, \tag{9}$$

where *f(E)* is a distribution function (probability that a state of given energy E is occupied).

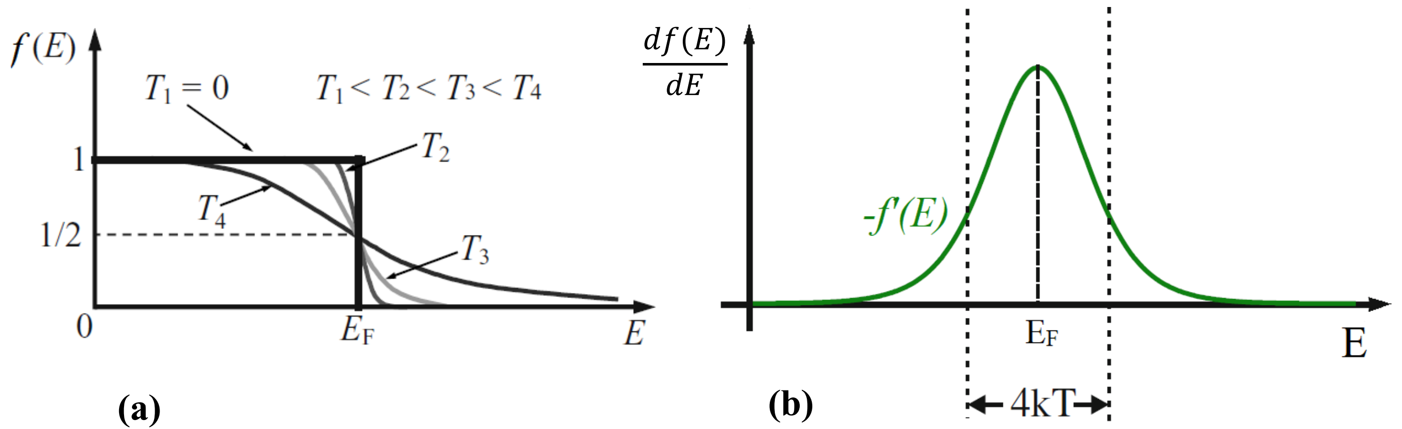

Figure 13. (a) Variation of the Fermi distribution function in a many-electron systems at temperature T. Reproduced from [58]. (b) First derivative of the Fermi distribution function. The only non-zero values exist in the peak around the Fermi energy; the width of the peak is proportional to the temperature T; this value gives a rough value of energy resolution maxima for investigation of energy dependent processes. Reproduced from [59].

As can be seen from the Fig. 13(a), for T = 0 K, *f(E)* is a step function, which at higher temperatures transforms into a broadened (or smeared out) step function. If we look at the first derivative *f'(E)* of this distribution function (Fig. 13(b)), we can see that it is nearly zero for almost all values of energy E besides the symmetrical peak with the width of approximately $4k_BT$ around the Fermi energy E_F. Hence, at room temperature the broadening is approximately 83 meV and increases by 0.28 meV/K [59]. Obviously, only the states in the region of the peak will contribute to the charge transport.

As a consequence, in order to explore the fine structure of the lithium niobate domain walls in the vicinity of the Fermi level and contribution of phonons, electron-electron interaction, scattering effects, and crystal defects with different energy levels to the charge transport, low-temperature conductance investigations are necessary. Both AC and DC conductance measurements are two of the most convenient ways for such investigations; below, several examples of such measurements will be given.

In order to describe DW charge transport, it is necessary to give a proper presentation of how electron states depend on the energy, some kind of dependence that is analogues to the energy level diagrams in Figs. 8-10. Since a DW can be described as an extended defect in the structure of the crystal, we will use a theory of the charge transport in disordered systems, in which due to large amount of various defects the symmetry of the crystal is broken [60]. In Fig. 14 the energy dependence of the density of states (DOS) g(E) in disordered material is presented.

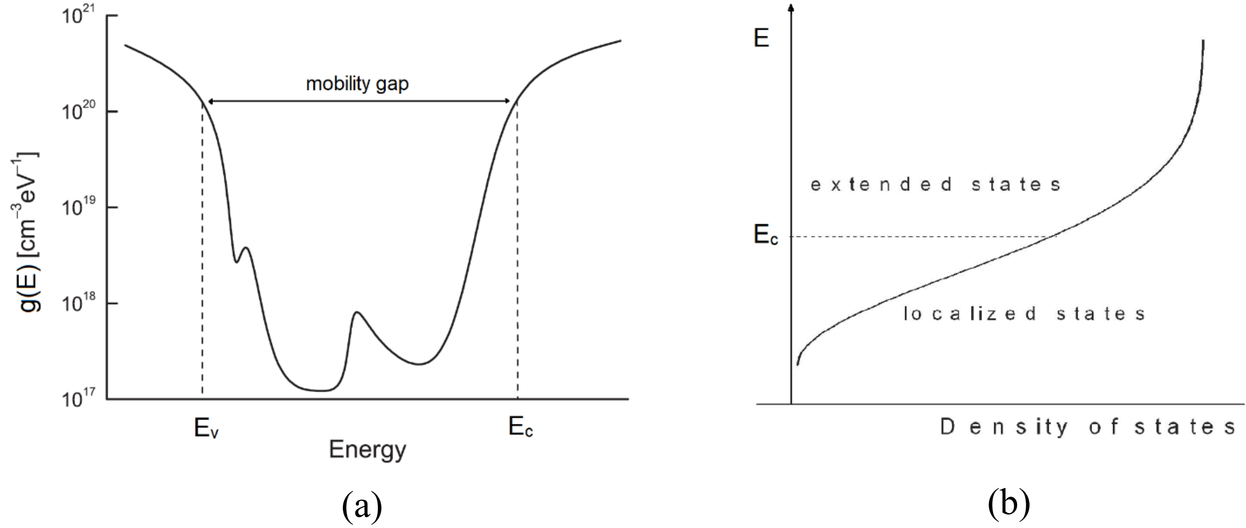

Figure 14. (a) The density of states (DOS) in a disordered solid. E_v and E_c are mobility edges; they separate regions with extended electron states (analogous to valence and conduction bands in regular crystalline materials) and localized electron states, so-called mobility gap (this region is analogous to the band gap in crystalline materials, picture (b) gives a close-up view of transition between mobility gap and extended states). Depending on the position of the Fermi level (above or below the conduction band edge), character of the charge transport in a material and its dependence on temperature changes dramatically. The picture is reproduced from [60].

It is obvious that it closely resembles the energy structure of a simple crystalline semiconductor (in the absence of long-range order close-range order still exists, hence the diagram retains its characteristic features); however, it contains not only regions of high electron density with delocalized states in it, but also localized states ("localization" of a state implies exponential decay of electron wave function away from the localization point) inside in the so-called mobility gap. The type of charge transport in such system is heavily dependent upon the position of Fermi energy E_F. If the Fermi level lies in the extended states region i.e., $E_F > E_c$, charge carriers are treated as nearly free electron gas (using a Fermi-liquid approach and the Boltzmann theory), weakly scattered by disorder as follows:

$$\sigma = \frac{ne^2}{m^*}\tau. \tag{10}$$

Here n is charge carrier density, m^* is the charge carrier effective mass, and τ is the time between scattering events; the expression has a very similar form to the conductivity in Drude theory. The theory above is based on the supposition of weak disorder (in case of a very strong disorder of the material, all states become localized). At cryogenic temperatures, the main source of scattering comes from the static potential of impurities, and, since the scattering is elastic, both

scattering probability and, consequently, the conductivity are almost temperature independent. DC conductivity in the extended states is finite at T = 0 K and according to Boltzmann theory, temperature coefficient of resistivity is $\frac{d\rho}{dT} > 0$. Such properties are called "normal metallic" behavior of conductivity.

Additionally, several scattering effects, influencing the material's conductivity, should be mentioned. Besides scattering by static random potential, mentioned above, other contributions are phonon scattering ($\rho \sim T$, in the region of low temperatures $\rho \sim T^5$, Bloch-Grüneisen law [60]), scattering by static impurities (this mechanism is temperature dependent; it is connected with the screening effect, which becomes weaker with higher temperatures; hence $\frac{d\rho}{dT} > 0$). Another scattering mechanism is electron-electron (e-e) interaction, both classical Coulomb interaction ($\frac{d\rho}{dT} > 0$) and quantum interference. The latter effect is especially pronounced at lower temperatures and cannot be neglected. Scaling theory of localization and Mott's extension of weak scattering transport theory take e-e interaction into account; a description of both theories is beyond the scope of this work, however some results of the theoretical calculations will be discussed below.

In case the Fermi level lies in the mobility gap, i.e., $E_F < E_c$, charge transport occurs through another mechanism – inelastic tunneling between localized states termed *hopping*. This mode of transport can be realized only in the presence of phonons (energy levels of different delocalized sites vary in energy, consequently, required energy can be supplied only by lattice vibrations). As a consequence, at some point of lowering the temperature, conductivity of the material with such properties vanishes. This behavior ($\frac{d\rho}{dT} < 0$) is characteristic of semiconductors and insulators. It should be noted that in such a configuration, phonons are the driving force behind the charge transport, unlike in the metal-like conductivity case, where phonons are an impeding factor. Temperature dependence of the conductivity in such materials at sufficiently low temperatures (~50 K and less) strongly depends on the properties of the material, especially the DOS in the band tail region, and can be described by a multitude of models [61]: Mott's law (constant DOS in the vicinity of Fermi level; $\sigma(T) \sim \exp\left(\left[\frac{1}{T}\right]^{-\frac{1}{4}}\right)$), Efros-Shklovskii law (parabolic DOS in the vicinity of Fermi level due to electrons Coulomb interaction; $\sigma(T) \sim \exp\left(\left[\frac{1}{T}\right]^{-\frac{1}{2}}\right)$), etc.

In case the Fermi level is positioned in the immediate vicinity of the mobility edge E_c, at not too low temperatures, the system's conductivity very often has an activated form of the eqn. (8).

We can use this equation in accordance with Mott's concepts: (a) conductivity below E_c is zero; (b) there is a minimum conductivity σ_{min}, below which the value of σ does not decrease, we obtain $\tilde{\sigma}_0 = \sigma_{min}$ and $E_a = E_c - E_F$. Thus, the conduction is provided by charge carriers thermally activated to extended states.

Such mode of conductivity is often observed in both crystalline and disordered semiconductors. Activation energy can vary from one sample to another due to the difference in preparation conditions, doping and some other external factors, e.g., prolonged illumination [62]; here we assume that E_c and E_F do not change the position in relation to each other (although such change is possible, e.g., due to change of temperature). The pre-exponential factor in the equation is heavily dependent upon electronic structure near the mobility edge and by the DOS in the mobility gap. As was explained above, such high-temperature measurements do not provide good information on a charge transport mechanism near the mobility edge, nor it gives any information about electronic structure near E_c, since many electrons with different thermal energy participate in charge transport. Low-temperature measurements near the mobility edge (E_F in the immediate vicinity of E_c, or so-called metal-insulator transition region) are necessary.

In 2D electron systems, for example the inversion layer in a Si MOSFET device (metal-oxide-semiconductor field-effect transistor) or in GaAs heterostructures, a semiconductor to metal transition occurs when a certain critical concentration of charge carriers (n_c) is reached [63]. The resistivity's temperature coefficient changes its sign, the resistivity has an exponential dependence on temperature in both regions (with different signs of the exponential expression):

$$\rho(T) = \rho_0 + \rho_1 \exp\left(-\frac{T_0}{T}\right). \tag{11}$$

Here T_0 is a scaling parameter, which is proportional to charge carrier concentration, i.e. $T_0 \sim (n - n_c)$. Such behavior poorly corresponds to both scaling theory of localization or Mott's calculations, and the main contribution factor to conductivity in such systems in the vicinity of the mobility edge can be not the e-e interaction, but other various scattering mechanisms, listed above. Based on this information, we can assume similar behavior of the LNO domain walls, since its charge carrier concentration can be varied by changing DW inclination.

2.5.3 Application of AC Measurements for Charge Transport Investigations

In order to investigate the fine electron structure of the material, and, consequently, the main ways of charge transport in this material, application of AC voltage excitation and analysis of the obtained output signal can be utilized. One of the main advantages of such a method is the detection

possibility of even the smallest changes in the current, that cannot be detected through the simple IV-curve, e.g., due to averaging over electronic noise. The following example of Inelastic Electron Tunneling Spectroscopy (IETS), although applied mainly for the investigation of vibrational structure of molecules, can give a good understanding of the AC measurement benefits. Practically, the technique can be used for metal-insulator-metal (MIM) tunneling junctions [64], in STM [65], and in the mechanically controllable break junction [66]. In the tunnel junction under applied bias V (Fig.15(a)) a tunneling current occurs; if the bias is large enough ($eV \geq h\nu$), electrons can tunnel inelastically – they lose a quant of their energy $h\nu$ to excite an additional vibrational state in the molecule in the tunneling junction; thus, an additional tunneling path is created and the conductivity of the junction is increased [67]. However, only a small amount of electrons tunnel inelastically, and an increase in the simple IV-curve (kink) is hard to detect (Fig. 11(b)). If the first and second derivatives of the current is analyzed, increase in the current will be visible as steps in the function and peaks, correspondingly (Fig. 15(b)). Admittedly, the most reliable for the current increase identification is the second derivative dependence on voltage $\frac{d^2I}{dV^2}(V)$. One of the factors contributing to the widening of the peaks until their full indistinguishability is the thermal broadening; hence IETS is conducted at cryogenic temperatures up to 10 K. In the Fig. 15(c) real spectra of 1,8-octanediamine (ODA) taken at 4.2 K are presented [68].

Although derivatives of the current-voltage curves can be obtained by the numerical differentiation of the simple IV-curve, such technique is not applied in practice due to the very low signal-to-noise ratio. Practically, such measurements are realized using a lock-in technique: a sinusoidal voltage $V = V_0 + V_1\cos(\omega t)$ is applied to the junction and the current response of a sample

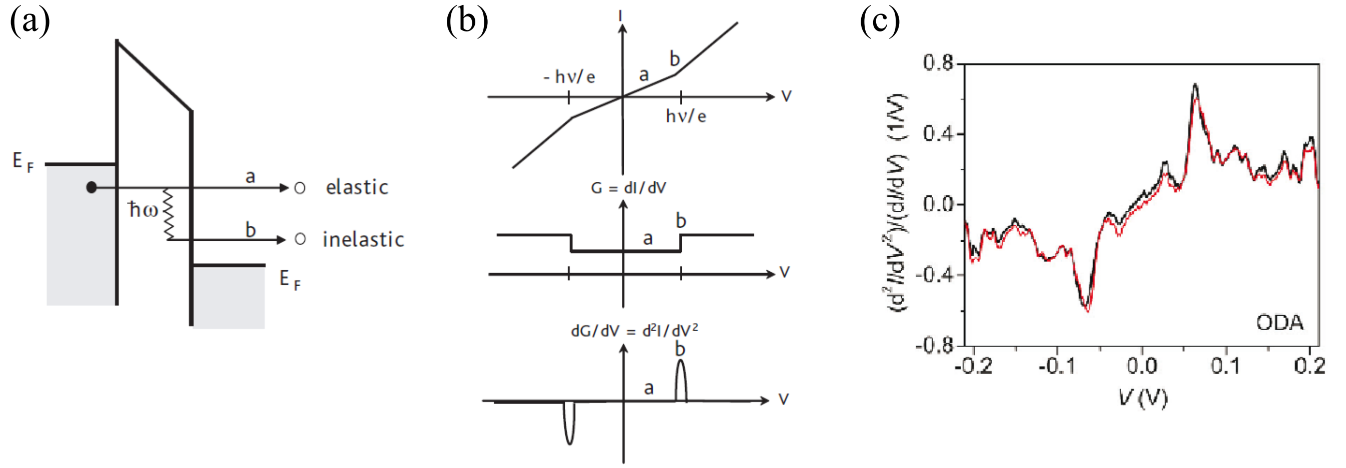

Figure 15. (a) Energy band diagram of the tunneling junction with a vibration mode of frequency ν. a - elastic tunneling pass, b - inelastic. (b) - voltage dependance of current I, first (dI/dV) and second (d^2I/dV^2) derivatives. Reproduced from [67]. (c) IETS spectra of ODA molecule, measured at 4.2 K. Reproduced from [68].

$I(V_0 + V_1 cos\omega t)$ is detected. Taylor expansion of the current around the offset voltage V_0 has the following form:

$$
\begin{aligned}
I(V_0 + V_1 cos\omega t) &= I(V_0) + \frac{dI(V_0)}{dV} V_1 cos\omega t + \frac{1}{2}\frac{d^2 I(V_0)}{dV^2} V_1^2 cos^2\omega t + \cdots \\
&= I(V_0) + \frac{dI(V_0)}{dV} V_1 cos\omega t + \frac{1}{4}\frac{d^2 I(V_0)}{dV^2} V_1^2 (1 + cos2\omega t) + \cdots
\end{aligned} \tag{12}
$$

As can be seen from eqn. (12), the measured tunneling current can be reduced to the sum of harmonic functions with frequencies $n\cdot\omega$, and what is more important, is that the amplitude of the signal at frequency $n\cdot\omega$ is proportional to the nth derivative of the IV-curve. It also should be noted that the detected signal is proportional to the amplitude of the modulation voltage V_1. In practice, such measurements are conducted using lock-in amplifiers (LIA) as well.

Based on the formula (12) and Fourier transformations, Zahn [15] the expressions for the current under application of an AC voltage. Applied to the problem of domain wall conductivity, under harmonic voltage excitation higher harmonic current contribution (HHCC) would originate from the Schottky junction in the DW-metal contact as the only element of the circuit with non-linear IV-response. Theoretical calculations for standard Schottky diode gave the following dependence of absolute value the nth HHCC on offset voltage U_0 and amplitude voltage U_1:

$$
|I_n| = I_s \cdot \mathbf{I_n}\left(\frac{U_1}{U_C}\right) \exp\left(\frac{U_0}{U_C}\right), \tag{13}
$$

where $\mathbf{I_n}$ (in bold) is modified Bessel function of first kind and of nth order, I_s and U_c are saturation current and characteristic voltage of a diode correspondingly. The phase angle of HHCC ($\arg(I_n)$) according to this model should move in anti-clockwise rotation:

$$\arg(I_n) = -\frac{\pi}{2}(n-1) \ . \qquad (14)$$

AC measurements of commercially available Schottky diode demonstrated an excellent correspondence of the theory to real behavior of the diode. IV-curves under AC voltage obtained for LNO samples also demonstrated good numerical agreement with suggested theory.

3 Experimental Methods and Setup

3.1 Lithium Niobate Samples and Sample Preparation Process

In this work 5-mol % Mg-doped lithium niobate crystals produced by Yamaju Ceramics Co., Ltd. were used. 200 μm-thick z-cut wafers with surfaces mechanically-polished to optical grade quality were cut into samples with a geometrical size of 5×6 mm^2 in x and y directions, respectively. Two different wafers from the above-mentioned manufacturer were utilized; samples, stemming from different wafers will be signified as "*ow*" – old wafer and "*nw*" – new wafer (the "old" wafer was acquired a one year earlier than the "new" one).

Before the poling process, glue residues had to be removed from the samples by plasma etching. For this purpose, an ATTO low pressure plasma system was utilized. Cleaning of the surface occurred in the atmosphere of oxygen plasma; the pressure in the chamber was around 0.5 bar. Under such conditions, the etching rate of LNO is 50 nm per minute; before the poling process, both sample surfaces were cleaned for 7 minutes (hence 350 nm of the material was removed from each side). After the plasma cleaning, the samples were successively cleaned for 5 minutes in isopropanol and acetone in ultrasonic bath.

3.2 Experimental Setup for Domain Inversion and Poling Protocol

The detailed description of the poling setup is available in Ratzenberger's Master's thesis [69]. Here, only a short description of the setup will be provided.

For the inversion of the spontaneous polarization in the single-domain sample, laser assisted poling was utilized. For these purposes liquid electrodes consisting of 2 g of NaCl per 100 ml of deionized water were used; the outer windows of liquid cells consist of quartz glass for higher transmission of visible and UV-light. Upper and lower parts of the liquid cell are tightly screwed together; in order to avoid leakage current and breakage of the sample, rubber rings separated the sample from the salt solution on both sides.

The schematic representation of the setup is presented in the Fig. 16. A 325-nm KIMMON KOHA IK3301R-G HeCd Laser was used as the UV radiation source. The laser beam was directed into an inverted microscope ZEISS Axio Observer. A neutral density filter was utilized to control the laser intensity. The laser beam was focused on the z+ side of the sample with apochromatic lens with NA = 0,3 (VEB Zeiss); the resulting diameter of the spot size of the beam is around 4,5 μm. A home-made laser shutter was put on the pathway of the laser beam to insure the full control of sample irradiation time. For visualization of the domain growth process and the recording of this

process, a THORLABS Zelux TM 1.6 MP Monochrome CMOS Camera was installed into the setup. A liquid cell was mounted on a motorized x-y moving stage attached to the microscope to obtain precision and stability of the process and fixated with screws.

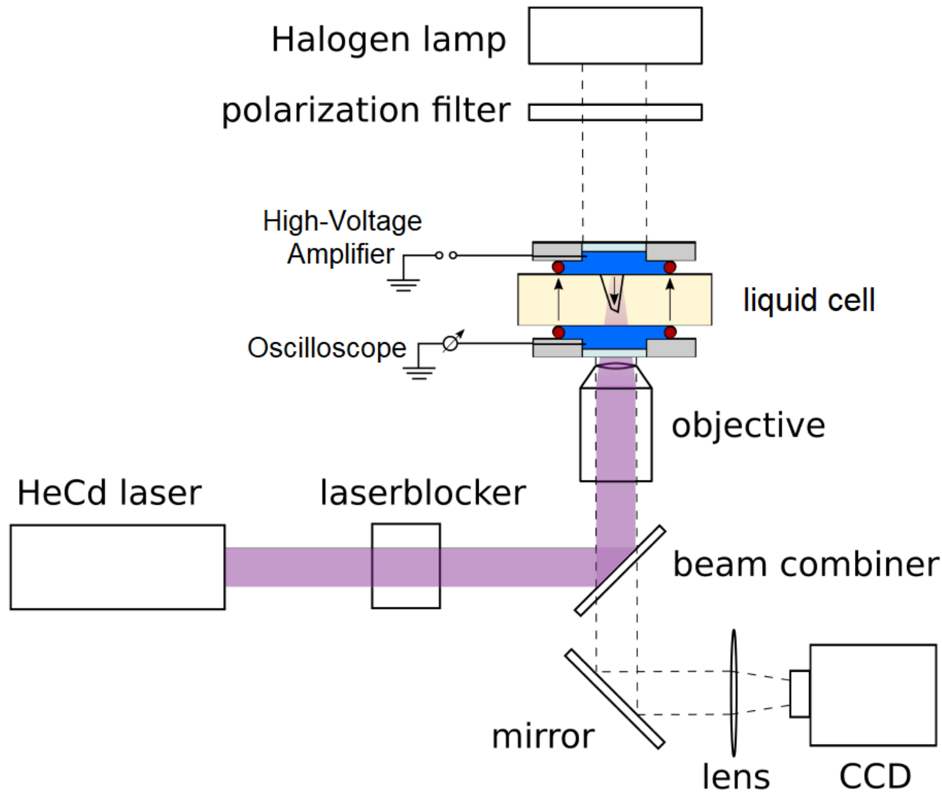

Figure 16. Schematic representation of the poling setup. The laser beam at 325 nm, represented by the violet light, is focused on the upper side (z+) of the sample (presented in light yellow inside a liquid cell). A voltage pulse, enhanced by a high-voltage amplifier, is applied to the liquid cell and controlled by the oscilloscope. For the visualization of the poling process, the sample is illuminated with a halogen lamp. The scheme is reproduced from [69] with modifications.

The poling voltage pulse was produced by an Agilent 33220A Arbitrary Waveform Generator in connection with a Trek 2210 high-voltage amplifier; for pulse shape monitoring a Tektronix TDS2024B digital oscilloscope was used. The waveform generator, the oscilloscope, the laser shutter, the x-y moving stage, and the camera were connected to a computer and controlled via home-built python3 scripts.

The shape of the voltage pulse is presented on the Fig. 17. The voltage value undergoes a quick rise (within 1 s) till its poling value (in this work samples poled under 800 and 900 V were investigated). Then, the voltage stays at its poling value for some time, called the pulse length; the two most frequently employed pulse lengths in this work are 30 and 120 s. After the poling is

finished, the voltage is gradually lowered to zero in an interval of 20 s to avoid back switching. The laser is blocked for 5 s before the beginning of the poling process to avoid premature excitation of the sample.

In this work, the name of a sample reflects the way it was prepared. For example, the first batch of samples (14 in total), prepared by J. Ratzenberger during the course of his master's work [69], were named in the following format: jr-(*poling_voltage)*-(*pulse_length)*-(*parent_wafer)* (e.g., jr-800-60-ow). The rest of the samples were prepared from the "new" wafer under the poling voltage of 800 V. The way of cleaning and voltage pulse length are reflected in their name (e.g., 800_120_plasma_clean_1) or the fact that the sample was annealed (all annealed samples were prepared with the poling pulse of the length 120 sec, an example of the name is the following: annealed_samp_2). The last number in the name reflects the serial number of the sample in the

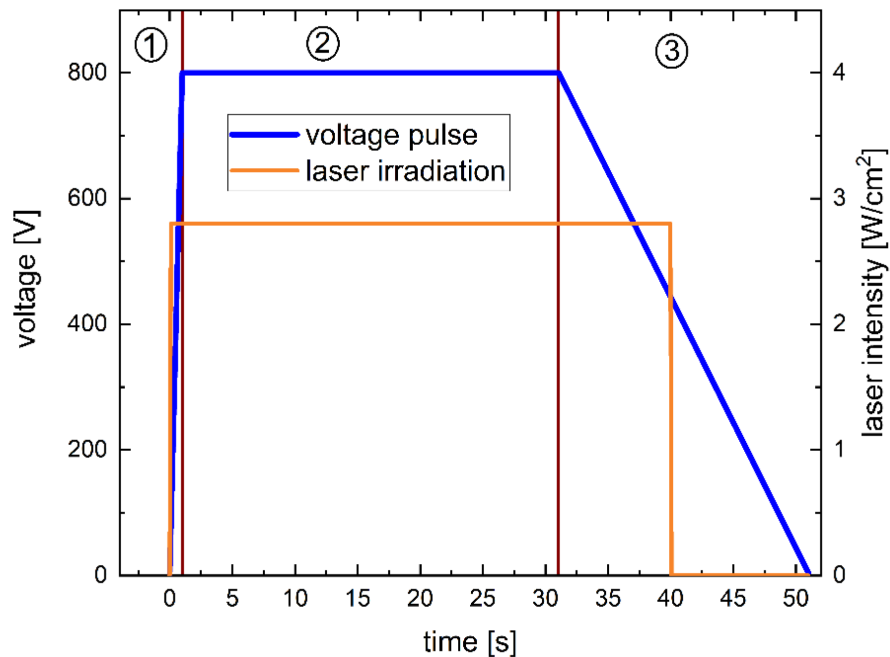

Figure 17. Example of the pulse shape utilized for poling the LNO samples. In step one, the voltage rapidly rises to its poling value (in this case 800 V); the laser shutter opens at the same time; in step two, the voltage pulse keeps its poling value for the time of the pulse length; in step three, the voltage is gradually lowered to zero to avoid back switching of the formed domain; the laser impact lasts ten seconds longer than the pulse length. Reproduced from [69].

batch.

After the domain poling, samples were thoroughly rinsed with deionized water and then placed into deionized water in the ultrasonic bath for five minutes in order to remove all NaCl residues after the poling process. After that, the samples were respectively placed for 10 minutes in isopropanol and for 10 minutes in acetone in the ultrasonic bath in order to obtain a cleaner

surface, and, consequently a good homogeneous contact between the LNO surface and the metal electrode in the next step.

3.3 Deposition of Metal Electrodes and Enhancement of the Domain Wall Conductivity

In this work, chromium was used for the creation of metal electrodes; they were deposited by thermal evaporation under high vacuum conditions (approx. 10^{-7} torr); the thickness of the electrodes was around 10-11 nm with a lateral geometrical size of the electrodes of approx. 5 mm in both directions.

In some experiments, the re-deposition of the chromium electrodes was utilized. In this case, the old electrodes were removed with the water solution of ammonium cerium nitrate $(NH_4)_2[Ce(NO_3)_6/HClO4]$; afterwards, the standard cleaning procedure and deposition process described above were utilized.

After the deposition of metal electrodes, the conductivity of the domain walls was enhanced by the method developed by Godau et al. [6]. The metal electrodes were connected with a Keithley 6517B Electrometer with silver paste. In initial IV-measurements (before the DWC enhancement), the LNO samples demonstrated very low current of the order of 10^{-10}-10^{-11} A. Afterwards, a negative voltage up to -600 V was applied via the electrometer voltage source to the samples (with voltage ramp of 0.5 V/sec). In order to avoid the explosion of the domain wall, the voltage increase was stopped when the value of the current running through the DWs was close to 10^{-5} A (usually when current values were approximately $4 \cdot 10^{-6}$ A). The sample was kept under the influence of the maximum reached negative voltage for ten minutes for the stabilization of the inclined structure of the domain wall. Thus, the DWC was permanently enhanced for up to 4 orders of magnitude.

3.4 Annealing Procedure of Lithium Niobate Crystals

As was described in the previous section, the quality of the surface has a significant influence on the near-surface DW structure and DW-metal contact. In this work, for the obtainment of atomically-smooth surface in z-cut LNO crystals, the annealing procedure, thoroughly described by Saito et. al. [31], was employed for 8 samples (termed as annealed_samp_#). Annealing was performed in a Nabertherm furnace (Germany) in air atmosphere. LNO samples were heated up to 1000°C with heating (and cooling) rates of 1 K/min. The annealing time at the maximum temperature of 1000°C was 5 h.

The samples were positioned on two ceramic plates with the height of 2 cm. In order to achieve the desired atomically-smooth surface, only the edges of the samples touched the ceramic plates, serving as a kind of a bridge; hence, both sides were in contact with the air.

3.5 Setup for DC Measurements at Room and Lower Temperatures

For the DC measurement (i.e., acquisition of standard IV curves) the sample was also connected to the Keithley 6517B electrometer, a positive voltage was always applied to the z+ side of the sample. The voltage was changed step-wise starting from -10 V to 10 and back with a voltage step of ΔU = 0.5 V or 0.25 V and time period Δt = 1 s or 5 s. It should be noted that measurements were conducted usually for a couple of hours (equivalent of approximately 90 full cycles) until the stabilization of IV-curves after enhancement was observed (no drastic changes in at least ten cycles of measurement). After the obtainment of DC IV-curves, its parameters (R, I_S, U_C in the forward and backward directions, Fig. 6(b)) were extracted by fitting the curve with a trust region reflective algorithm with least-squares cost function, in a python3 software, on the basis of the library scipy.

For DC conductivity measurements at lower temperatures, the samples were inserted into an Oxford Instruments Optistat DN liquid nitrogen bath cryostat. For temperature measurements, two independent PT100 platinum resistance sensors were installed into the setup, one in the immediate proximity to the sample and another at the heat exchanger. An Oxford ITC 503 temperature controller realized regulation of gas flow, heating control, and temperature control via the platinum resistor sensor at the heat exchanger. The platinum resistor sensor in the vicinity of the LNO sample was read out via a Keithley 196 Digital Multimeter. During measurements, the temperature set points were changed step-wise; stabilization time for the achievement of temperature equilibrium was set to 1200 s; the refill of the liquid nitrogen reservoir was realized every 4 h. For the current measurements, the Keithley 6517B electrometer was used again. All above-mentioned equipment was controlled via a home-built python3 script software. All the improvements to the above-described low temperature setup were implemented by Zahn (including the creation of python3 software) and described in his Master's thesis [15] in great detail; no change in the setup was implemented during this work.

3.6 AC Measurements

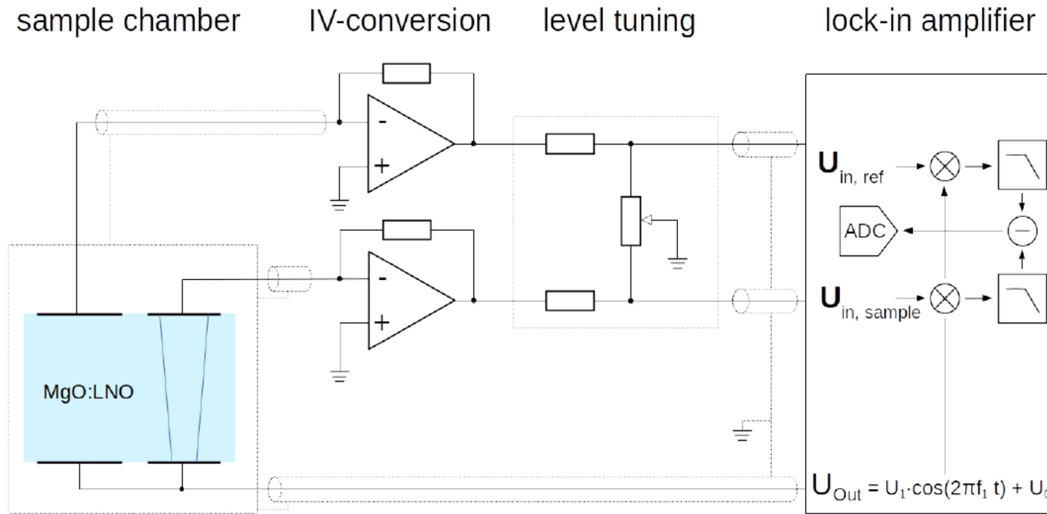

Figure 18. Electric circuit configuration used for AC measurements, consisting of a signal generator (with output signal $U_{out.}$), a LIA (referenced to $U_{out.}$ and two signals from a reference LNO sample and the investigated sample in subtraction regime), IV-converters and a level-tuning circuit. Reproduced from [15].

For the investigation of the AC response, lock-in amplifier-based dielectric differential measurements were conducted (Fig. 18). An output signal $U_{out} = U_0 + U_1 \sin(\omega_0 t)$ from the the signal generator Agilent 33250A was referenced to a lock-in amplifier (LIA) Stanford Research Systems SR830 and connected to both a multidomain sample and a LNO crystal with no domain walls (reference sample). Both sample with DWs and monodomain LNO crystal were enclosed into tinplate boxes and all connections were realized with BNC cables for proper shielding of noise, caused by the environment of the setup. Sample and reference LNO crystal were connected to IV-converters Femto DLPCA-200, which were in turn connected to the level-tuning circuit. The latter contains a 25-turn precision potentiometer, which compensates for unequal capacitance between sample and reference LNO crystal caused by different areas of chromium electrodes. Such arrangement is necessary for the liquidation of "parasitic" currents, generated by the capacitor, formed by the electrodes, and allows reaching an accuracy of approximately 1%. The tuning was accomplished at zero offset voltage U_0 at low amplitudes for 1st harmonic current; the imaginary part of the current was set to zero. The level-tuning circuit was connected to the LIA, working in the regime of subtraction. Based on the earlier obtained values of saturation current and characteristic voltage, offset sweep $|I_n|(U_0)$ curves and amplitude sweep $|I_n|(U_1)$ curves for n harmonics are modeled according to the theoretical equations for the diode (13) and (14), describing dependence of the absolute value of higher-harmonic current contribution (HHCC) on alternating excitation values U_1 and U_0 and sample intrinsic characteristics U_C and I_S.

4 Results and Discussion

In this section, the influence of the interface parameters, such as presence of the contamination on the lithium niobate surface, the surface quality of the lithium niobate crystal and the material of the electrode, on the formation on the Schottky barrier between the DW and the electrode material is investigated. Current-voltage characteristics of the obtained samples and quantitative characteristic of the formed Schottky barriers, such as the saturation current I_S and the characteristic voltage U_C, acquired from the fitting of these IV-curves according to the suggested equivalent circuit (Fig.6(b)), are the main objects of analysis in this work. Prior to such studies, however, the influence of poling parameters (poling voltage and the length of the poling pulse) on the conductance of the multidomain LNO samples will be studied; afterwards, the reproducibility of the samples in the laser-assisted poling setup will be examined.

4.1 DC Conductance of Domain Walls and Circuit Characteristics

The samples presented in this section were produced by J. Ratzenberger in the course of his master's work [69], where optimal poling and DWC-enhancement conditions for the reproducibility of the LNO samples were investigated. Here, the DC and AC (Appendix C) conductance of 14 such samples were studied and fitted according to the suggested model of the equivalent circuit; these samples are separated into three batches: the first batch is produced with the poling voltage of 800 V from the "old" wafer, the second batch is produced from the same "old" wafer, but with the poling voltage set to 900 V, and the third batch produced with the 900 V from the "new" wafer; the voltage pulse length was different from sample to sample. As a result, the effects of the domain size, and hence, the contact area between the DW and the metal electrode (parameters proportional to the poling voltage and pulse) as well as minute differences in the chemical composition of the crystal, will be investigated in this subsection; additionally, the accuracy of the suggested model will be checked on this statistically significant number of samples.

IV-curves of these samples are presented in the Figs. 19-21; as can be seen, some of the samples (e.g., jr-800-180-ow) show a rectifying (monodirectional or diode-like) IV-curve, similar to the curves of standard diodes, where the current along one direction is several orders of magnitude smaller than in the opposite direction. The equivalent circuit to describe such samples, can be a modified circuit presented in Fig. 6(b) using only one branch with resistor and diode. Other samples (e.g., jr-800-120-ow) demonstrate remarkable bidirectional (ohmic) curve, visually very similar to a curve of a simple resistor. It should be also noted, that the vast majority of the samples (10 out of 14) are "imploded", meaning the formation of a large multitude of the spike

domains instead of one domain with the inclined DWs as the result of high current through the DW during the DWC enhancement procedure (for more details see the ref. [7]).

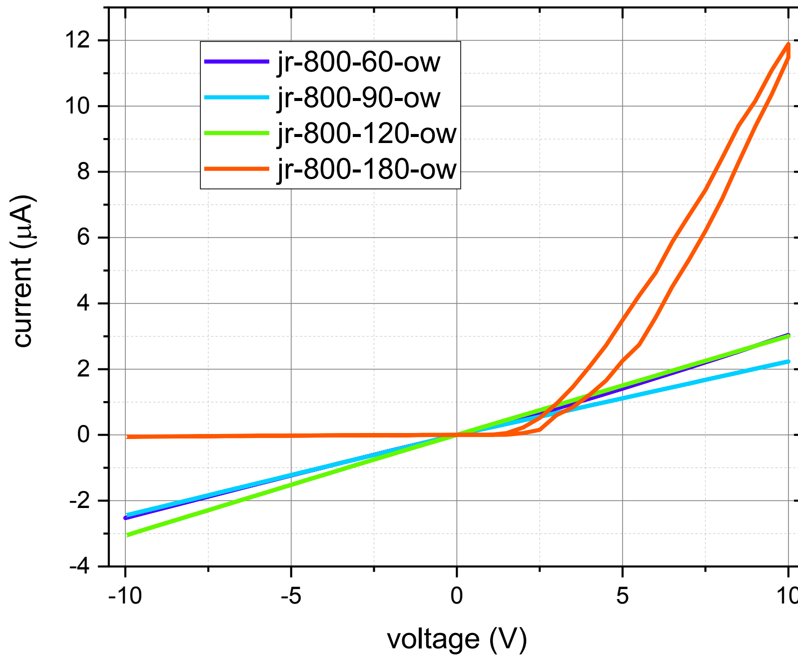

Figure 19. Room temperature IV-curves of samples with DWs created under 800 V in the old wafer crystals after domain wall stabilization. The voltage was changed step-wise with ΔU = 0.5 V, Δt = 2 s.

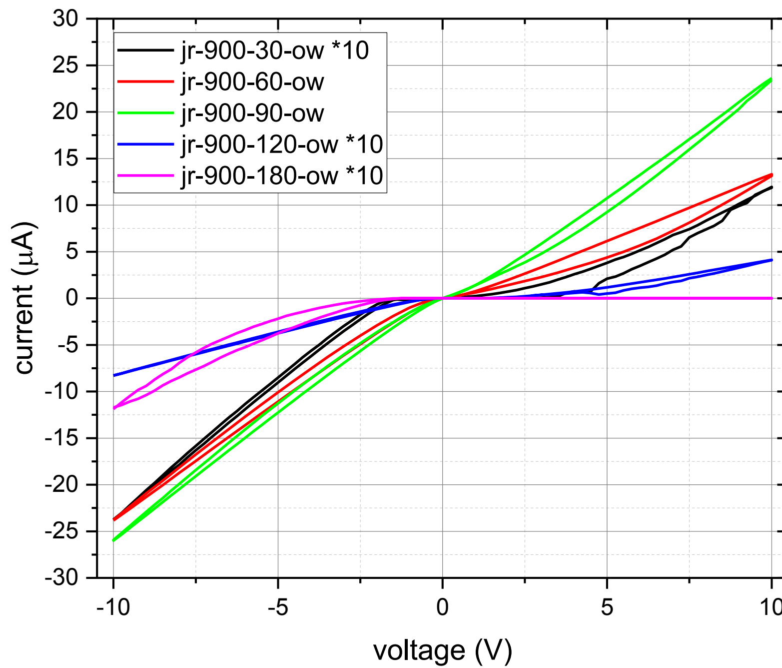

Figure 20. Room temperature IV-curves of samples with DWs created under 900 V in the old wafer crystals after domain wall stabilization. For samples jr-900-30-ow, jr-900-120-ow and jr-900-180-ow current is multiplied by ten for better visualization. The voltage was changed step-wise with ΔU = 0.5 V, Δt = 2 s.

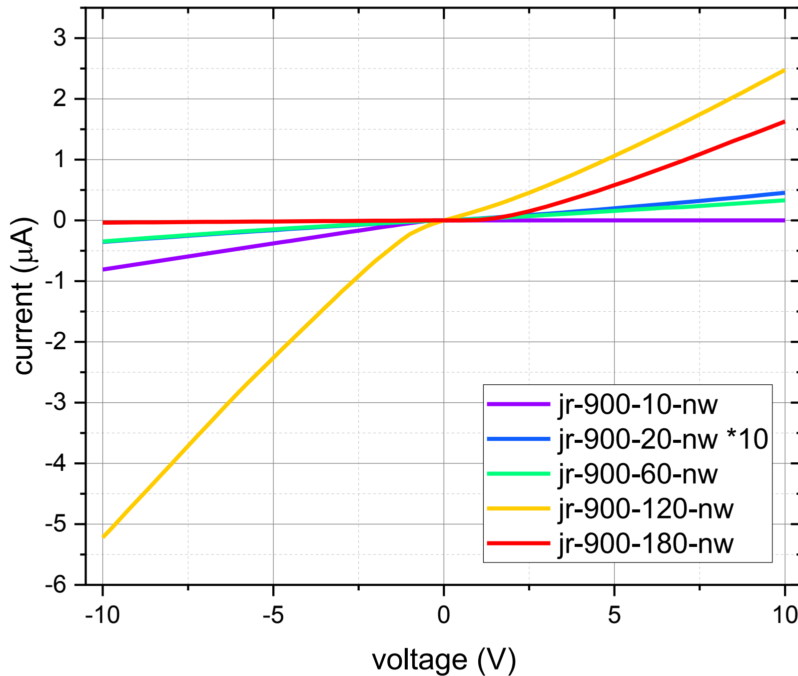

Figure 21. Room temperature IV-curves of samples with DWs created under 900 V in the "new wafer" crystals after domain wall stabilization. For sample jr-900-20-nw current is multiplied by ten for better visualization. The voltage was changed step-wise with ΔU = 0.5 V, Δt = 2 s.

The IV-characteristics of all investigated samples were also obtained earlier by J. Ratzenberger in his master's thesis [69]. Interestingly, the form of the curves in his work is significantly different from the results obtained in this work, in most cases due to removal of the chromium electrodes and deposition of the new electrodes due to degradation of the former. For example, sample jr-900-180-nw was characterized by him as *ohmic* (black line, Fig. 22(c)), but after the reapplication of electrodes, characteristics of the curve demonstrate clear diode-like behavior (blue line); such behavior is in agreement with results presented by Werner et al. [24]. No additional enhancement was conducted. Right after the enhancement with older electrodes, sample jr-900-60-ow was characterized as *diode-like, directional dependent* (Fig. 22(b), black line); after electrodes' reapplication, the character of the curve has not changed, but the maximum current decreased (red line); after 2-hour stabilization on Keithley and no enhancement, the sample demonstrates ohmic characteristics (blue line). Sample jr-900-20-ow (Fig. 22(a), black) has lower conductivity after electrode reapplication and enhancement, but it stayed ohmic in nature. It seems that even after the removal of the electrodes, with which the enhancement procedure was realized, the character of the metal-DW contact can be influenced with high voltages. In the case of the sample jr-800-60-ow (Fig. 22(d), black line), which was characterized as *diode-like, directional dependent*, no manipulation with electrodes was done, however for some reasons the IV-behavior

of the sample have changed. It is not clear, what could have attributed to such a transformation [70].

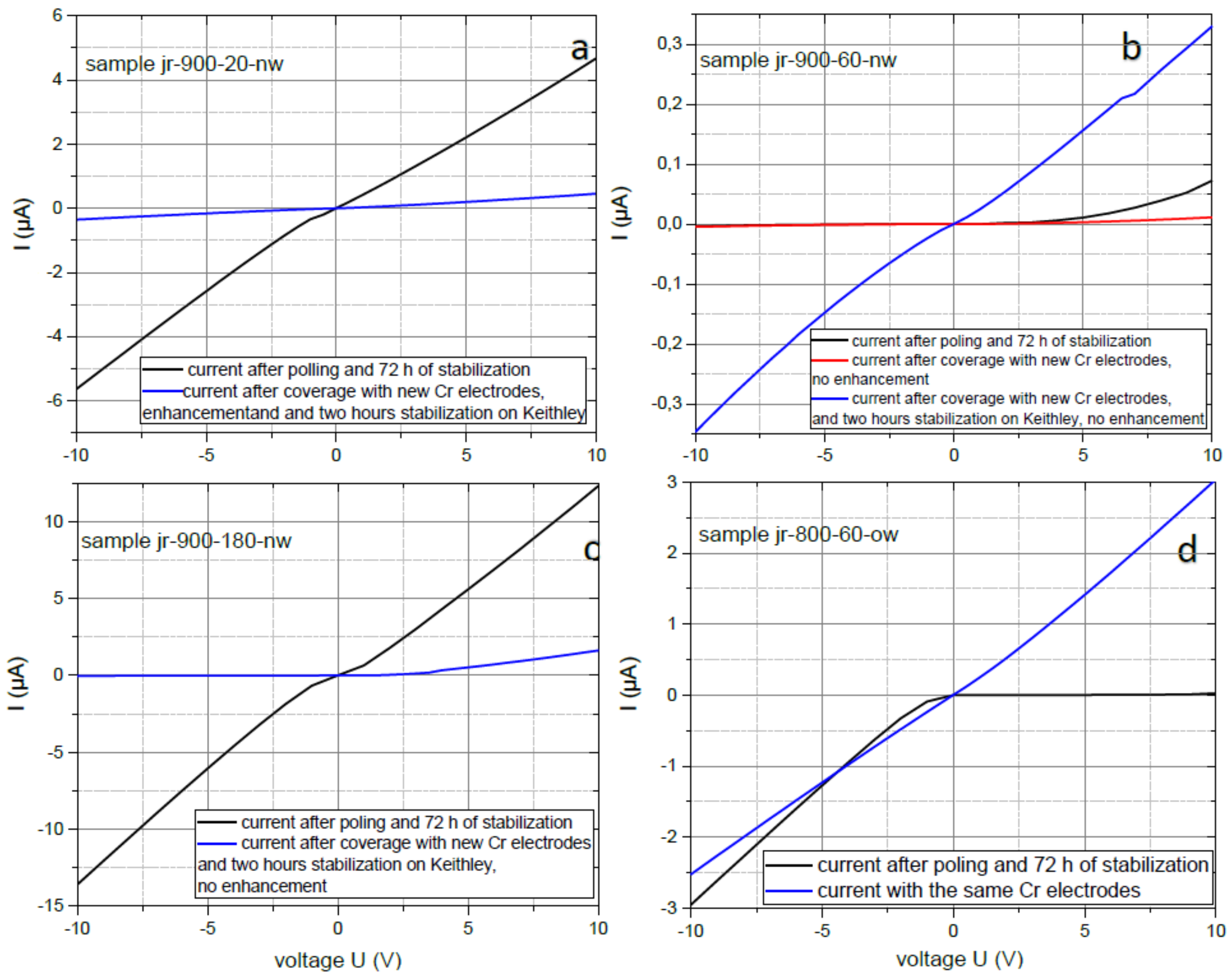

Figure 22. Change of IV-characteristics of samples jr-900-180-nw, jr-900-60-nw and jr-800-60-nw compared to those presented in Julius Ratzenberger's master's thesis (in black) [69]. The voltage was changed step-wise with ΔU = 0.5 V, Δt = 2 s.

In order to investigate how the parameters of the samples have changed, IV-curves of the samples were fitted (Table 1) according to the suggested model (Fig. 6(b))**;** for the samples with reapplied electrodes, parameters of the IV curves before reapplication are also present in the table. The fitting procedure was developed by M. Zahn and thoroughly described in his thesis [15]. The fitting is performed with a trust region reflective algorithm, with a least-squares cost function, implemented in the *python3* library *scipy*.

The suggested model contains diodes – non-linear circuit elements; because of that, the current through the circuit cannot be presented in a form of a closed expression for a fixed voltage.

The problem was resolved by calculating the voltages U_f and U_b (see Fig. 6(b)) using Kirchhoff's current law on these knots: value ($I_{diode} - I_{resistor}$) becomes zero for the optimally chosen value of U:

$$U_f = \arg\min \left| I_{s,f} \left[exp\left(\frac{U - U_{z-}}{U_{c,f}} \right) - 1 \right] - \frac{U_{z+} - U}{R_f} \right|$$

(15)

$$U_b = \underset{U \in (U_{z-}, U_{z+})}{\arg\min} \left| \underbrace{I_{s,b} \left[exp\left(\frac{U - U_{z+}}{U_{c,b}} \right) - 1 \right]}_{I_{diode,\, b}} - \underbrace{\frac{U_{z-} - U}{R_b}}_{I_{resistor,\, b}} \right|$$

After the determination of the potentials U_f and Ub, the current in two branches was calculated using the Ohm's law for the resistor.

Table 1. Parameters from the equivalent circuit model (**Fig. 6(b)** and **eqn. (15),** both duplicated below) obtained by fitting the room temperature IV-curves of **Figures 19-21.** Results in gray are untrustworthy (and cannot be fitted better) and thus should not be taken into account. Results for the DWs before electrode reapplication are indicated in blue. The samples with inclined domain walls are marked in green; the DWs of the remaining samples are imploded.

$$U_{f(b)} = \arg\min \left| I_{s,f} \left[exp\left(\frac{U - U_{z-(+)}}{U_{c,f(b)}} \right) - 1 \right] - \frac{U_{z+(-)} - U}{R_{f(b)}} \right|$$

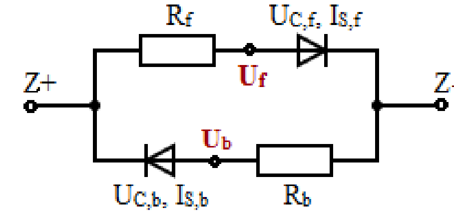

Sample	R_f [MΩ]	$I_{s,f}$ [pA]	$U_{c,\,f}$ [V]	R_b [MΩ]	$I_{s,b}$ [pA]	$U_{c,\,b}$ [V]
jr-800-60-ow	2.802±0.002	$(4.39\pm0.02)\cdot10^5$	0.729±0.003	3.530±0.005	$(4.4\pm0.2)\cdot10^3$	0.424±0.003
jr-800-90-ow	4.440±0.003	$(2.27\pm0.01)\cdot10^5$	0.0277±0.0005	4.034±0.002	$(1.1\pm1.4)\cdot10^{-6}$	0.036±0.002
jr-800-120-ow	3.311±0.003	0.01±0.02	0.029±0.003	3.222±0.003	149.6±2.7	0.044±0.001
jr-800-180-ow	0.379±0.001	35.85±0.45	1.017±0.002	122±388	$(1.357\pm138)10^{-5}$	0.5±4
jr-900-30-ow	4.53±0.01	$(2.36\pm0.02)\cdot10^4$	0.456±0.006	3.260±0.002	13.9±2	0.190±0.008
jr-900-60-ow	0.682±0.001	$(6.6\pm1.3)\cdot10^3$	0.140±0.004	0.3795±0.0002	$(2.04\pm0.04)\cdot10^5$	0.197±0.001
jr-900-90-ow	0.2650±0.0004	$(1.74\pm0.02)\cdot10^6$	1.475±0.006	0.3385±0.0004	$(4.5\pm0.1)\cdot10^5$	0.440±0.003
jr-900-120-ow	13.78±0.01	$(1.17\pm0.03)\cdot10^3$	0.735±0.003	10.736±0.008	$(1.52\pm0.04)\cdot10^3$	0.179±0.001
jr-900-180-ow	$10^7\pm0$	$2\cdot10^9\pm4\cdot10^{16}$	$4\cdot10^{14}\pm4\cdot10^{21}$	5.60±0.06	$(6\pm2)\cdot10^2$	0.45±0.03
jr-900-10-nw	6877 ± 0	10^{-8}	$2\cdot10^{-16}$	11.562 ± 0.002	25.2 ± 1.9	0.0635 ± 0.0005
jr-900-20-nw (before reap.)	1.973±0.003	$(5.0\pm0.1)\cdot10^5$	0.359±0.004	1.59±0.001	102±17	0.170±0.002
jr-900-20-nw	176.2±0.2	$(3.68\pm0.04)\cdot10^3$	0.819±0.004	239.9±0.5	82.2±1.8	0.408±0.001
jr-900-60-nw (before reap.)	286±46	30±24	1.0±0.2	1681±43	29.5±6.6	1.03±0.05
jr-900-60-nw	25.43±0.06	$(5.35\pm0.22)\cdot10^4$	0.83±0.01	21.77±0.08	952±145	0.636±0.007
jr-900-120-nw	3.015 ± 0.007	$(1.79\pm0.02)\cdot10^5$	0.972±0.003	1.590 ± 0.003	$(2.2\pm0.1)\cdot10^4$	0.367±0.006
jr-900-180-nw (before reap.)	0.775±0.001	$(1.6\pm0.2)\cdot10^4$	0.167±0.002	0.692±0.002	$(2.04\pm0.18)\cdot10^4$	0.2±0.1
jr-900-180-nw	4.30±0.01	3027±109	0.476±0.002	248.7±15.3	1±9	0.15±0.15

First of all, just like in Zahn's work [15], resistances both in forward and backward direction for all samples are on the order of several MΩ. For the first batch we can see that there is no dependence between the exposure time in the poling procedure (and consequently, the size of the domain) and the value of the resistance both in positive and negative direction, i.e., in this case we cannot precisely influence that parameter. If we compare the samples produced from the same wafer, but under the two different poling voltages (800 V vs. 900 V), we observe that on average (in two out of the three cases, where comparison is possible), the intrinsic conductivity of the DWs (parameters R_f and R_b) produced under higher voltages tend to be less resistive; the number of the samples, however, does not allow us to make an unequivocal conclusion.

For the "900-V-new-wafer" batch where chromium electrodes have been reapplied, we can make several observations. First of all, for the samples that did not undergo repeated enhancement (jr-900-60-nw and jr-900-180-nw), the resistances both in positive and negative directions have changed. Such results allow us to give some physical interpretation to the model in the Fig. 6(b), namely, the resistance values of the model consist of two components, one being the surface (or contact) component and the other being the bulk component; consequently, one resistor in each branch could be substituted by two resistors, connected in series, respectively. Secondly, the only domain wall of all specimen with re-applied electrodes, which has not been imploded (neither in the first enhancement, nor in the second) – jr-900-20-nw – after electrode reapplication demonstrates the current two orders of magnitude lower than before. Imploded samples jr-900-60-nw and jr-900-180-nw tend to demonstrate a current of the same order of magnitude as they used to before electrode reapplication, even without second enhancement. This motivates the picture of a statistical connection between DW and contact electrode that averages out in case of a huge number of domain walls. Thirdly, there seems to be no correlation between the parameters (and even the character of the curves) before and after electrode reapplication. This leads to the conclusion that surface processes (e.g., metal electromigration or the electrode deposition conditions) and enhancement play a much bigger role than poling conditions.

Just like in ref. [15], the saturation current I_s turned out to be the parameter with largest variation of five orders of magnitude; no correlation between I_s and any other parameter can be observed.

The characteristic voltage of the diode in the equivalent circuit is a parameter that allows to gain some quantitative insight into the physical characteristics of DWs: $U_c = nk_BT/q$, where n is the ideality factor, a parameter, which in case of DW is related to the number of free charge carriers (for conventional semiconductor diodes this value is usually between 1 and 2, but there is no upper limit if charge carrier concentration is high). Here, the minimum value is 1.1, maximum is 57. Using the formula $n = \frac{q\hbar}{2k_BT}\sqrt{\frac{N_d}{m^*\varepsilon}}$ [27], with $m^* = m_0m_r$ – effective mass of electrons and $\varepsilon=\varepsilon_0\varepsilon_r$ – dielectric permittivity; for LNO $m_r\varepsilon_r = 1.7$ [15]. Maximum and minimum values of charge carrier concentration for the investigated samples are $N_{d,\,max} \approx 10^{21}$ cm^{-3} (sample jr-900-90-ow, forward direction) and $N_{d,\,min} = 10^{19}$ cm^{-3} (sample jr-800-90-ow, forward direction). These values are at expected order of magnitude, and correspond to the values obtained both in [15] and those obtained in theoretical calculations by Eliseev et al. [71].

In order to practically counter-check both the suggested model presented in Fig. 6(b), and the fitting procedure, equivalent electrical circuits with the characteristics of two LNO samples were physically constructed from commercially available resistors and diodes. For that purpose samples jr-800-90-ow and jr-800-120-ow were chosen, since parameters of its circuit elements (diodes in particular) are quite close to commercially available (ideality factor *n* between 1 and 2, and $I_{s,n}$ in the region of hundreds nA). Comparison of the IV-curves of circuits built from commercially available elements and IV-curve of the both samples can be seen on the Fig. 23.

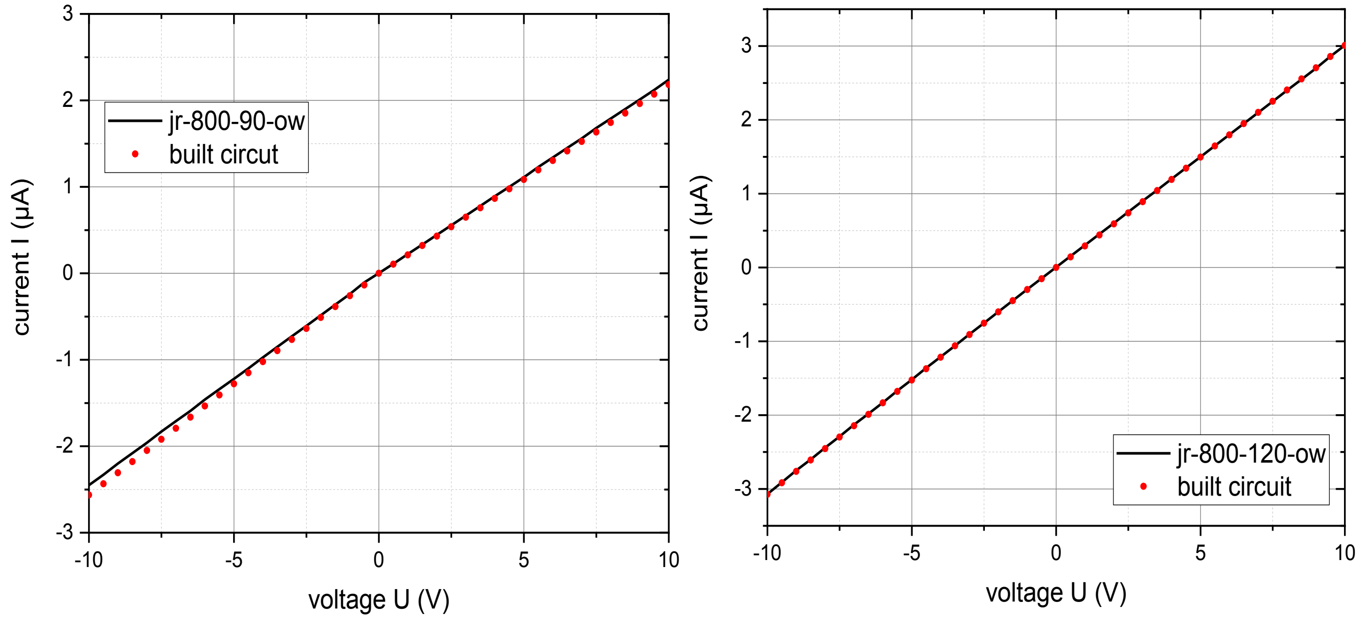

Figure 23. Comparison of IV-curves of the jr-800-90-ow and jr-800-120-ow samples, and the circuit built from commercial resistors and diodes. The voltage was changed step-wise with ΔU = 0.5 V, Δt = 2 s.

Sample jr-800-90-ow was emulated with three resistors and two diodes, connected as in Fig. 1: R_f = 4.4 (two resistors of 2.2 MΩ, connected in series), R_b = 3.9 MΩ, Schottky diode BAT43 ($I_{s,\,f}$ = 200 nA) and diode 1N4148 ($I_{s,\,b}$ = 5 μA – that quantity was poorly defined for this sample, thus a simulation diode with larger variation of that parameter would fit). Sample jr-800-120-ow was emulated with two resistors with R_f = R_b = 3.3 MΩ and diodes BAT43 ($I_{s,\,b}$= 200 nA vs. 0.15 nA for the sample – two orders of magnitude higher) and 1N4148 ($I_{s,\,b}$ = 5 μA – quantity poorly defined for the sample).

As can be seen from the Fig. 23, samples demonstrate *ohmic* curves almost identical to those of the physical equivalent circuits. Properties of such circuits are defined by the characteristics of resistors; characteristics of diodes can be varied by several orders of magnitude. Unfortunately, those sample that demonstrate clear non-linearity, cannot be emulated by a circuit, that include commercially available diodes mainly due to their very high ideality factor $n > 10$. Nevertheless, the above experiment demonstrates, that the model, suggested by Zahn does not contradict experimental results for LNO domain walls.

It is evident from the obtained results, that the suggested model provides excellent accuracy and flexibility in describing the charge transport through the created samples, as it was

demonstrated on a statistically significant number of samples prepared under varying conditions, and from the comparison between current-voltage characteristics of two samples and the physical equivalent circuits, built from the commercially available resistors and Schottky diodes with comparable characteristics. Significant influence of the interface between the DW and the metal electrode on all the parameters of the sample was found during the electrode re-application process; it is not clear, which controllable conditions of the production process define the transport characteristics through the interface, however. Before appropriate investigations of this issue can start, it is necessary to understand, whether the poling setup and the poling/DWC-enhancement procedures, recently developed by J. Ratzenberger [69], allow the creation of samples with reproducible characteristics, since all of the above samples have demonstrated great variation in the numerical parameters, mainly due to the implosion.

4.2 Reproducibility of the Domain Walls Produced with Laser-Assisted Poling

Since in the previous section no correlation between the poling pulse length and the conductivity of the domain wall was found, it is necessary to further check the reproducibility of laser-assisted poling method. In this section, three batches of samples are investigated; all the samples were produced from the "new" wafer employed in the previous section. The poling voltage for the three batches was 800 V; in order to gather statistical information on the influence of the pulse length, samples in the first batch were produced under 30 s laser pulse length; 5 samples in the second and 5 samples in the third batch were produced with the pulse length of 120 s; before the electrode deposition, the samples were cleaned with DI water; isopropanol, and acetone as it is described in the experimental section; here it is signified as "regular cleaning". The first pulse length was chosen based due to the fact that this pulse length was found out to be an optimal one by J. Ratzenberger in his thesis [69]; 120 s were chosen due to the fact that all the samples produced under the 180 s pulse length had monodirectional (rectifying) IV characteristic, which might be inflexible for hypothetical commercial application. Also, the sample jr-800-120-ow has a remarkably "linear" curve in the sense that higher harmonic current contribution could not be detected during the AC conductivity measurements, as can be seen from the following section. In order to investigate the influence of the surface's cleanness (e.g., nascence of carbon contamination layer) on the domain wall near the surface of the sample and on the metal-DW contact, samples in the third batch in addition to the regular cleaning with DI water and organic solvents were etched in the oxygen plasma for 5 minutes on each side; consequently, 150 nm of the material was etched

from both sides of a sample and carbon contamination layer is fully removed. IV curves of the investigated samples are presented in the Fig. 24; parameters of the samples according to the model presented on the Fig. 6(b) and eqn. (15) are summarized in the Table 2.

During the measurement and enhancement process one of the samples from each batch (800_30_reg_clean_3, 800_120_reg_clean_1, and 800_120_plasma_clean_2) has demonstrated a lower conductivity and the IV curve that was significantly different from all the other samples in the batch; for all these samples, the same sample holder, through which the sample was connected to Keithley 6517B, was used; it is possible, that it was defunct and all the difference were caused by this fact; in the Table 2 these samples are marked with yellow.

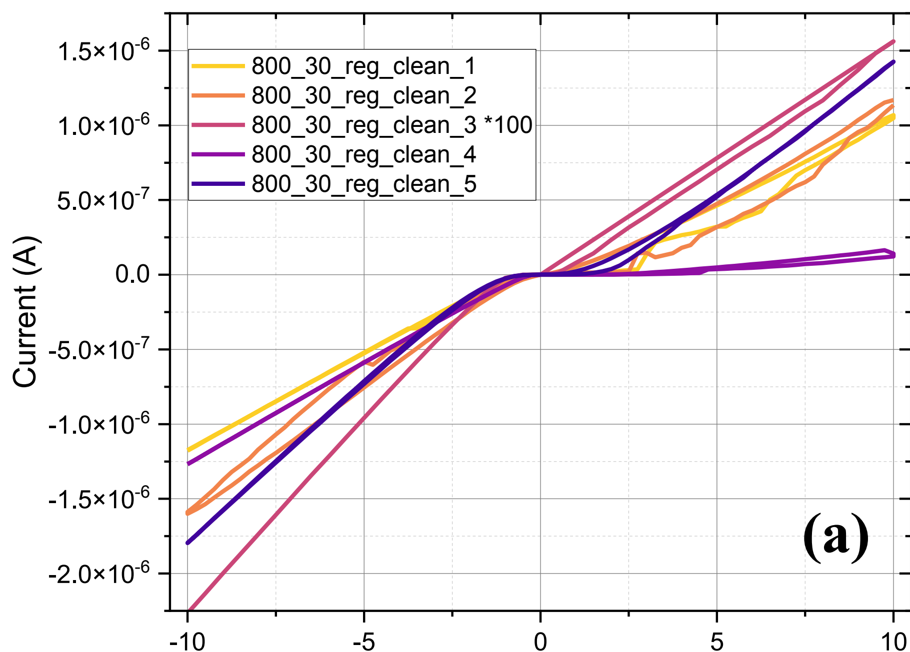

Figure 24. IV curves of the three batches of LNO samples: (a) samples produced under the poling voltage of 800 V and a 30-seconds pulse length, and regular cleaning of the surface before the electrode deposition with DI water and organic solvents; current of the third sample was enlarged by two orders for better visualization; (b) samples produced under the poling voltage of 800 V and a 120-seconds voltage pulse length, regularly cleaned; current of the first sample was multiplied by 100 for better visualization; (c) samples produced under the poling voltage of 800 V and a 120-seconds voltage pulse length, with +z- and –z-sides etched in oxygen plasma for 5 minutes in addition to the regular cleaning; the current of the third sample was multiplied by 10 for better visualization. The voltage was changed step-wise with ΔU = 0.25 V, Δt = 2 s.

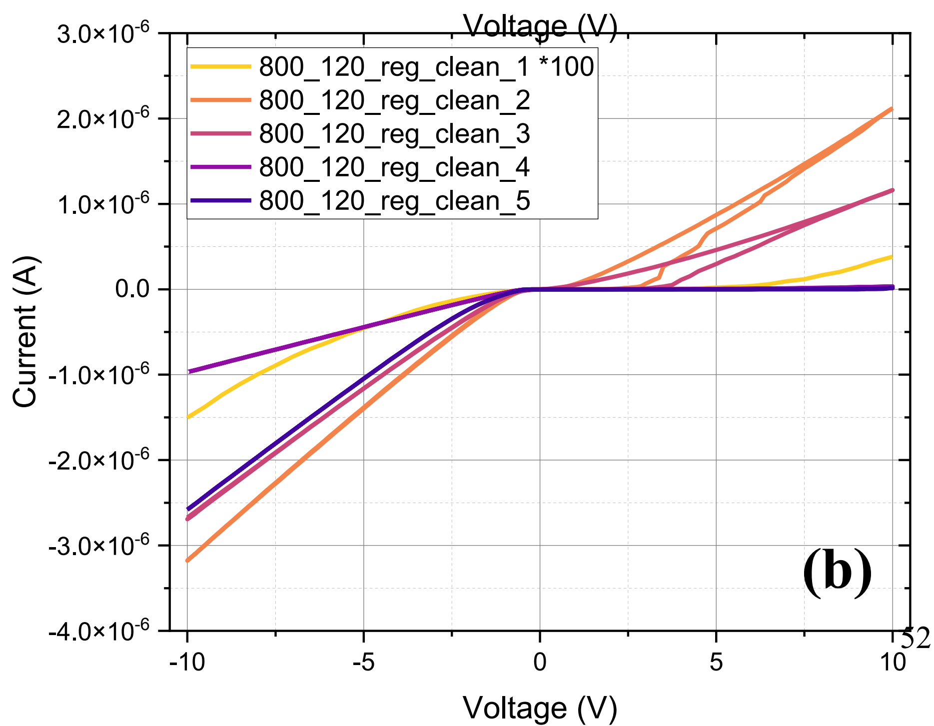

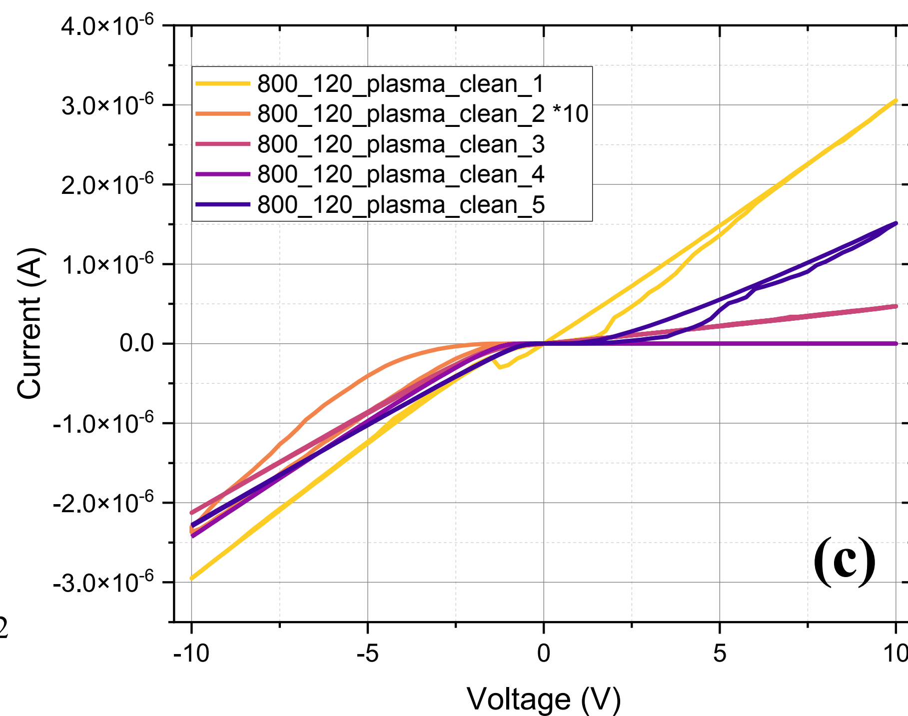

Table 2. Parameters for equivalent circuit (**Fig. 6(b)** and **eqn. 15**, duplicated below) model obtained by fitting the room temperature IV-curves (**Figure 24 (a-c)**). Results in gray are untrustworthy (and cannot be fitted better) and should not be taken into account. All the samples DWs are inclined (not "imploded"). Average values of equivalent circuit parameters are marked with blue (dash line means that the parameters are too variant to calculate a reliable mean value). The samples, that significantly differ from the other samples in the batch (possibly due to defunct sample holder) are marked with yellow and are not included in averaging.

$$U_{f(b)} = \arg\min \left| I_{s,f} \left[exp\left(\frac{U - U_{z-(+)}}{U_{c,f(b)}} \right) - 1 \right] - \frac{U_{z+(-)} - U}{R_{f(b)}} \right|$$

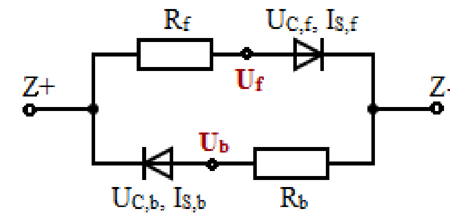

Sample	R_f [MΩ]	$I_{s,f}$ [pA]	$U_{c,f}$ [V]	R_b [MΩ]	$I_{s,b}$ [pA]	$U_{c,b}$ [V]
800_30_reg_clean_1	7.73	$1.86 \cdot 10^4$	0.43	7.61	2.40	0.093
800_30_reg_clean_2	5.53	$1.08 \cdot 10^5$	1.42	5.52	$1.70 \cdot 10^3$	0.24
800_30_reg_clean_3	$6.10 \cdot 10^2$	1.61	0.08	$3.68 \cdot 10^2$	5.85	0.20
800_30_reg_clean_4	38.6	27.7	0.42	7.26	$1.09 \cdot 10^3$	0.12
800_30_reg_clean_5	4.97	$1.10 \cdot 10^4$	0.60	4.48	$5.78 \cdot 10^2$	0.25
Average value	6.08±1.35	-	0.72±0.46	6.22±0.90	-	0.18±0.06
800_120_reg_clean_1	$6.70 \cdot 10^2$	$1.90 \cdot 10^{-2}$	0.62	$4.10 \cdot 10^2$	$1.67 \cdot 10^2$	0.94
800_120_reg_clean_2	3.76	$1.94 \cdot 10^4$	0.46	2.72	$3.92 \cdot 10^3$	0.21
800_120_reg_clean_3	5.72	$7.86 \cdot 10^4$	1.24	3.16	$3.76 \cdot 10^3$	0.28
800_120_reg_clean_4	116.5	$5.32 \cdot 10^{-2}$	0.46	9.39	33.5	0.088
800_120_reg_clean_5	10^{14}	10^{32}	0.009	3.08	$3.03 \cdot 10^3$	0.30
Average value	-	-	0.70±0.31	4.59±2.72	$(2.68 \pm 1.53) \cdot 10^3$	0.22±0.08
800_120_plasma_clean_1	3.20	$2.97 \cdot 10^4$	0.063	2.82	$1.64 \cdot 10^3$	0.23
800_120_plasma_clean_2	$2.87 \cdot 10^4$	10^{-8}	10^{20}	30.7	12.6	0.26
800_120_plasma_clean_3	20.2	$4.90 \cdot 10^4$	0.33	3.87	35.9	0.18
800_120_plasma_clean_4	$3.23 \cdot 10^{11}$	10^{-8}	$2.09 \cdot 10^{17}$	3.32	$2.50 \cdot 10^2$	0.21
800_120_plasma_clean_5	4.72	$3.64 \cdot 10^3$	0.47	3.89	$8.10 \cdot 10^2$	0.14
Average value	9±8	$(2.7 \pm 2.1) \cdot 10^4$	0.29±0.19	3.48±0.43	684±607	0.19±0.03

As seen from the data, no dependence between the resistance of the DW and the length of the poling voltage pulse (and consequently, the size of the domain and contact area) exists – for the DWs grown under the voltage pulse of lengths 30 s and 120 s – both regularly cleaned and plasma etched – resistance of the walls is around 4-6 MΩ. Taking into account the big confidence interval, stemming from comparatively small number of samples, we can make the conclusion that the size of the domain wall (a value proportional to the pulse length) has very weak or even zero influence on the conductivity of the sample. As c-AFM measurements of DWC by Godau et al. [6] showed, not all sections of the domain wall are equally conductive, hence it is reasonable to conclude from the fact that charge transport occurs only in small areas with larger inclination angle α, such as either in the corners of the domain, or at somewhat random sections of the domain wall outside of corners, that the size of such a section does not vary much for all the DWs produced with the laser-assisted method and enhanced using the Godau method.

The saturation current I_s for all the samples is still the quantity with the highest variation among samples, up to six orders of magnitude ($I_{s,f}$ for the batch of the regularly cleaned samples produced under 120 s pulse length). Since in the Schottky diode this quantity depends on the cross-section area, carrier concentration, diffusion coefficients of the carriers inside the material, and various barrier properties (e.g., height and width), such a high variation of this parameter in the obtained samples may be evidence of the insufficiently clean conditions with a large number of uncontrolled parameters, such as air humidity and temperature during the production of the barrier for the reproducibility of the results. The characteristic voltage U_C of the produced samples demonstrates satisfactory reproducibility among all batches, especially for the backward direction; the mean value around 0.20 V corresponds to the concentration of charge carriers of approximately 10^{20} cm^{-3}. It can be also seen from the parameters in Table 2 that the characteristic voltage U_C of the Schottky barrier on – z-side of LNO is lower, than the same quantity on the +z-side of the crystal (0.2 V and 0.72 V respectively). The same observation was made by M. Zahn in his work [15] and is also true for the majority of the samples in the Table 1, although some exceptions to the rule exist, e.g., samples jr-800-120-ow and jr-900-60-ow. Such a differences probably stem from the electrostatic difference between LNO surfaces with opposite polarities (see the literature review section), with ionization energy of +z-side being almost 2 eV higher than for –z-side. It is reasonable to assume that such electrostatic differences at surfaces may play an important role in the characteristics of the Schottky barrier; consequently, asymmetry of the IV-curve of the DW-

metal electrodes system is an inherent property. It is unclear, however, why some of the samples (e.g., sample 800_120_plasma_clean_1) tend to demonstrate the opposite properties, and whether it is caused by some of the controllable parameters during the sample preparation, or perhaps the local surface properties in the vicinity of the DW.

The comparison between the second and the third batch (samples produced under 120 sec pulse length regularly cleaned and etched in the oxygen plasma, respectively) shows, that etching of a surface with already existing domain wall has no significant influence on the metal-DW contact after the DWC enhancement process. It seems that the layer of carbon compounds, always present on the LNO surface, has no significant influence on the formed Schottky barrier either. Before the enhancement procedure (see graphs in the Appendix A), however, current-voltage characteristics of the plasma-etched samples have exclusively rectifying diode-like features. As it was previously described, the near-surface structure of the DWs is very sensitive to both polarization of the surface (+z or −z) and the depolarization field in the vicinity of the surface. Supposedly, the etching has changed inclination of the DW (probably up to a point of a very poor contact with the LNO surface) and/or the width of the DW, which has led to such diode characteristics. The DWC enhancement procedure, however, fully eliminated the difference between the differently prepared samples; consequently, we can make an assumption, that the influence of a high negative voltage on the near-surface structure of the DW is significant, up to a point where it can define the character of the device (rectifying/bi-directional). Unfortunately, due to the lack of suitable analysis methods, it is very hard to investigate this near-surface structure in absolute details; here, we can only speculate that the smaller the difference between the near-surface and bulk structures of the DW (and hence the weaker the widening of the DW), the lower the potential barrier on the interface is formed.

In conclusion of this section, it can be said that the *relative* reproducibility of the samples in the laser-assisted poling setup indeed occurs, in the sense that for most of the samples both forward and backward resistances R are in the range of 4-6 MΩ and the average characteristic voltages U_C of backward and forward diodes are ~0.2 V and ~0.7 V respectively; consequently, the absolute value of the current at ±10 V is a few µA for most of the samples. Still, it is unclear, why some of them (800_120_reg_clean_5 and 800_120_plasma_clean_4) demonstrate rectifying IV curve as opposed to the bi-directional curve of the other samples. Here, we can again return to the somewhat random surface conductance distribution (which is heavily correlated with the near-surface DW-

inclination angle), described by Godau [6]; one of the possible explanations for such randomness is the electric field inhomogeneity, stemming from the metal layer grain boundaries. In the following section, after the repetition of the electrode re-deposition experiment under controllable conditions, the influence of electric fields at various magnitudes will be investigated; then, liquid electrodes (a substance, being drastically different in its electrical and material properties from the solid metal) will be utilized for the DWC-enhancement procedure; evidently, the application of such a material without grain boundaries will allow us to eliminate the influence of inhomogeneities on the near-surface structure of the DW.

4.3 Electrode Re-Deposition Influence on the Schottky Barrier

As it was shown in the section 4.1, re-application of electrodes can drastically change the IV curve of the sample; this result, however, was demonstrated mostly on the imploded DWs (three samples), and only on one regular inclined DW. Here, the reapplication results will be compared for five samples with inclined DWs from the third batch (produced with poling pulse length of 120 s and plasma etched before electrode deposition, since DC conductivity between the samples in this batch was the closest to each other).

Previously deposited chromium electrodes were chemically removed; afterwards, the samples were cleaned with the standard technique, utilized before electrode deposition and described in the experimental section. After the deposition, the DC conductivity of the samples was measured (in red; Fig. 25); only samples 800_120_plasma_clean_1, 800_120_plasma_clean_3 and 800_120_plasma_clean_5 have demonstrated clear current voltage dependence in the range of $10^{-7} – 10^{-6}$ A; for the samples 800_120_plasma_clean_2 and 800_120_plasma_clean_4 current was in the range of pA and lower, with no clear dependence on the voltage. It seems that for the latter samples, the metal-DW contact was very poor, and hence no current was detected; consequently, only the samples 1-3-5 will be discussed further. As can be seen from the Fig. 25, the IV characteristics of some samples, just like in the section 4.1, has noticeably changed. In Table 3 the comparison between the saturation currents, characteristic voltages, and resistances in both directions can be seen. The sample 800_120_plasma_clean_1 is somewhat peculiar, since its IV characteristics before and after electrode reapplication remained mostly unchanged. Changes in IV characteristics of samples 800_120_plasma_clean_3 and 800_120_plasma_clean_5 are much more noticeable; conductivity of the sample 5 has decreased by approximately one order of magnitude; all the samples, however, have remained bidirectional in their nature.

Taking into account the fact that the depolarization field on the surface of LNO has a great influence on the structure of the domain wall near the surface, and both application and removal of metal electrodes change this field drastically, an attempt to "correct" the domain structure near the surface by applying a comparatively low voltage of –100 V only was made; the IV curves of the samples after application of this "corrective" voltage are plotted in red in the Fig. 25. For all the samples, the substantial change in both the diode and resistor characteristic took place (see Table 3), compared to the characteristics obtained immediately after electrode re-deposition. In case of sample 800_120_plasma_clean_1, which IV curve after electrode reapplication almost coincided with its original curve, the conductivity has somewhat decreased; in case of the samples 800_120_plasma_clean_3 and 800_120_plasma_clean_5, their conductivity has increased and became comparable with that of an original curve, although the diode characteristics have remained noticeably different, up to a point where the negative branch of the sample 800_120_plasma_clean_3 could not be fitted according to the suggested model. Judging on these results, it seems that the process, which largely defines the resulting features of the DC conductivity is the enhancement process itself, suggested by Godau et al. [6]. In his Master's thesis, J. Ratzenberger has found out, that the limiting factor in this process is the current (it should not exceed than 10^{-5} A, otherwise the domain "implodes"); however, no unified procedure has been developed yet; e.g., no optimal voltage ramp or optimal value of the stabilization time, at which the domain is kept under the maximum negative voltage during the DWC enhancement procedure and during which the current can change by several orders of magnitude, was found. Additionally, as the example of the sample 800_120_plasma_clean_1 demonstrates exemplarily, the near-surface structure of the DW can be quite sensitive to the enhancement voltages of values several times lower than the maximum enhancement voltage. Consequently, further investigations of the process, preferably supplemented by CSHG imaging are necessary; existing techniques, employed by Kirbus et al. [7] are an excellent tool to achieve this. The results for the sample 800_120_plasma_clean_1 suggest that a finer tuning of the near surface wall parameters can be done by application of "medium" voltages, around 40 V for samples of 200 µm thickness. This is coincides with the threshold electric field of 2 kV/cm, reported, the literature [53], at which the walls start to move. According to the same paper, the DWs of higher thickness (which applies to the near-surface DW structure) have a lower threshold electric field.

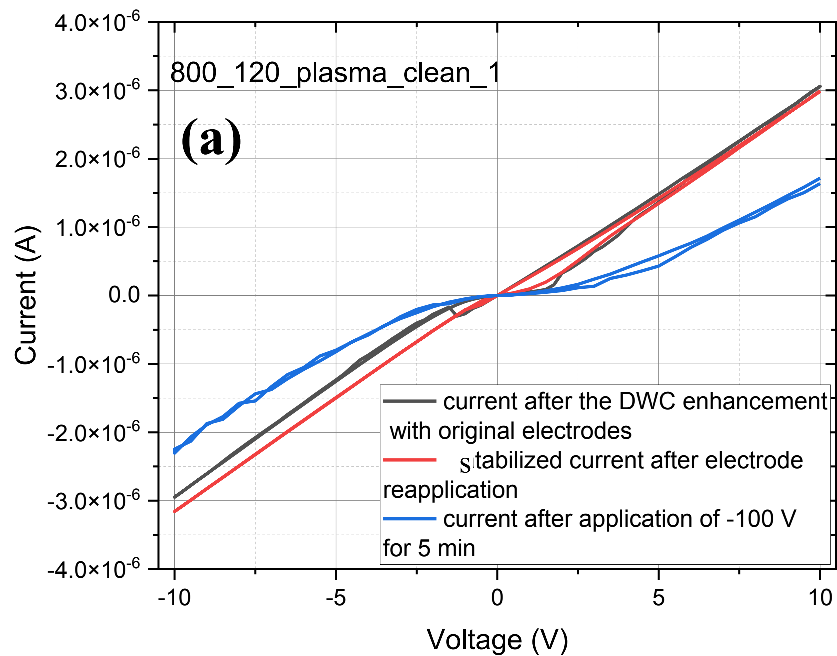

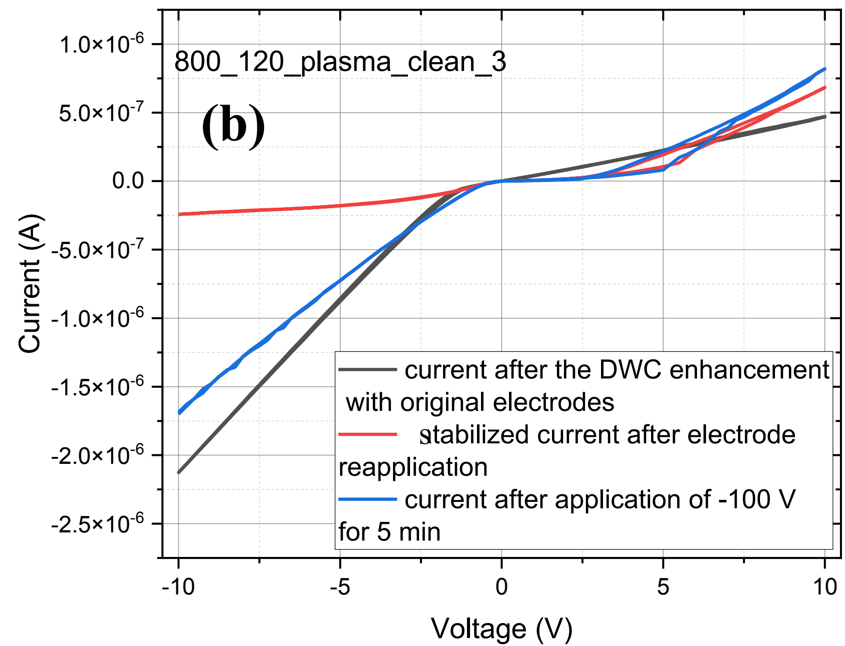

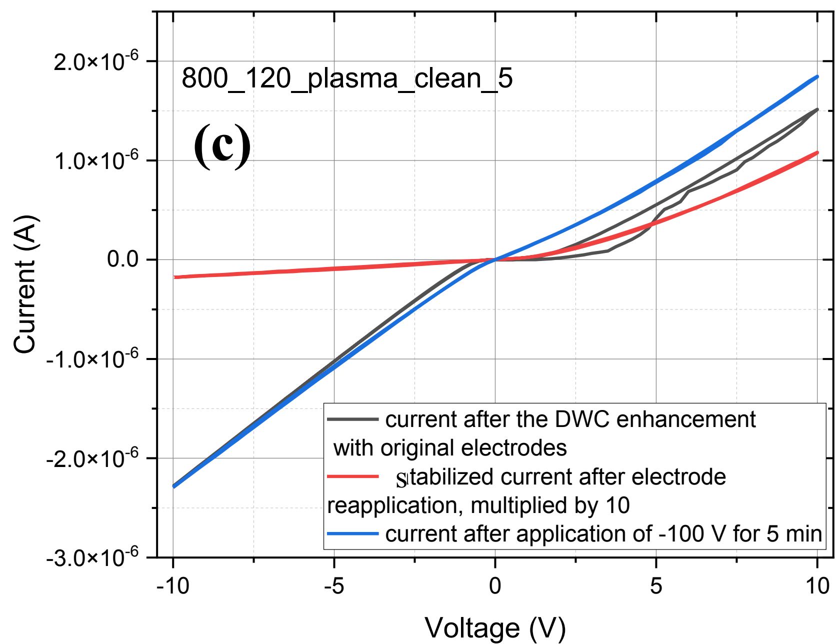

Figure 25. Change of the original IV-characteristics of samples 800_120_plasma_clean_1 (a), 800_120_plasma_clean_3 (b), 800_120_plasma_clean_5 (c) (in black), after chromium electrode reapplication (in red) and application of -100 V for 5 min to the samples. The voltage was changed step-wise with ΔU = 0.25 V, Δt = 5 s.

Table 3. Parameters for equivalent circuit model obtained by fitting the room temperature IV-curves (**Fig. 25 (a, b, c)**) of the samples poled under 120 s pulse length and cleaned in oxygen plasma before original electrode deposition according to the suggested circuit model (**Fig. 6(b)** and **eqn. (15)**, both duplicated below). White lines correspond to original IV curves, taken from the Table 2, lines marked in pink correspond to the IV curves obtained after electrode reapplication and the lines marked in blue are IV curves obtained after application of -100 V for 5 min.

$$U_{f(b)} = \arg\min \left| I_{s,f} \left[exp\left(\frac{U - U_{z-(+)}}{U_{c,f(b)}} \right) - 1 \right] - \frac{U_{z+(-)} - U}{R_{f(b)}} \right|$$

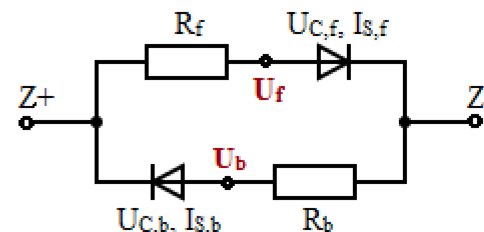

Sample	R_f [MΩ]	$I_{s,f}$ [pA]	$U_{c,f}$ [V]	R_b [MΩ]	$I_{s,b}$ [pA]	$U_{c,b}$ [V]
800_120_plasma_clean_1	3.20	$2.97 \cdot 10^4$	0.063	2.82	$1.64 \cdot 10^3$	0.23
after electrode reapplication	3.07	$3.52 \cdot 10^5$	0.38	2.94	0.52	0.11
after application of -100 V for 5 min	3.47	$2.91 \cdot 10^4$	1.01	3.06	$1.03 \cdot 10^4$	0.60
800_120_plasma_clean_3	20.2	$4.90 \cdot 10^4$	0.33	3.87	35.9	0.18
after electrode reapplication	9.01	$1.91 \cdot 10^2$	0.48	34.4	$3.83 \cdot 10^3$	-
after application of -100 V for 5 min	7.79	34.9	0.37	5.11	$8.67 \cdot 10^3$	0.29
800_120_plasma_clean_5	4.72	$3.64 \cdot 10^3$	0.47	3.89	$8.10 \cdot 10^2$	0.14
after electrode reapplication	57.3	$1.31 \cdot 10^3$	1.00	$5.99 \cdot 10^2$	$6.68 \cdot 10^3$	0.002
after application of -100 V for 5 min	3.74	$2.31 \cdot 10^5$	1.45	3.85	$2.63 \cdot 10^4$	0.47

4.4 Electrode Influence on the Processes of Poling, DWC Enhancement, and Charge Transport

4.4.1 Influence of the Electrode Material on the Schottky Barrier Parameters

As was previously discussed, the electrode material is usually one of the main defining parameters of the Schottky barrier, mainly because of the differences in the work function of the metals. Other factors, such as chemical reaction between a metal and substrate, interdiffusion, the quality of the metal layer, etc., should be also taken into account. In this section, the influence of the electrode material on the Schottky barrier characteristics will be investigated. The first material discussed in this section are the liquid electrodes, comprised of the water solution of NaCl, employed in the poling process themselves.

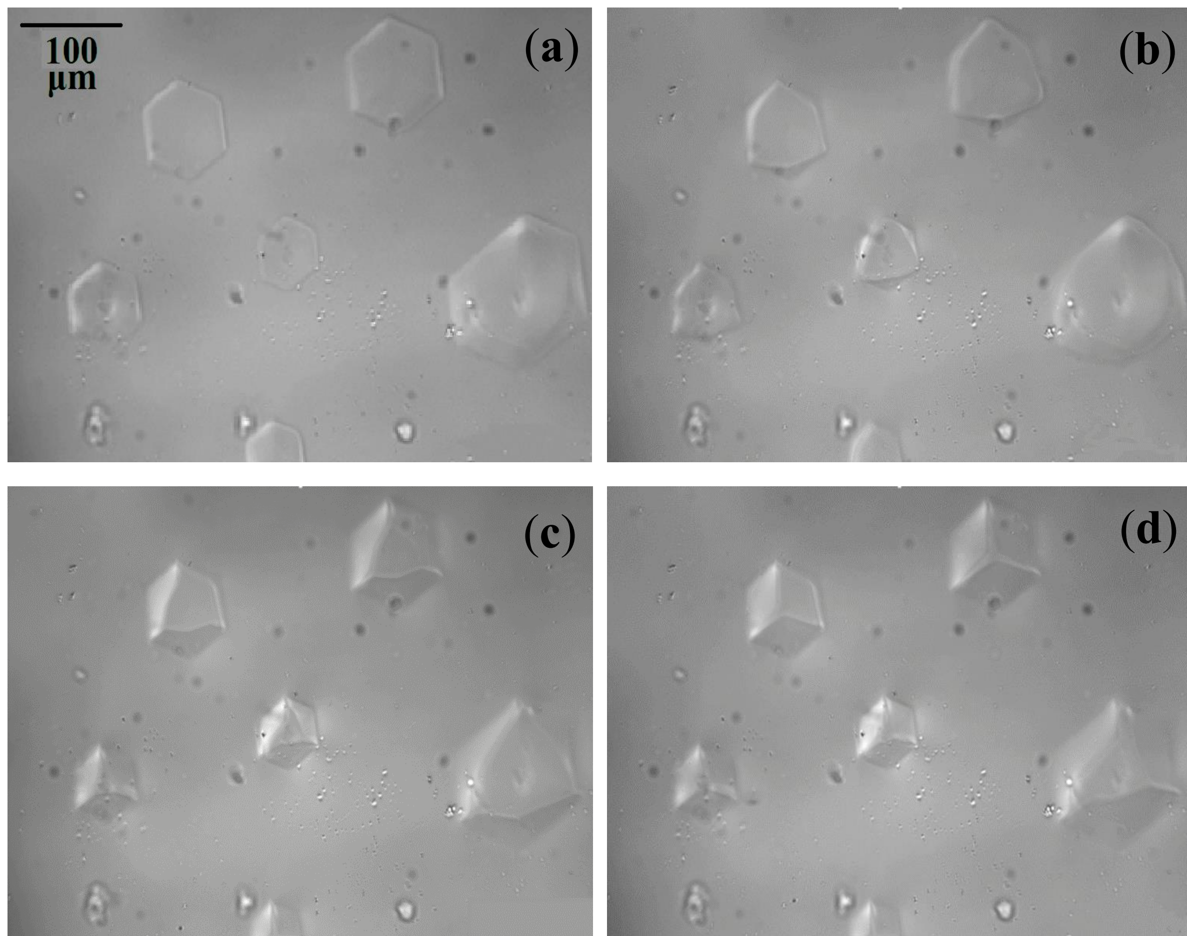

Figure 26. In-situ polarization microscopy images the of the DWC enhancement process of the sample with multiple domains in the liquid cell. Transformation of the domains can be roughly classified in three stages: the initial hexagonal domain (a) under the influence of the negative voltage turns into a triangular shape (b), and then after an intermediate stage (c) transforms into its final form of "Mercedes" star. Voltage step is 10 V, time step is 5 seconds, maximum voltage is – 200 V, and stabilization time at maximum voltage is 120 sec.

No charge transport is possible in this configuration since for the electrolyte solution the only way to do so would be an electrochemical reaction. However, such a reaction is very unlikely for the crystalline oxide with metal atoms in the highest oxidation state and will also not occur due to nanometer size of the DWs on the surface. The main point of interest here, however, is the absence of electrode grain boundaries and the existence of a more homogeneous electric field in the surface proximity due to the nature of the electrolyte solution, which provides highly mobile ions, and, hence suitable depolarization field on the surface can be formed quickly. Using the poling setup, the same DWC enhancement procedure was applied to the liquid cell; the process was observed through the polarization microscope and recorded (one picture per second). The geometrical transformation of multiple domains under the negative voltage is presented on the Fig. 26.

Primarily, it should be noted that the transformation of the domain from hexagonal shape to triangular during the DWC enhancement process occurs under a smaller absolute voltage than in the case of the metal electrode (– 200 V for liquid electrodes and approx. – 400 V for the chromium electrodes). Hence, we can make the conclusion that the metal layer on the surface of lithium niobate serves as an impedance for the DW movement. Secondly, the "triangular" shape of the DW (Fig. 26(b)) is the same that was described by Godau et al. [6] with PFM, c-AFM, and CSHG imaging for the DW with an enhanced conductivity. The results of the CSHG microscopy for the sample, 'enhanced' in the liquid cell has showed that the bulk structure of the domain indeed has an inclination (Fig. 28).

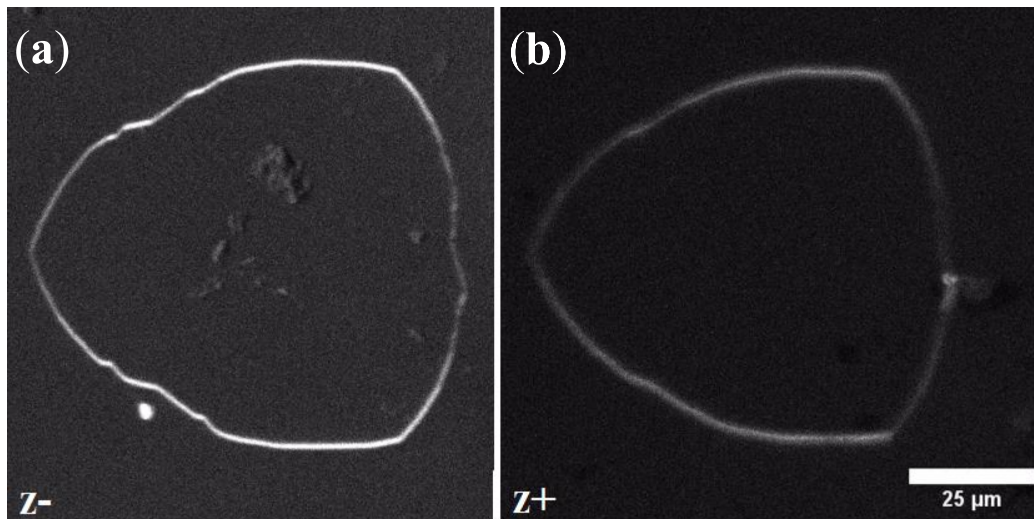

Figure 27. CSHG images of z- (a) and z+ (b) sides of the triangular domain wall in LNO (whose conductivity was enhanced with liquid electrodes). Comparison between the areas of the domains on opposite sides of images shows the presence of the inclination in the bulk structure of the wall.

The final form of the DW in the liquid cell under the influence of the negative voltage can be described as a ‘Mercedes’ star; it is stable within a range between –200 V and –600 V (the voltage, at which almost all of the domains covered with metal electrodes become ‘imploded’ – form a multitude of adjacent spike domains [8]; in case of liquid electrodes, no such state was observed under the high negative voltage). It could be suggested that the “exploded” state of the domain in the LNO crystal originates from the crystal-electrode interface, probably at the points, where the presence of metal polycrystalline boundaries creates electric fields higher than the coercive electric field of $MgO:LiNbO_3$. The 3D structure of the ‘Mercedes’ DW is presented in the Fig. 28. It is also interesting to note that such enhanced states are readily reversible and under the application of high positive voltage (~ 300 V) they return in the initial hexagonal state in the matter of seconds.

No current through the domain wall was recorded during the enhancement process, just as it was assumed earlier; current-voltage measurements with the Keithley 6517B Electrometer at three different stages of the enhanced domain with the liquid electrodes has also detected no current through the domain wall; an exemplary IV curve of the triangular stage is presented in the Fig. 29.

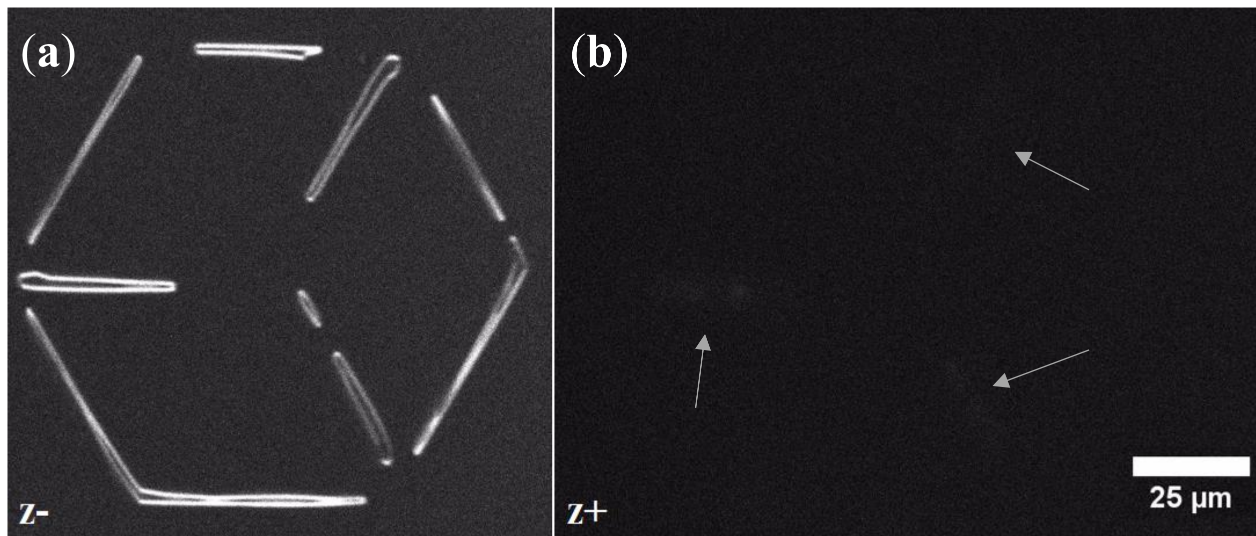

Figure 28. CSHG images of –z- (a) and +z-side (b) of the Mercedes-star-shaped domain wall in LNO (whose conductivity was enhanced with liquid electrodes). As can be seen from the images, the domain after the enhancement has turned into several domains (nine in total) with very small area, and, as can be seen in picture (b), the DWs are barely reaching the +z-side of the crystal (barely visible DW structures are marked with arrows).

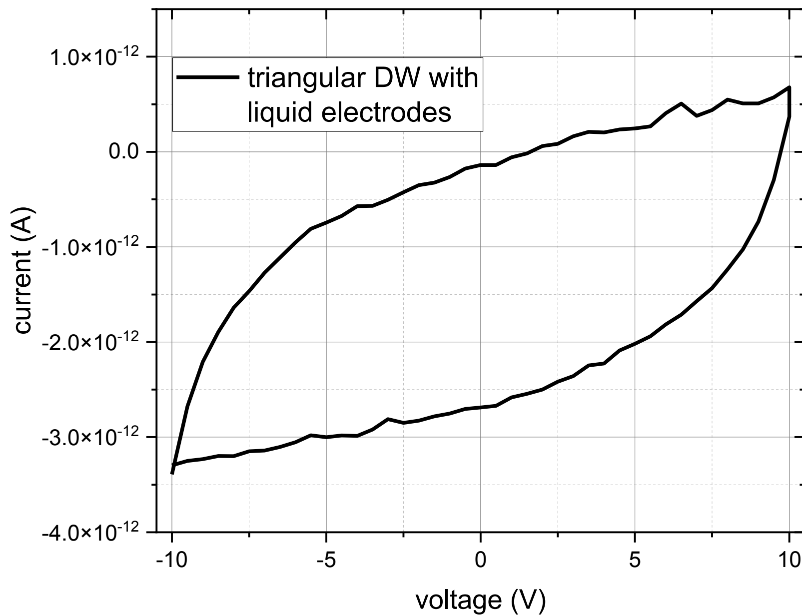

Figure 29. Current-voltage characteristics of the triangular-shaped DW in the liquid electrode. The voltage was changed step-wise with ΔU = 0. 5 V, Δt = 2 s.

Two samples, one with the triangular shaped DW and the other with 'Mercedes' star-shape were covered with chromium electrodes; the results of the DC conductivity measurements are presented for both samples in the Fig. 30 (a) and (b). The conductivity of the triangular sample enhanced with the liquid electrodes are on average even two orders of magnitude lower than the conductivity of non-enhanced samples, prepared according to the standard protocol; for the star-shaped domain it is of the same order of magnitude as for pre-enhanced "standard" samples. Taking into account the results of the CSHG imaging, for the triangular shaped domain we can assume, that the absence of the current stems from the zero inclination of the DW near the surface; from here we can assume that the presence of metal (or possibly any other material with an infinite dielectric constant, such as an electrolyte solution) electrodes stabilizes the near-surface domain walls in the inclined position. Low current of the star-shaped domain obviously stems from the fact that most of the walls just don't reach the opposite side of the sample and hence conduct improperly. Since such a novel enhancement procedure has resulted in the outcome opposed to the desired, the standard DWC enhancement procedure was additionally applied. Current-voltage characteristics of the triangular and 'Mercedes star'-shaped domains, that were enhanced for the second time with deposited metal electrodes are presented in the Fig. 30(b) and (c).

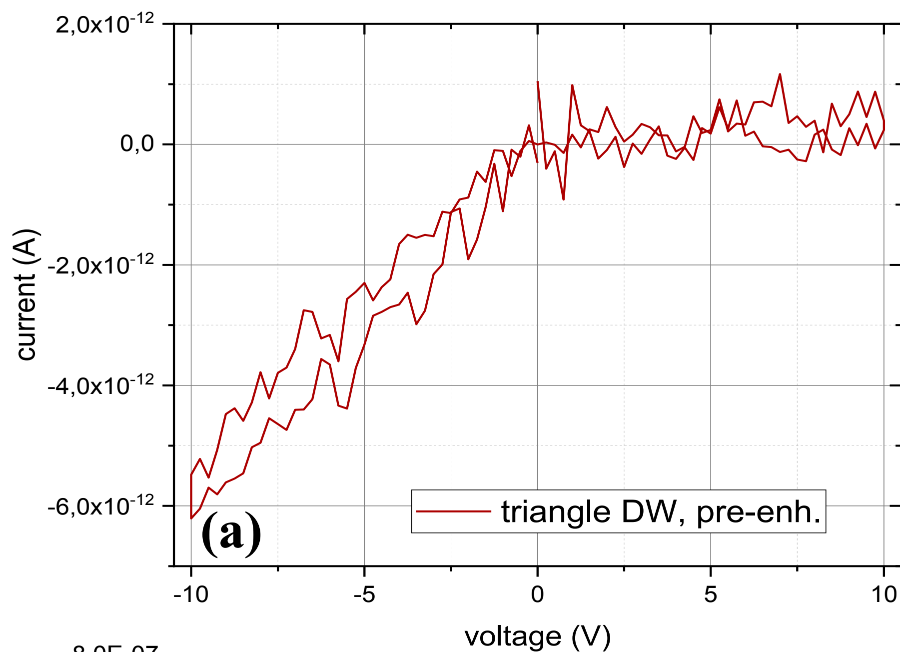

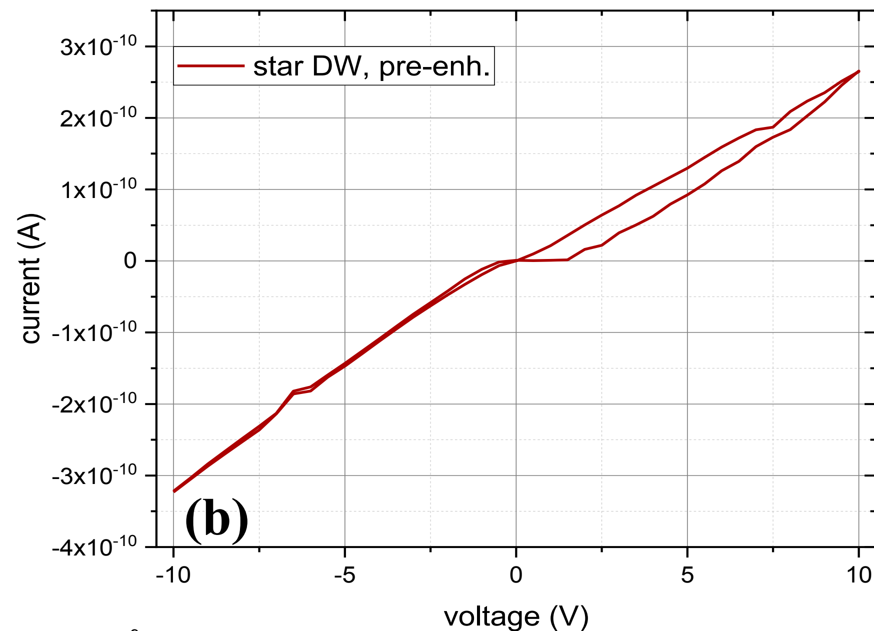

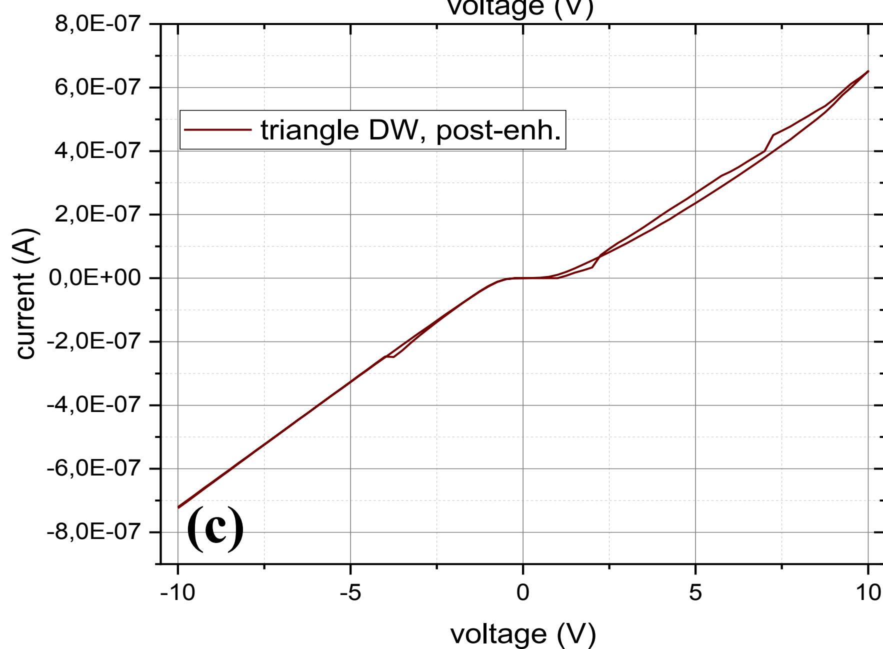

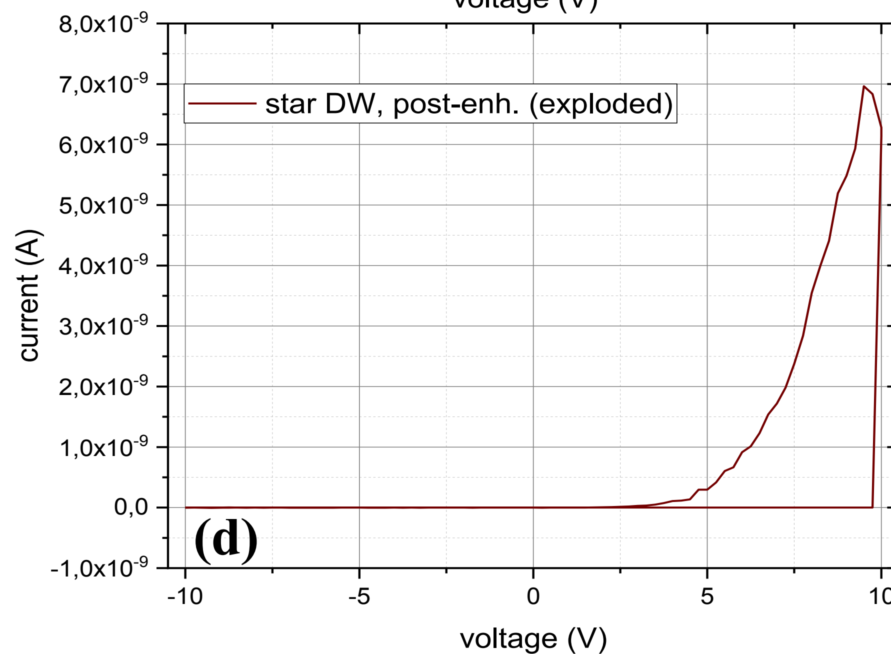

Figure 30. IV curves of the DWs enhanced with the liquid electrodes before the metal electrode deposition of triangular and star-shaped forms before the additional DWC enhancement with metal electrodes (**a** and **b** respectively,) and after the additional DWC enhancement with metal electrodes (graphs **c** and **d**). The voltage was changed step-wise with $\Delta U = 0.25$ V, $\Delta t = 5$ s.

As can be seen from the graphs, the absolute value of the current is on average ten times smaller than for the samples prepared and enhanced according to the standard protocol; after the repeated DWC enhancement, the triangular-shaped domain demonstrates the DC conductivity characteristics very similar to the standardly prepared samples. The 'Mercedes star'-shaped domain has demonstrated signs of an explosion during the enhancement process; the obtained IV curve in this case stands out due to its comparatively enormous hysteresis-like loop and major difference in the current (3.5 orders of magnitude) between the voltage points of 9.75 V and 10 V; after reaching a voltage of 10 volts, its direction was reversed. The latter case is somewhat promising for the application of LNO domains for electrical switching devices; however, due to large possibility of the DW being exploded and lack of similar samples, it is impossible to make an unequivocal conclusion; further investigations are necessary.

Concerning the influence of the electrode materials during the DWC enhancement procedure, it seems that metallic electrodes, being an impeding factor for the movement of the domain walls, also serve as the pining and stabilizing factor, which especially important for the case of an inclined DWs. The absence of the imploded state of the domain wall in the conditions where no metal polycrystalline boundary, and, as a consequence, no electric field inhomogeneity is present, coupled with the immense impact of a voltage as small as 100 V has on the near structure of the nano-sized DWs, allows us to make the assumption that the further investigation of such structures requires a different, more sophisticated way of sample preparation, meaning the achievement of atomically smooth surfaces of both LNO crystal and the metal layer. The role of the former will be investigated in the next chapter; the latter condition is somewhat harder to reach, although in the literature the description of the growth of the GaN with an ideal crystal lattice on the surface of an atomically smooth LNO is described [32].

4.4.2 Poling of the DW with a Deposited Electrode

As was previously described by Werner et al. [24], the nature of the metal-DW interface can be defined by the sequence, at which the electrode deposition and poling was done; in his work, the domain wall was poled with a calligraphic domain writing method (in a c-AFM setup). The original chromium electrode, deposited on the opposite side to the one, to which voltage was applied from the AFM, formed an ohmic contact with the poled domain wall; after removal of the original electrode and deposition of the new one, the contact acquired a diode-like characteristics. Inspired by the Werner's results, it was attempted in the course of the present work to repeat the poling process with one electrode already present on one side of the electrode. The cleaning, poling, and deposition process were conducted according to the descriptions presented in the experimental

section, but in a different order; a chromium electrode was deposited on the +z-side of the LNO crystal and since the laser in the poling setup illuminates the sample from below (–z-side), no further changes in the procedure were required. After the poling and deposition of chromium on z-side, the following IV curves (Fig. 31 (a) and (b)) were obtained:

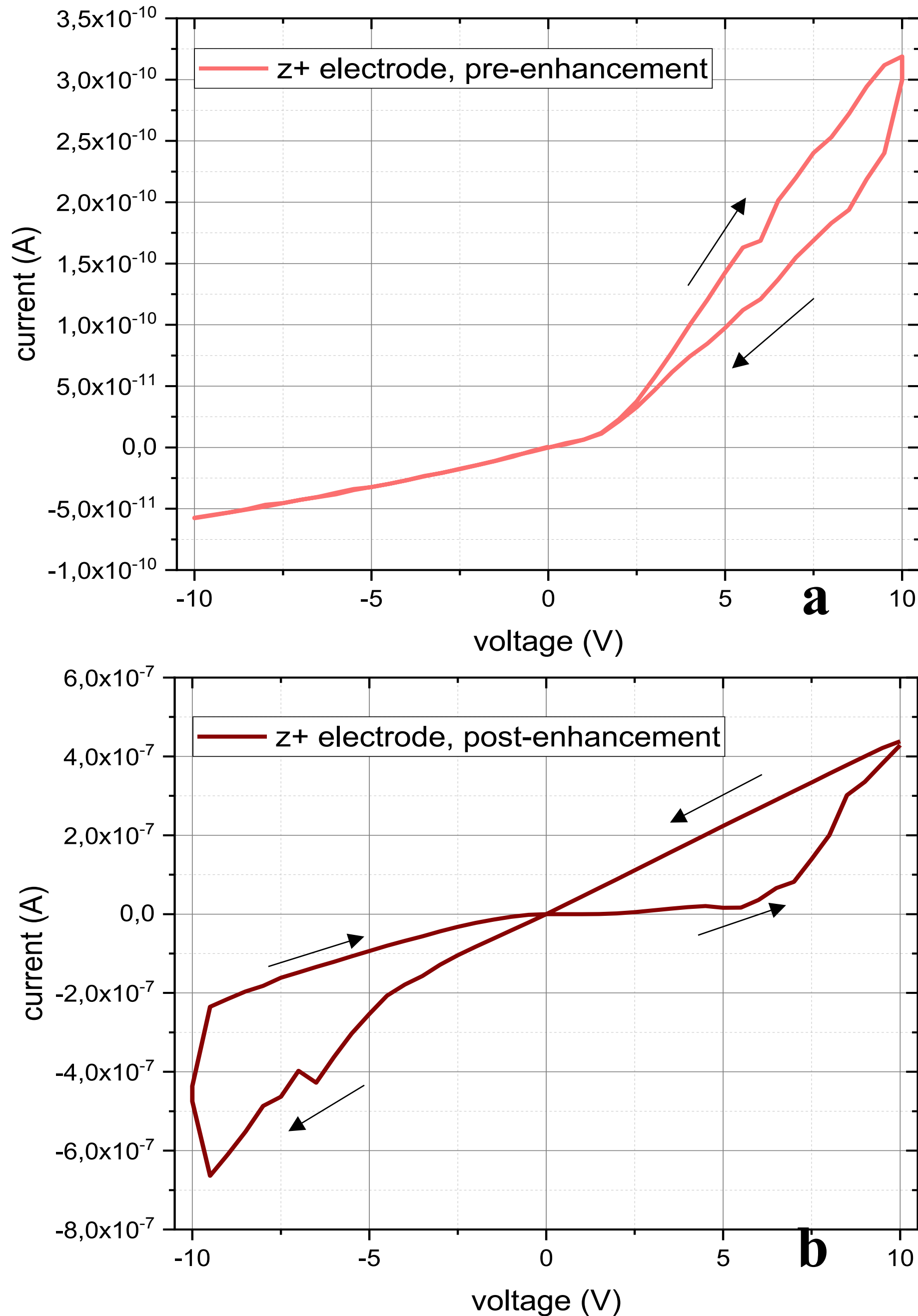

Figure 31. DC conductivity of the sample with chromium electrode deposited on the z+ side before the poling routine; a - before the DWC enhancement, b - after the DWC enhancement. The voltage was changed step-wise with ΔU = 0. 5 V, Δt = 2 s.

As can be seen from the graphs, neither before, nor after the DWC enhancement procedure, the sample showed the diode-like, rectifying behavior; characteristic values of the sample according to the equivalent circuit did not show any significant difference from all the other

samples. The presence of the hysteresis-like loops are also more pronounced, than in the case of standardly poled samples. There are two differences between the sample described by Werner, and the sample studied in this work: the first one is the thickness between the LNO crystals – 300 μm and 200 μm respectively. Such difference is unlikely to be responsible for the difference in the conductive behavior. The second difference is the source of the LNO crystal; in the case of Werner, it was supplied by HC Photonics (in this work the crystals, manufactured by Yamaju Ceramics Co., Ltd. were used). It was found by J. Ratzenberger in his Master's thesis [69], that structure and the growth process/movement of the DWs in crystals by the same producer, but acquired in one-year time intervals were different; hence, in this experiment minute differences in the chemical composition of the crystals could also play an important role. The third difference is the production procedure and it seems to be more likely explanation; the "form" of electric field differ significantly for the two cases (tip-metal electrode for calligraphic domain writing and two "plate" liquid electrodes in the case of the laser assisted poling; accordingly, the value of the poling voltage is different). The laser illumination can also play a certain role in the formation of the contact. Comparison between the Werner's experiment and the IV-curves of the standardly prepared samples before the DWC enhancement procedure (Appendix A1, Figs. A1 (a) and (b)) may suggest the fourth explanation: due to the fact, that some of the samples (samples #1 and #2 in the Fig. A1(a) and sample #3 in the Fig. A1(b)) demonstrate the behavior very close to ohmic for contacts on the both sides of the crystal, we can assume, that the formation of the potential barrier near the interface may originate from the "uneven" movement of the DW during the enhancement process. The "unevenness" of the movement stems from the different thickness of the DW near the surface and in the bulk (it is known, that for DWs of the different thickness' the threshold electrical fields is different [53]) and the contact to the surface can serve as an impeding factor for the movement of the domain wall, which can lead to the difference in the structures of the bulk and near-surface DWs. The exact formation of the DW-metal contact is not completely understood yet and the role of the various parameters is obscure; for now, the only conclusion we can make is that the method of the domain wall creation and enhancement process noticeably influences the nature of that interface. An additional problem is the degree to which poling parameters influence the structure of the DW near the interface; if it is highly sensitive to such parameters, the utilized home-built poling setup may not be able to create samples with reproducible interface characteristics due to slight fluctuations in the salt concentration or laser intensity. Obviously, all of the suggestions presented above require further investigations.

4.5 Influence of the Lithium Niobate Surface Quality on the Characteristics of the Schottky Barrier

As was established earlier, surface states on the metal-semiconductor interface can have a substantial influence on the energy structure of the barrier, up to the point where the pinning of the Fermi level occurs and, for example, the work function of both semiconductor and metal do not play a role anymore in the establishment of the effective height of the barrier, or, as it was previously discussed, the corrugations and other defects may lead to inhomogeneities in the electric field structure during poling, DWC-enhancement, and the field created by the double electric layer (spontaneous polarization and screening charges), when no external voltage is applied; all of the above have a noticeable effect on a structure of the DW and charge transport as a consequence. Furthermore, the case of lithium niobate is very tricky, due to the fact that the existence of spontaneous polarization of the crystal makes the creation of a surface close to an “ideal” one (for example a silicon surface), impossible. As was discussed in the literature review, surfaces of the commercially available mirror-polished LNO wafers are highly imperfect; an attempt to reproducibly create an atomically flat, regular surface with annealing leads to the reconstruction of the crystal lattice, accompanied by the out-sorption of the lithium and oxygen from the crystal. Such crystal reconstruction is unavoidable, since the high free energy of the surface charge, stemming from the spontaneous dipole polarization, should be compensated by formation of the depolarization field. Consequently, the presence of the vacancies on the surface is unavoidable. It is also unclear, by how much the surface quality influences wall-metal contact due to its microscopic size area.

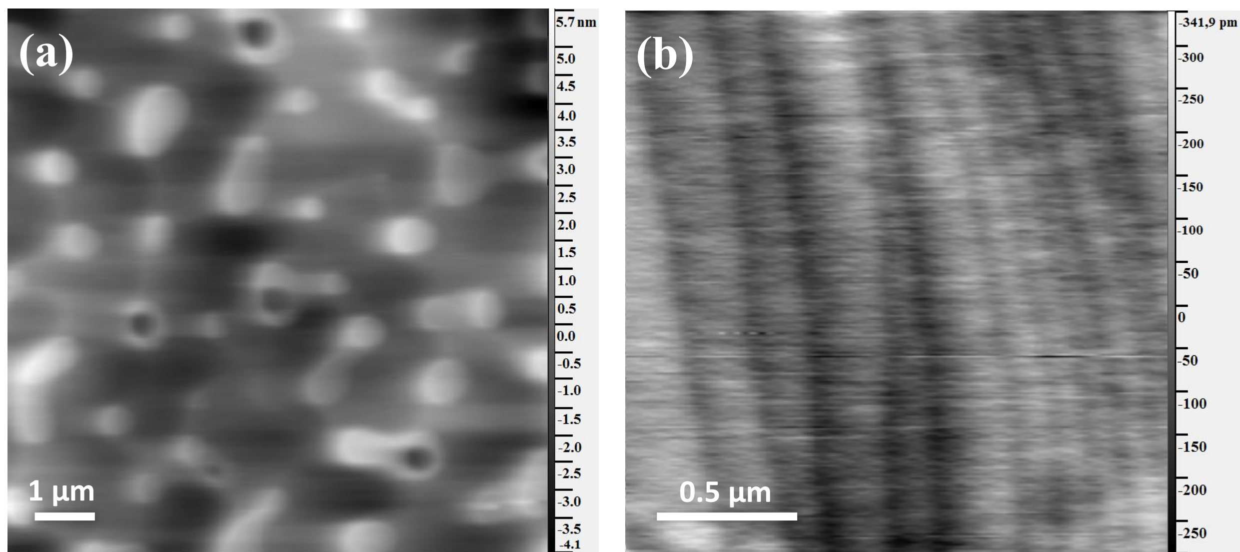

Figure 32. AFM images in air of z+ (a) and z- (b) sides of the LNO wafer after annealing at 1000 ˚C for 5 hours. On the z+ side of the wafer, an uneven surface with circular elevations can be seen, with an average distance between the lowest and highest points around 3-4 nm; the z- side clearly demonstrates a step-like surface, identical to the one obtained in the [31] with the average height of step of ~ 0.2 nm, which corresponds to the size of a unit cell in LNO.

In this section, eight samples of LNO crystals were annealed, according to the procedure suggested by Saito et al. [31]. Half of the samples were facing z+ side upwards and half of the samples were facing z- side upwards; the opposite side was partly in contact with a ceramic. After annealing, it was confirmed with AFM investigations that the desired results, at least on one side of the crystal, have been achieved. AFM-scans of both sides of an annealed sample are presented in Fig. 32; for the other samples the results were similar. Interestingly, is that only the –z-side of the LNO crystals had an atomically flat surface with a step-like structure for all the cases (Fig. 32(b)); the +z-sides of the crystals (Fig. 32(a)) showed a highly irregular structure with a great difference between highest and lowest points on the surface. Such results are somewhat contradictory to the results in the ref. [31], since there only the z+ side was employed (successfully) for the obtainment of the atomically-smooth surface. The reason for such contradictions in the results is not fully understood, but undoubtedly stems from the different physical properties of the sides with the opposite vector of spontaneous polarization; for more details see Sanna et al. [32].

After the investigation of the surface topography, the annealed samples were poled, cleaned and covered with chromium electrodes according to a standard procedure. Afterwards, the IV-curves pre-, post- and during the DWC enhancement were obtained. In Fig. 33 the current-voltage characteristics of the annealed samples are presented. In one sample it was impossible to pole the domains; hence, current-voltage characteristics of only seven annealed samples will be discussed further.

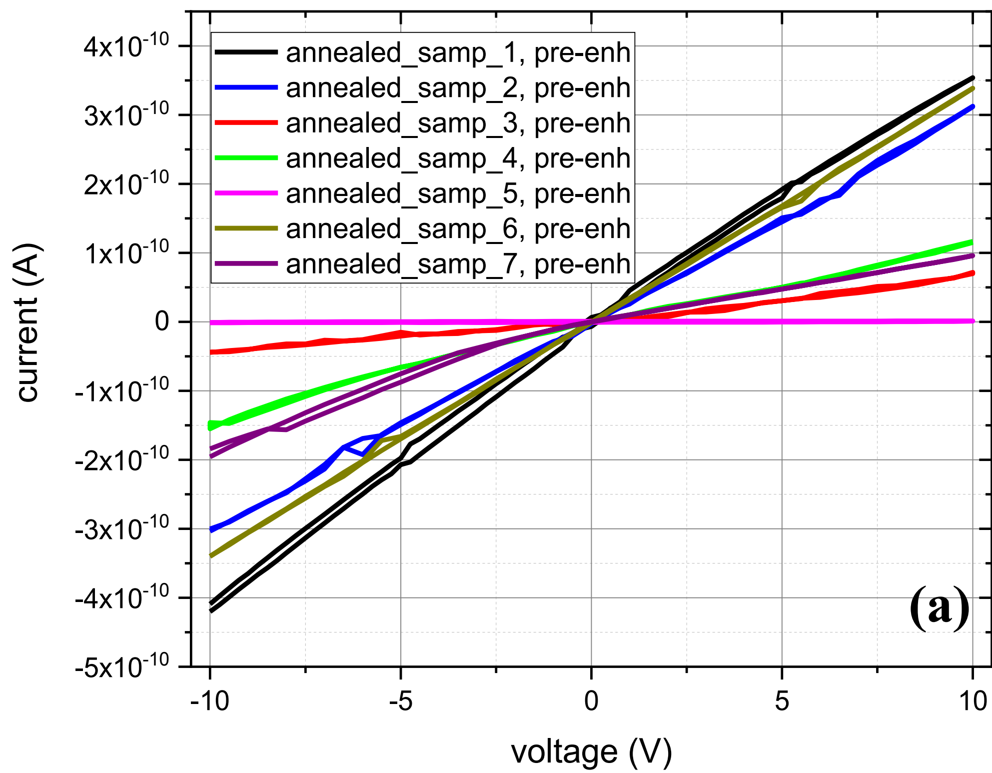

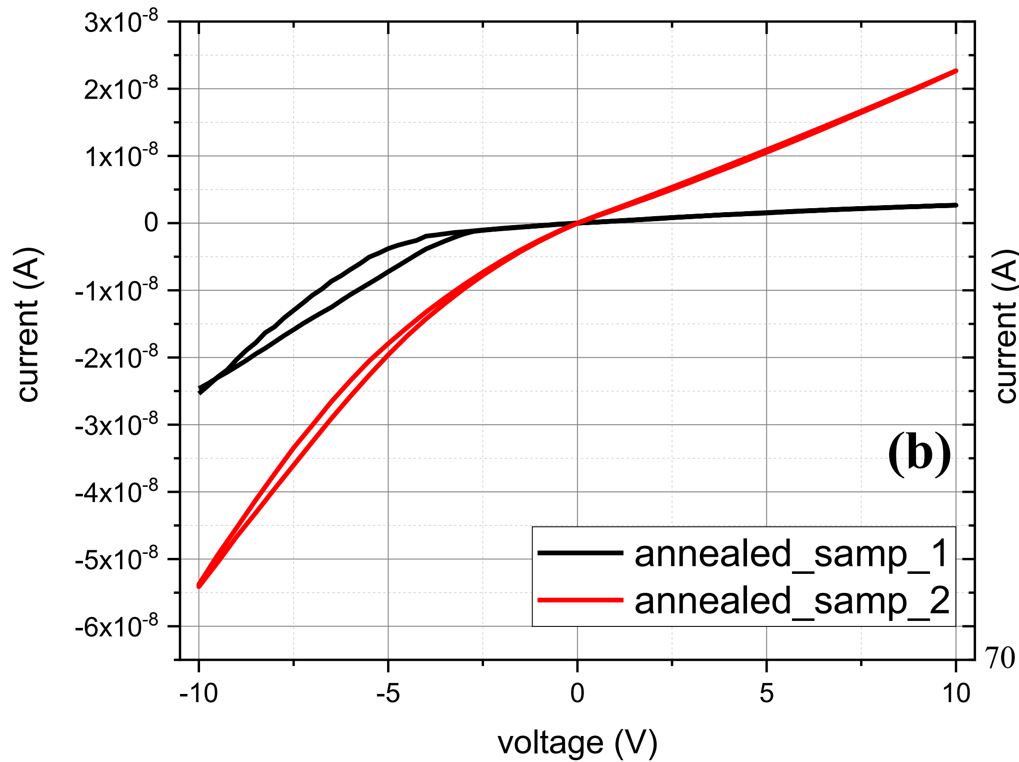

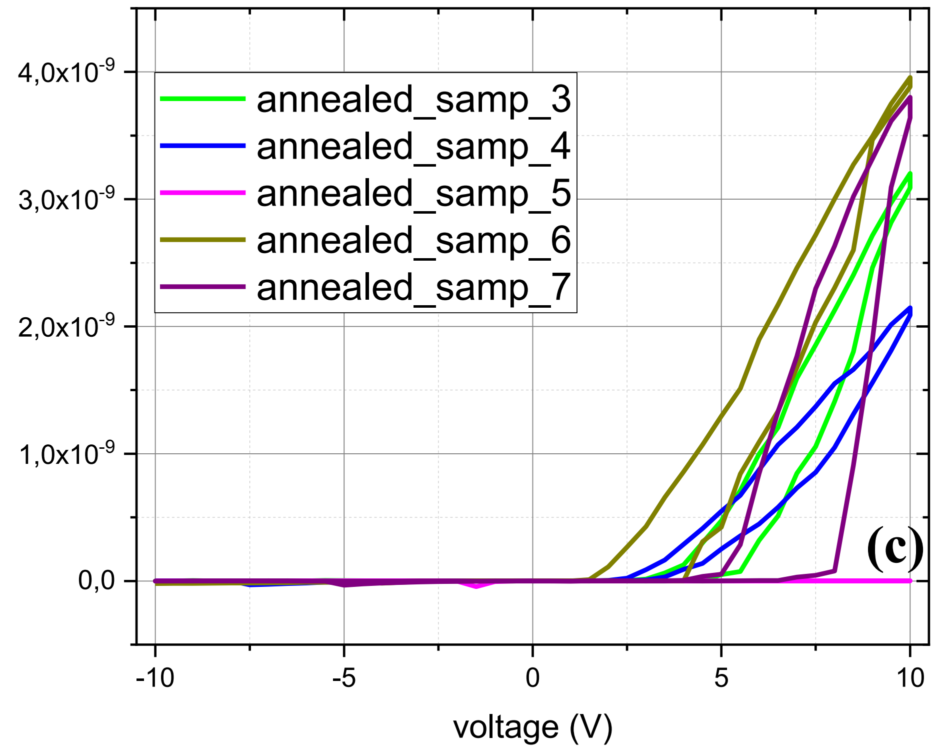

Figure 33. Current-voltage characteristics of the annealed LNO samples before DWC enhancement procedure (a) and after the DWC enhancement procedure (b and c). The latter curves were separated in two graphs for better visualization, since the absolute value of the current for annealed samples 1 and 2 was one order higher than for the rest of the samples. The annealed sample #5 after the enhancement procedure has a current around zero both before and after the enhancement. The voltage was changed step-wise with ΔU = 0.25 V, Δt = 5 s.

As can be seen from the Fig. 33(a), the IV-characteristics of the samples before the DWC enhancement procedure are very close to the those of the samples prepared according to the regular procedure (presented in the Appendix A1). We can suspect here, that the near-surface structure of the non-inclined DWs was not influenced by the transition from mirror-polished surface of poor quality to the atomically-smooth surface, formed by the annealing. The subsequent DWC enhancement procedure for the annealed samples was, however, noticeably different from the regularly prepared samples (Fig. 34).

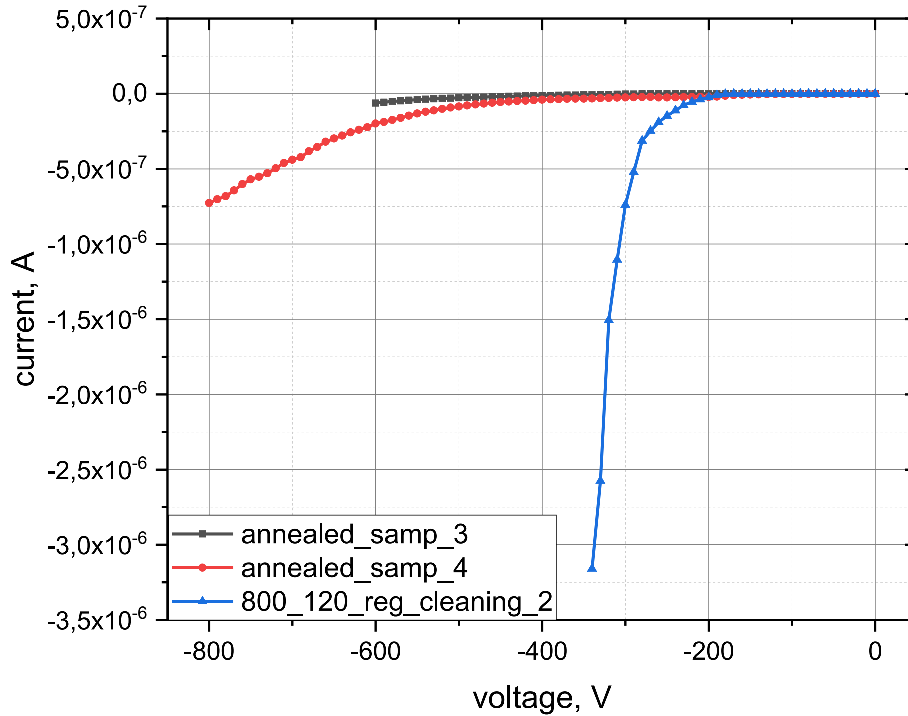

Figure 34. Enhancement curves of two annealed samples and one sample prepared according to the regular procedure. The voltage was changed step-wise with ΔU = 10 V, Δt = 5 s.

According to the description of the enhancement process, done by J. Ratzenberger in his thesis [69], the voltage ramp should be stopped as soon as the current value is close to the 10^{-5} A and for the regularly prepared samples, this current value is reached on average at the voltage of approx. – 400 V. In case of the annealed samples however, neither at – 600 V nor at – 800 V the current was close to 10^{-5} A and the IV slope has very mild decline compared to the "regular" sample. It seems that for an annealed sample it is either very hard to achieve the exploded state of the domain or even impossible. Based on these results, we can assume that either the movement of the DWs along the interface between atomically-smooth LNO and metal interface is impeded, or the inclined position of the DW cannot be properly stabilized by the "ideal" LNO surface. This

demonstrates, especially in connection with the findings for conductivity enhanced with liquid electrodes the ultimate importance of the surface conditions in the DWC process.

From the obtained IV-curves of the annealed samples after the DWC enhancement procedure, it can be seen that the majority of the samples (Fig. 33(c)) have unidirectional curves with very poor conductivity (absolute value of the current around 1 nA, only one order of magnitude larger than the current before the enhancement procedure). For one sample (annealed_samp_5) it was impossible to achieve a conductivity enhancement. It is also interesting to note that a conductive Schottky barrier was formed only on the +z-surface of poor quality; on the interface between the –z-surface and the metal electrode, no conductive barrier was formed. Here we can assume that highly irregular structure of a surface with multiple surface states promotes the formation of the Schottky barrier with a smaller barrier height, probably due to pinning of the DWs in the inclined position by crystal defects. From here we can make a conclusion, that lattice defects of mechanically polished LNO are more favorable for formation of the low potential barriers on the interface, compared to the surface with no lattice defects, but rich with oxygen vacancies. Only two samples (Fig. 33(b)) have demonstrated bi-directional IV characteristics with the conductivity two orders of magnitude larger than before the DWC enhancement procedure; such conductivity, however, is still two orders lower than that of the regularly prepared DW. It is hard to explain such a noticeable difference from the other samples; perhaps, a local damage of the surface took place during poling or cleaning process, it is, however, not unlikely.

Since the annealing process influences not only the surface structure of the lithium niobate crystal, but also the bulk lattice due to outsorption of Li and O atoms, it is also important to make an investigation of the inner structure of the domain wall in the annealed sample. On the Fig. 35 the CSHG image of the annealed_samp_3 sample is presented.

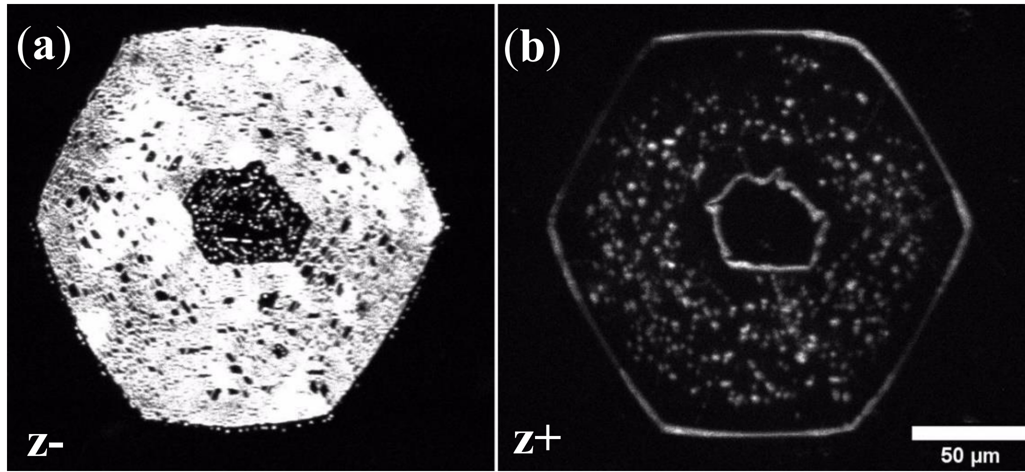

Figure 35. CSHG images of –z- (a) and +z-sides (b) of the annealed_samp_3 after the DWC enhancement procedure. The inner structure of the sample stands out due to its hexagonal form and the presence of a great multitude of spike domains on z-, majority of which do not reach the opposite side of the crystal.

The structure of the domain inside the annealed sample consists of two domains, one inside the other. A large multitude of spike domains is present on the –z-side, which is quite similar to the samples imploded during the enhancement process; the enhancement curve, however, is very uncharacteristic for an imploded standardly prepared sample, due to its low current and absence of the large change in the current during the enhancement process (several orders of magnitude). It is possible that such a large number of spike domains has been poled due to an increased number of so-called domain nuclei, as it was described by Shur [72]; such nano-sized nuclei that are impossible to be detected with standard analytical methods, are formed on the defects sites (for example V_{Li} and V_O that appear under the influence of high temperatures), or, alternatively, such nuclei are formed under the influence of high temperatures. In turn, such a high density of DWs is very hard to move/stabilize, possibly due to some kind of repulsive interaction between them, either of electrostatic or tensile nature [73].

In conclusion, the annealing process that leads to the formation of the atomically-smooth surface in LNO crystal, is also accompanied by the changes in the bulk of the crystal, which in its turn strongly influences both near-surface and bulk DW structure. Despite the presence of several interesting results (such as for example the different reactions of opposite sides of LNO on the annealing process), the conducted experiment has not had the desired effect on the contact between the DW and the metal electrode. However, being the only way of reproducible production of an atomically smooth surface in lithium niobate, further investigations should be conducted. They can include the annealing in an oxygen- and lithium-rich atmosphere, in order to avoid the desorption of the materials and the formation of vacancies in the lattice. Alternatively, for the

removal of the domain nuclei formed under high temperatures, large electric fields should be employed after the annealing for the removal of these nuclei; only after this, the poling of the DWs can be conducted.

5 Summary and Outlook

In the course of this Master's thesis work, the current-voltage characteristics between – 10 and 10 V of the domain walls in fourteen 200 μm-thick $LiNbO_3$ samples, doped with 5 mol. % of MgO prepared under different conditions (poling voltage, length of the pulse, and wafer material) was investigated; in order to increase the conductance of such a structure for up to four orders of magnitude, a large negative voltage of the order of 10^4 V/cm^{-1} was applied to the +z-side; the procedure is termed DWC-enhancement. For all of these samples the fitting procedure, according to the equivalent circuit model, consisting of two oppositely directed Schottky barriers, representing the potential barrier, formed between the DWs on +z- and –z-sides respectively, and metal electrodes, and two resistors, were performed. As a result, six parameters – saturation current I_S, characteristic voltage U_C, and resistance R in both forward and backward directions, fully characterizing the conductance properties of the samples, were obtained. In most cases, the curves were fitted with high precision. The *re-deposition* of the electrodes has led to drastic changes in the character of the current-voltage characteristics of the investigated samples (bi-directional to rectifying and vice-versa). The comparison of current-voltage characteristics obtained before and after the re-deposition leads to the following conclusions: firstly, the resistance in both directions changes; in addition to the fact, that electrode re-deposition does not change the bulk structure of the DW, we can assume that resistance in the equivalent circuit model has surface and bulk components and thus within the suggested model one resistor *could be substituted by two resistors, connected in series,* one of them is responsible for bulk resistance of DWs only and another one is related to contact between a metal electrode and the DW. Secondly, due to such drastic differences in the conductance of the samples before and after the electrode re-application, the surface processes (quality of the LNO crystal surface, metal material, deposition conditions, etc.) obviously play a significant role, perhaps even more than the poling conditions.

For the examination of the reproducibility of the LNO samples in the utilized setup, a statistically relevant set of new 15 samples were produced; five of them with a poling pulse length of 30 s and regular cleaning procedure before the electrode deposition (1st batch), five with 120 s pulse and the same regular cleaning (2nd batch), and another one with 120 s poling pulse and *oxygen-plasma cleaning* before the electrode deposition (3rd batch). The parameters, fitted for all the obtained current-voltage characteristics, have demonstrated that the value of the poling voltage and the length of the poling pulse, and hence *the size of the DW, has no noticeable influence on the conductance of the device*. The comparison between the pre-electrode deposition cleaning methods has demonstrated that cleaning of the surface in the oxygen plasma has no

advantage over the ultrasonification of the LNO crystals in organic solvents, hence it can be assumed, that carbon layer contamination on the surface of the LNO, has no noticeable influence on the formed Schottky barrier; the cleaning itself changes the near-surface domain wall structure in the way that it increases the resistance of the device and *creates rectifying contacts on the –z-side*, possibly due to changes in the surface electric field. Domain wall conductivity-enhancement procedure fully removes such a difference. It was found that in the utilized laser-assisted poling setup the production of the samples is reproducible up to a certain degree: for the majority of the samples both forward and backward resistances R are in the range of 4-6 MΩ and the average characteristic voltages U_C of backward and forward diodes are ~0.2 V and ~0.7 V respectively; consequently, the absolute value of the current at ±10 V is of the order of μA for the most of the samples. *The difference in characteristic voltages of opposite sides is probably an intrinsic property of the investigated samples, stemming from* the different dielectric properties of the LNO – z- and +z-sides (e.g., due to a large difference of ~2 eV in *ionization energy).*

In order to study the influence of the metal-DW interface contact, the electrodes of the samples from the third batch were re-deposited. The IV curves of the other samples have drastically changed both their resistor and diode parameters, and one sample has almost fully retained its original features. This result has confirmed the previously made assumption about the importance of the electrode deposition conditions (among which may be macroscopical conditions, such as humidity level, or microscopical, such as the structure of the bulk and surface near the DW; further investigations are required here) and local surface conditions in the vicinity of the domain wall. In an attempt to restore the initial conductance of samples and to investigate the influence of a mild voltages on the near-surface DW structure, up to 100 V were applied to these samples. As it was suggested, the current-voltage characteristics, and consequently the parameters of the equivalent circuit have changed. These results demonstrate the necessity of the detailed investigation and *standardization of the DWC enhancement process*, including voltage gradient and stabilization time and the further investigation of the possibility of the "fine" tuning of the near-surface DW structure *with medium voltages, starting with 2000 V/cm (~40 V for the 200 μm-thick samples, studied in this work), as suggested in the literature [53]*.

The influence of the LNO surface quality on the formation of the potential barrier on the DW-metal interface was further studied on eight virgin LNO samples that were annealed at 1000 ˚C for 5 hours; thus, an atomically-smooth surface was achieved for all of them on the – z-side; +z-side was noticeably uneven. The current-voltage characteristics of the annealed material before the DWC enhancement procedure have not demonstrated any difference from the

samples prepared according to the regular procedure. The majority of the samples after the enhancement procedure have demonstrated rectifying IV curves with the conducting Schottky barrier formed on the z+ side and very poor conductance enhancement (only one order of magnitude). *From here the conclusion was made that the poor quality LNO surface, resulting from the mechanical polishing, promotes the formation of the Schottky barrier of small height with its surface states, probably due to fixation of the DW in the inclined position by the lattice and surface defects.* The atomically-smooth z- surface with a high concentration of oxygen vacancies has the opposite effect. The enhancement procedure for such samples is also quantitatively different: here, a current of the order of 1 μA was not achieved even at -800 V, whereas for standard samples this current is usually achieved at approx. -400 V. The annealing process influences also the bulk structure of the crystal, creating multiple Li and O vacancies, from which, supposedly, a large number of spike domains appear. Possibly, as the result of repulsive interaction between these domains inside the poled DW, the movement of the latter is impeded, which is supported by the IV curve in the course of the DWC enhancement. Further experiments, that allow to separate the surface effects of annealing from the bulk effects and their influence on the charge transport in the DW-metal electrodes system, are necessary. For example, the annealing of the LNO samples in a lithium-oxygen atmosphere in order to avoid the formation of vacancies in the bulk or the intentional creation of the poor-quality surface by ion bombardment after the annealing process, should be tested. The application of large electric fields after the annealing procedure for the removal of the domain nuclei, which form at high temperatures, may also be utilized.

The domain wall was also poled with the z+ side covered with a metal electrode in advance. Unlike in the literature source, where such a domain was grown with the calligraphic domain writing method (metal tip-plate electrode system, where the DW is inclined from the start), the ohmic contact between the original electrode and DW wasn't achieved. The reason for such results can be either a form/value of the poling electric field, in which case further investigations with the use of a c-AFM setup is necessary, or from the difference in the movement of the near-surface and the bulk parts of the DW. In the latter case, the influence of the DWs movement on its near-surface structure should be investigated step-by-step, probably using an imaging technique like CSHG; the example of such investigations are thoroughly described by Kirbus at. el [7].

While the above-discussed investigations used chromium electrodes to contact the DWs, the influence of electrode material was studied in the last step. Using the liquid electrodes (water solution of NaCl) of the poling setup, an attempt was made to realize the DWC enhancement process alternatively. It has resulted in the formation of *new types of domains*, most importantly

the triangle-shaped domain (corresponding to the form of the regularly enhanced domain) and star-shaped domain. Such states were reached at much lower voltages, compared to the enhancement with the solid metal electrodes, which can serve as evidence of the *LNO-metal interface being an impeding factor for the DW movement*. The domain shapes were also *fully reversible, and consequently, the imploded state of the domain (the formation of a large number of spike domains) was not reached*. From here we can make a conclusion that such a state originates from the inhomogeneities of the electric field, caused by the metal grain boundaries, at which the field comes close to the coercive value. Coupled with the above-discovered facts that even a mild voltage of around 100 V leads to changes in the domain wall structure and that the conditions of the metal deposition process also strongly affect the current-voltage characteristics of the samples, the question arises, whether further investigation of this surface nanostructures are possible with the use of above utilized methods, or if new refinded techniques are necessary. They may include the creation of the metal-DW contact in clean room conditions and the growth of the conductive layer with the regular lattice structure on the atomically smooth surface of LNO. The inner structure of such novel domains was studied with CSHG imaging, and it was found that the bulk structure of the triangular domain wall indeed has an inclination; the poor conductance in this case can be explained by the absence of inclination near the surface, leading to the conclusion that presence of a metal contact (or contact with any other material with an infinite value of the dielectric constant, such as an electrolyte solution) is necessary for the stabilization of the inclined DW near the surface. Further, the stabilization by the metal seems preferable to the stabilization by the interface defects, since the latter leads to electric field inhomogeneities (during DWC enhancement and concerning the electric fields created by the combination of spontaneous polarization and screening charge on the LNO surface), which leads to unpredictable changes in the charge transport through the barrier; hence the above utilized atomically smooth surface should be further investigated. The star-shaped domain turned out to be an assembly of several domains with a very small area, the majority of which does not reach the opposite side, so zero conduction, in this case, is understood.

Appendix

A1. Pre-enhancement IV curves of the samples used in this work

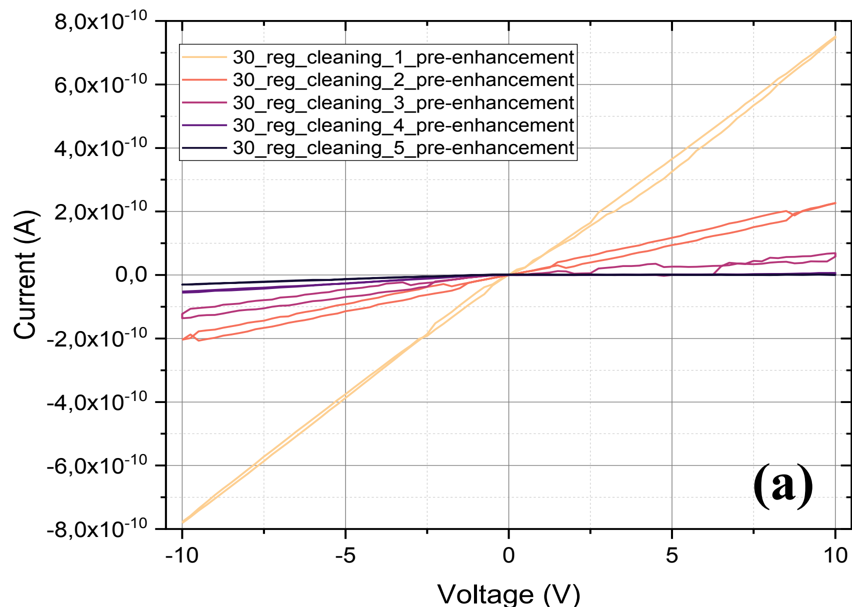

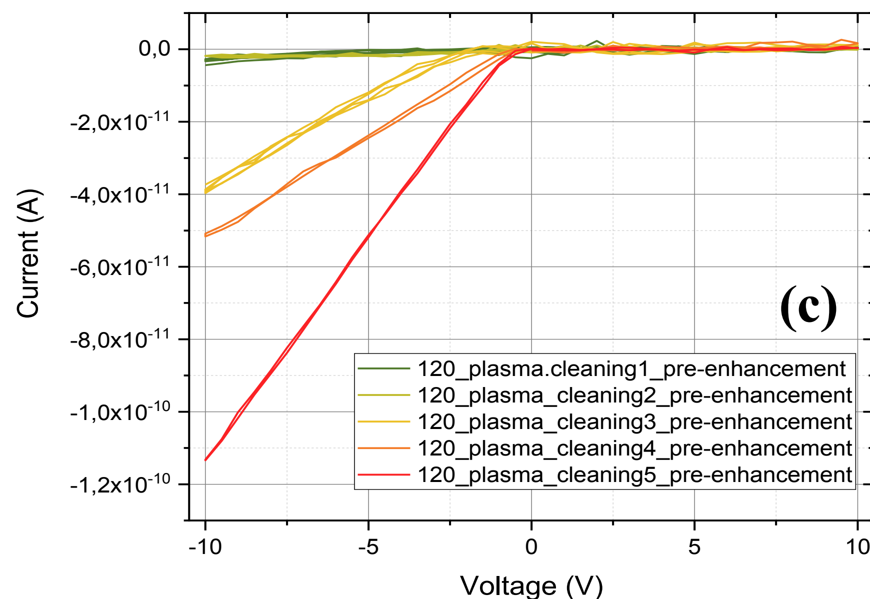

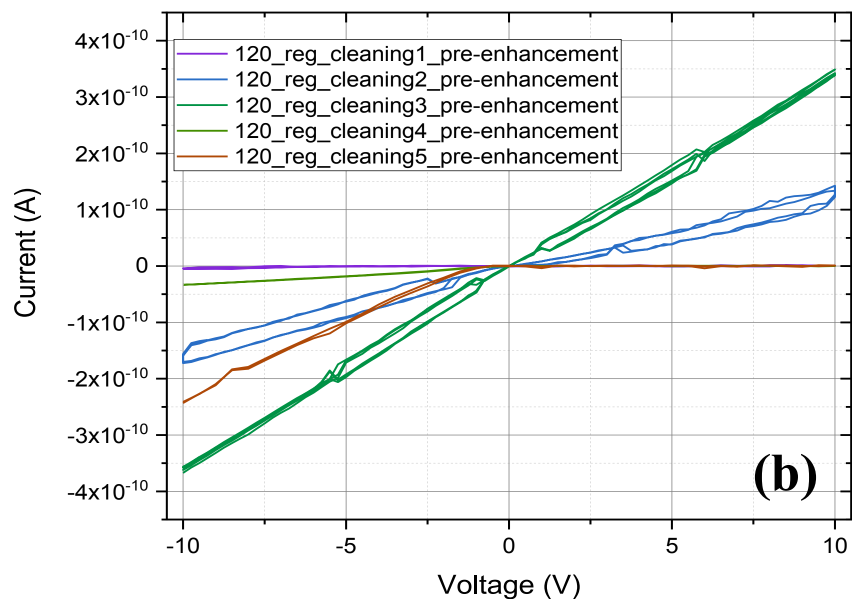

Fig. A1. IV curves of the three batches of LNO samples pre-DWC-enhancement process: (a) samples produced under the poling voltage of 800 V and 30 s pulse length and regular cleaning of the surface before the electrode deposition with DI water and organic solvents; current of the third sample was enhanced by two orders for better visualization; (b) samples produced under the poling voltage of 800 V and 120 s voltage pulse length, regularly cleaned; current of the first sample was enhanced by two orders for better visualization; (c) samples produced under the poling voltage of 800 V and 120 s voltage pulse length, with z+ and z- sides etch in the oxygen plasma for 5 minutes in addition to the regular cleaning; current of the third sample was enhanced by one orders for better visualization. The voltage was changed step-wise with ΔU = 0.25 V, Δt = 2 s.

A2. Temperature-Dependent DC Conductance

During the course of this work, temperature-dependent measurements of the DC conductance, fully analogous to those described by M. Zahn in his Master's work [15], were conducted. In order to confirm the findings of his work, the current voltage characteristics of 6 samples (jr-800-120-ow, jr-900-120-ow, jr-900-120-nw, jr-800-180-ow, jr-900-180-ow and jr-900-180-nw) were acquired for 15 temperatures, logarithmically distributed between 100 and 300 K; for each temperature an IV-curve between -10 V and 10 V with a voltage step of 0.5 V and time step of 1 s. The current-temperature I(T) dependence obtained for all the samples are in an excellent agreement with the results obtained in [15], and is presented in the Fig. A2.1 on the example of sample jr-900-120-nw. The plot is built in the Arrhenius coordinates ($\log_{10}(I) = f(1/T)$).

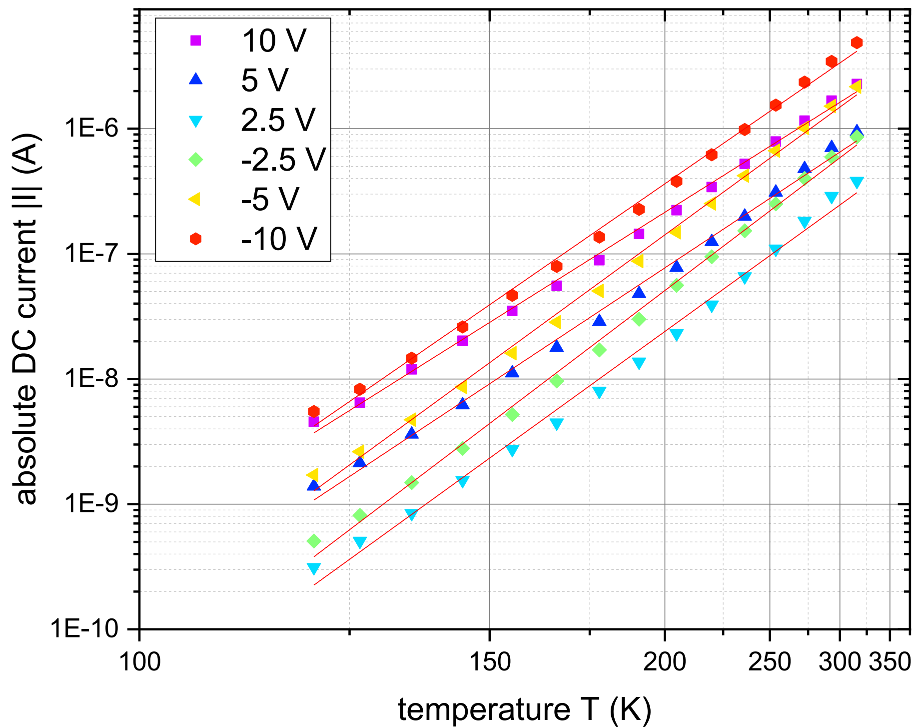

Fig. A2.1. The temperature dependence of the DC conductance for the sample **jr-900-120-nw** for six different voltage values. As can be seen from the graph, the I(T) dependence in the Arrhenius coordinates is linear, which corresponds to the temperature activated model of charge transport.

As can be seen, all dots are aligned in a line with the high precision (with the Pearson correlation coefficient of 0.998 on average). Hence, it is possible to say that transport mechanism in the LNO domain wall are indeed described by eqn. 8, which corresponds to the thermally activated transport. That means that in the room temperature electrons travel through the extended

states in the LNO conduction band, which is analogues to the intrinsic conductivity of semiconductors at the room temperature.

For all the investigated samples, for each voltage point from the I(T) graphs, dependence of the activating energy E_a on voltage was calculated and fitted, according to the eqn. A2.1, derived in [15]:

$$E_a(U) = E_0 - A\frac{U/U_c}{1-\exp(-U/U_c)} \tag{A2.1}$$

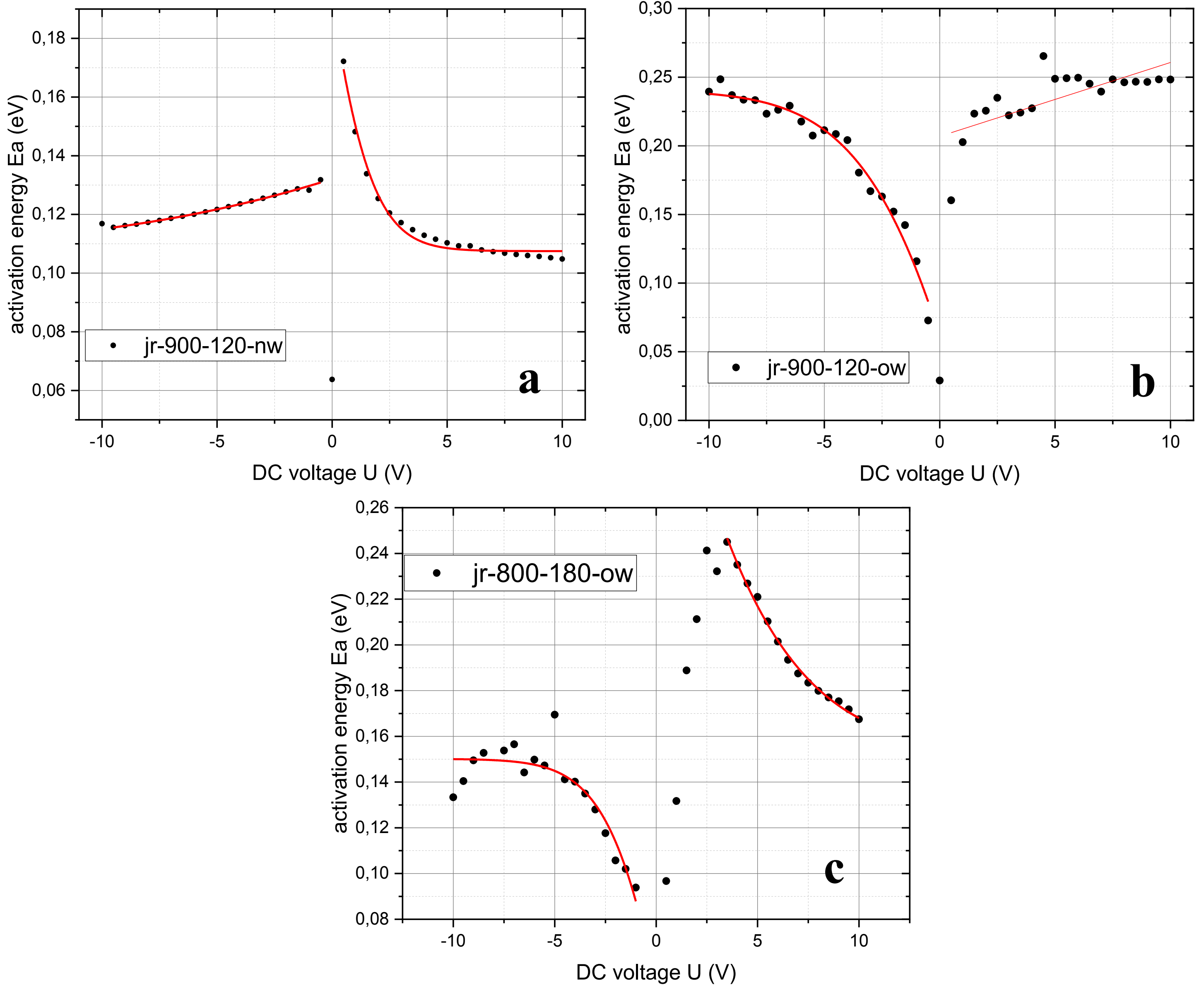

Fig. A2.2. Activation energy E_a of the domain wall samples jr-900-120-nw (a), jr-900-120-nw (b) and jr-800-180-ow (c) according to equ. B1 as a function of the dc voltage. Red lines represent the fits according to equ. A2.1.

This equation was derived on the basis of thermally activated transport equation (8), from which the following form for the activation energy is obtained:

$$E_a = -k_B \frac{\partial(lnI)}{\partial\left(\frac{1}{T}\right)}, \quad \text{(A2.3)}$$

the current *I* here is calculated according to the Shockley equation (5).

In the expression for activation energy A2.1, E_0 is a constant activation energy, connected to the intrinsic conductivity of the CDW, and A is the scaling parameter, which so far has no physical meaning. Graphical dependence of $E_a(U)$ for samples jr-900-120-ow, jr-900-120-nw and jr-800-180-ow is presented on the Fig. A2.2 (a, b, c) and fitting result for all samples are presented in the table A2.4.

Table A2.4. Fit parameters of voltage dependent activation energy Ea according to the eqn. A2.1.

sample	E_0 [meV] forward	A [meV] forward	Uc [V] forward	E_0 [meV] backward	A [meV] backward	Uc [V] backward
jr-800-120-ow	-	-	-	-	-	-
jr-900-120-ow	-	-	-	241	179	1.69
jr-900-120-nw	107	-86.2	-0.80	107	-25.0	5.06
jr-800-180-ow	152	-205	-2.50	150	100	1.12
jr-900-180-ow	-	-	-	138	-42.8	2.06
jr-900-180-nw	-	-	-	-	-	-

The results of the fitting, as seen from the graphs on the Fig. A2.2 and the Table A2.4, show that unlike in ref. [15], not all the curves agree with suggested dependence. The possible reason for that is either an insufficient amount of temperature measurements points (15 in this work versus 40 in the reference); it is also possible however that eqn. A2 is not fully correct in the description of the transport through the LNO-plate metal electrodes device. The other major difference is that in Zahn's work all the measured samples had a positive peak of $E_a(U)$ dependence around 0 V (like for the sample jr-900-120-nw in the Fig. A2.2(a)); here, the sample jr-900-120-ow has a fully negative peak and the $E_a(U)$ dependence around 0 V for the sample jr-800-180-ow resembles such dependence for the industrial BAT 48 Schottky diode, investigated in the same work [15]. The reason for such a major difference is not yet clear.

The behavior of the $E_a(U)$ curves for the larger voltages confirms the earlier findings; for the researched samples the activation energy approximates to a constant value E_0, which is a numerical characteristics of the intrinsic conductive properties of the DWs. For most of the samples E_0 is in the range between 150 mV and 250 mV, although for the sample jr-900-120-nw this value is equal to 107 mV. According to the temperature activated transport model (eqn. (8)), this value is approximately equal to the energy gap between the Fermi level inside the DW and the mobility edge level in the conduction band. Possibly, this value can be decreased by increasing the DW inclination angle α (according to eqn. 1).

A3. Higher-Harmonic Current Generation in Domain Wall Structures

For all "jr" samples AC response measurements were conducted (amplitude U_1 and offset U_0 sweeps at fixed frequency, as it was described in the section 3.6). For the offset sweep from -10 to 10 V, the combination of transimpedance and voltage amplitude U_1 was chosen in the way to establish the registered voltage signal sufficiently large (tens of mV at least) for good signal-to-noise ratio (usually U_1 was of the order of hundreds of mV) and avoid overload of circuit elements. For the selection of the offset voltage U_0 for the amplitude sweep in previously obtained offset sweep a value was chosen, at which the current-voltage characteristic exhibits most non-linear (exponential) behavior. Since the setup used in this work is exactly the same that was used in M. Zahn's master thesis [15], its limitations are the same. This means that the relative (current amplitude three orders below the first harmonic) and absolute (~ 10^{-10} A) noise limits are valid, and for most of the samples in this work only three higher harmonics of the current were distinguishable. All the samples demonstrate qualitative correspondence with the model (Fig. 23 and eqns. (13) and (14)) suggested by M. Zahn, but not quantitative, due to the nature of the investigated samples – ohmic samples barely demonstrate diode-like features, which makes measurements and fitting not very reliable; for diode-like samples half of the parameters (e.g. R_f, $U_{c,f}$ and $I_{s,f}$) cannot be fitted unequivocally. The phase angle dependence on the amplitude is in good accordance with the model of anti-clockwise behavior; phase-angle dependence on offset voltage demonstrates qualitative agreement with results obtained in [15].

In order to measure the degree of "non-linearity" of the system, containing LNO DWs and metal electrodes, the frequency comb can be investigated. That idea was demonstrated in its most simple form by Gambhir et al. [74], with a diode as the example of a non-linear circuit element. According to the Shockley equation (eqn. 4), the current in diodes has an exponential dependence on voltage, which can be also represented by an infinite power series. If we have an AC voltage $U = U_0 + U_1\cos(\omega_0 t)$ with the use of trigonometrical formulas, first three members of infinite series of output current of a diode have the following form:

$$I_{output} = R_F \begin{bmatrix} \left(\frac{I_S}{U_C} + \frac{I_S}{U_C^2} + \frac{I_S}{2U_C^3} U_C^2 + \frac{U_1^2}{4}\right) U_1 cos\omega_0 t \\ + \frac{1}{4}\left(\frac{I_S}{U_C^2} + \frac{I_S}{U_C^3} U_0\right) U_1^2 cos2\omega_0 t \\ + \frac{I_S}{24U_C^3} U_1^3 cos3\omega_0 t + \cdots \end{bmatrix}, \tag{A3}$$

where R_F – transimpedance of the current-to-voltage converter. This equation was used in derivation of eqns. (13) and (14) and it allows simple demonstration of higher harmonic current contributions (HHCC) and their amplitudes, especially their dependence on the voltage amplitude, which should demonstrate direct proportionality.

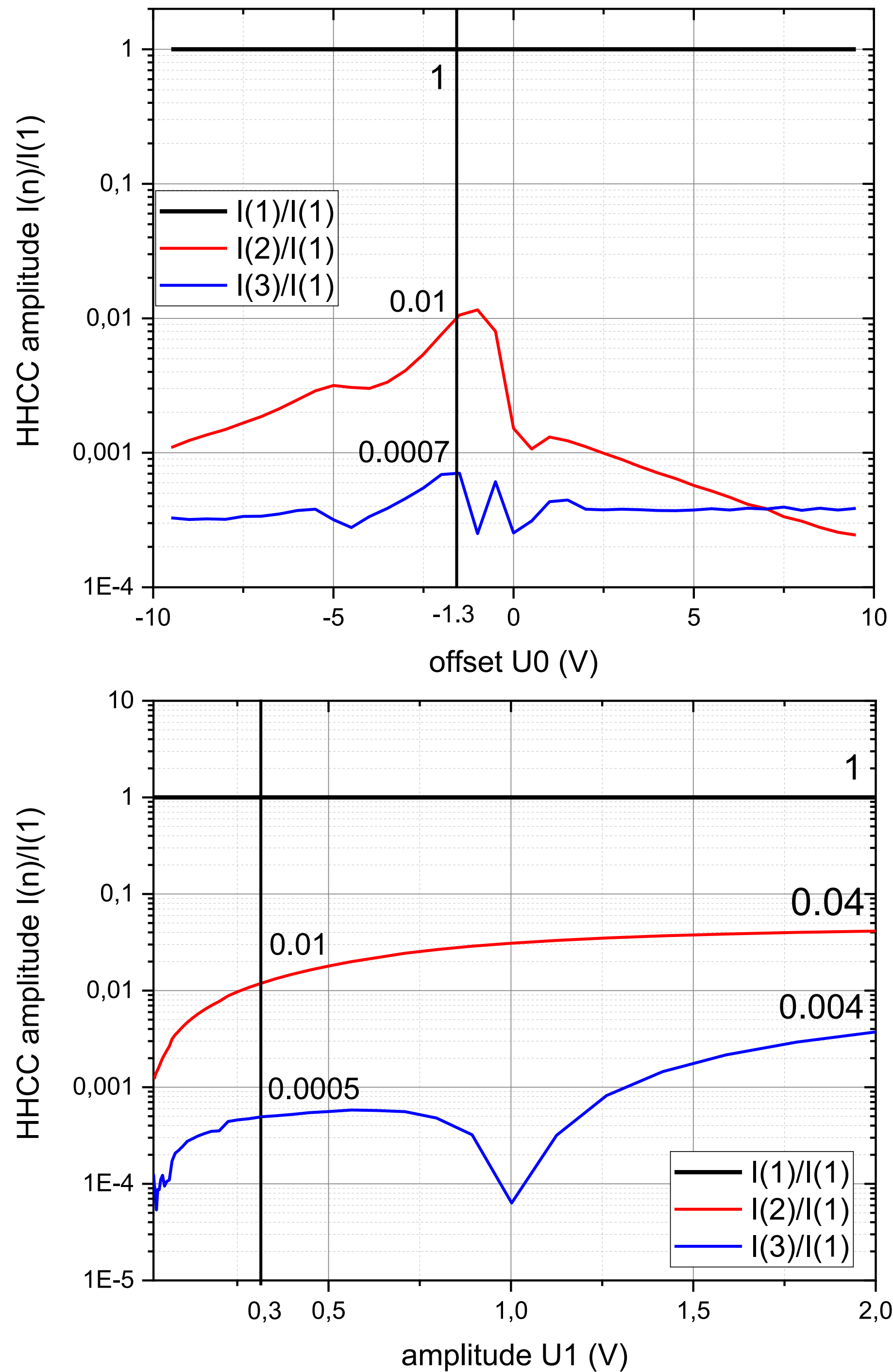

Figure A3.1. Ratio of HHCCs to the current amplitude of the fundamental harmonic vs. offset and amplitude voltage for the sample **jr-800-60-ow**. Offset sweep was recorded for amplitude U_1 = 300 mV; amplitude sweep was recorded at U_0 = -1.3 V. Ratio of HHCC to current amplitude with fundamental frequency is shown with black vertical lines for maximum amplitude U_1 = 2 V, and for values of U_0 and U_1, for which amplitude or offset sweep was recorded, correspondingly.

Using the sample jr-800-60-ow we can study the HHCC compared to the current amplitude of the fundamental harmonic with frequency ω_0 (normalized HHCC) and its dependence on offset U_0 and amplitude U_1 (Fig. A3.1). The graphs were obtained from the offset and amplitude sweeps measurements by normalization of the data.

As can be seen from the graphs, dependence of the HHCC on the offset voltage has a complex form; largest occurrence of higher harmonics can be observed for offset voltages near zero; under the increase of offset voltage U_0 currents with frequency $2\omega_0$ and $3\omega_0$ steadily decline. Such results are expected, since the influence of diodes (i.e., non-linear elements) in analogous circuits is strongly manifested at lower offset voltages. As can be seen, the HHCC is minor; even second harmonic contribution I_2 close to maximum is only one percent of fundamental frequency current I_1.

The dependence of the HHCC compared to the first harmonic on frequency U_1 is in complete accordance with results of a diode [74] – the higher the amplitude, the larger the input of HHCC. For the largest measured amplitude U_1 = 2 V, the contribution of the second harmonic is four percent of the current with the fundamental frequency. The local minimum at U_1 = 1 V can be addressed to the parasitic influence of the series resistance. All in all, the sample jr-800-60-ow can be characterized as demonstrating linear behavior, HHCC is negligible. Since for offset voltages, where the sample demonstrates predominantly non-linear behavior (and at which amplitude sweeps of HHCCs is measured) and high voltage amplitudes noise-to-signal ratio is the largest, ratio of HHCC to the current of the first harmonics will be measured for highest U_1 for all samples. The dependence of the HHCC amplitude compared to the fundamental one is presented for samples *jr-800-180-ow* and *jr-900-20-nw* below (Figs. A3.2-A3.3); it can be seen that the input of the higher harmonics can vary between one and thirty percent, proportional to the value of the characteristic voltage. For all the samples, qualitatively, these graphs look very similar to each other, and the height of the peaks and their position is defined completely by the saturation current I_S and characteristic voltage U_C, and are adequately predicted by the M. Zahn's equivalent circuit model. Since in the course of this work it was found out that the DW-metal interface changes very drastically from one sample to another (prepared seemingly in the same conditions), and, consequently, I_S and U_C in both directions change quite drastically as well, no useful quantitative information can be extracted from these graphs. It was observed, that for DWs showing the most pronounced diode-like IV-characteristics, a detection of the fourth harmonic for high amplitudes is possible, but its contribution does not surpass few percent of the first harmonic current. The value of the second harmonic can be equal to fifty percent of the current with fundamental frequency;

the ratio of HHCC to the current with fundamental frequency is proportional to the amplitude U_1 and shows asymptotic growth, unlike with the case of the simple diode [12], where amplitude growth does not show any limit and detection of the twentieth harmonic is possible. The presence of the large resistance, connected in series to the diode is probably the reason for that. In principle, that kind of AC measurements can be used in the future as the way to quantitatively determine the presence of the non-linearity in the IV-characteristics of a sample. Considering the fact, that one of the possible application the LNO domain walls us the formation of conductive nano-paths between the elements of an integrated circuit, the ability to detect even smallest potential barrier in the interface (and then to get rid of it), and, consequently, the applications of such graphs, are quite useful.

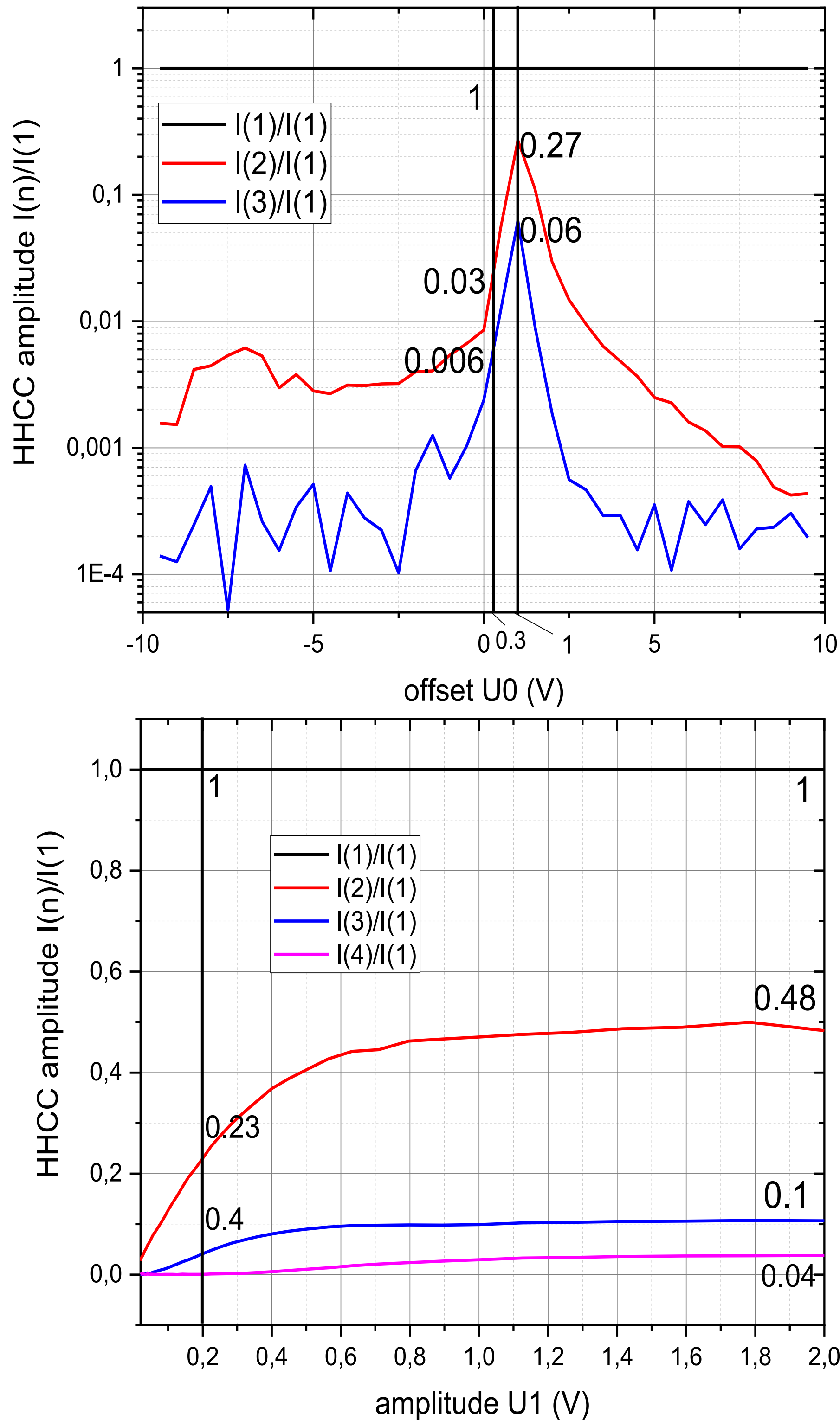

Figure A3.2. Ratio of HHCCs to the current amplitude of the fundamental harmonic vs. offset and amplitude voltage for the sample **jr-800-180-ow**. Offset sweep was recorded for amplitude U_1 = 200 mV; amplitude sweep was recorded at U_0 = 0.3 V. Ratio of HHCC to current is shown with black vertical lines for maximum amplitude U_1 = 2 V, and for values of U_0 and U_1, for which amplitude or offset sweep was recorded, correspondingly, and for U_0 = 1 V, since it demonstrates the maximum.

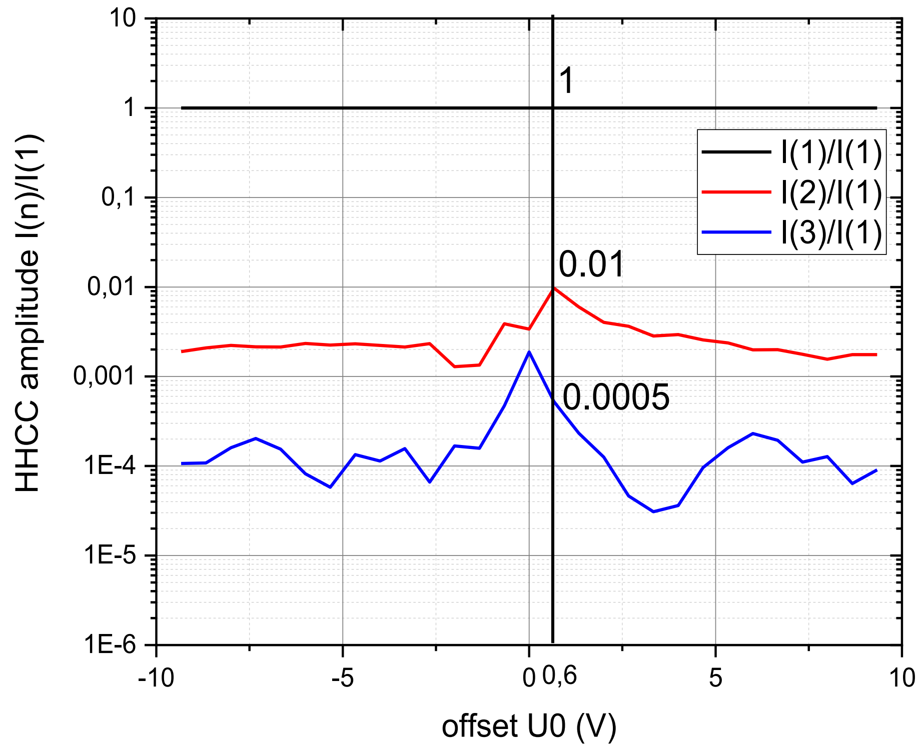

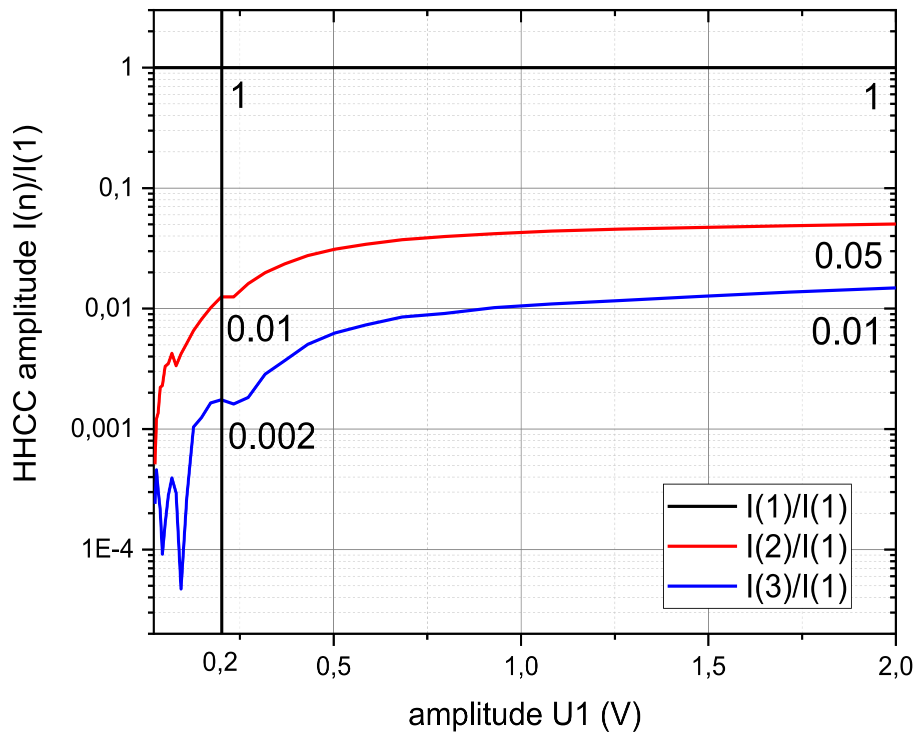

Figure A3.3. Ratio of HHCCs to the current amplitude of the fundamental harmonic vs. offset and amplitude voltage for the sample **jr-900-20-nw**. Offset sweep was recorded for the amplitude U_1 = 200 mV; the amplitude sweep was recorded at U_0 = 0.6 V. Ratio of HHCC to current is shown with black vertical lines according to the same principle.

References

[1] Schultheiß, J., Rojac, T., & Meier, D. (2022). Unveiling Alternating Current Electronic Properties at Ferroelectric Domain Walls. *Advanced Electronic Materials*, *8*(6), 2100996. https://doi.org/10.1002/aelm.202100996

[2] Holstein, W. L. (1997). Etching study of ferroelectric microdomains in $LiNbO_3$ and $MgO:LiNbO_3$. *Journal of Crystal Growth*, *171*(3–4), 477–484. https://doi.org/10.1016/S0022-0248(96)00681-1

[3] Allwood, D. A. & Cowburn, R. (2010). "Magnetic domain-wall logic." *Science* 309.5741, 1688–1692. https://doi.org/10.1002/9783527628155.nanotech039

[4] Chaib, H., Otto, T., & Eng, L. M. (2002). Theoretical study of ferroelectric and optical properties in the 180° ferroelectric domain wall of tetragonal $BaTiO_3$. *Physica Status Solidi (B) Basic Research*, *233*(2), 250–262. https://doi.org/10.1002/1521-3951(200209)233:2<250::AIDPSSB250>3.0.CO;2-1

[5] Beccard, H., Kirbus, B., Beyreuther, E., Rüsing, M., Bednyakov, P., Hlinka, J., & Eng, L. M. (2022). Nanoscale Conductive Sheets in Ferroelectric $BaTiO_3$: Large Hall Electron Mobilities at Head-to-Head Domain Walls. *ACS Applied Nano Materials*, *5*(7), 8717–8722. https://doi.org/10.1021/acsanm.2c01919

[6] Godau, C., Kämpfe, T., Thiessen, A., Eng, L. M., & Haußmann, A. (2017). Enhancing the Domain Wall Conductivity in Lithium Niobate Single Crystals. *ACS Nano*, *11*(5), 4816–4824. https://doi.org/10.1021/acsnano.7b01199

[7] Kirbus, B., Godau, C., Wehmeier, L., Beccard, H., Beyreuther, E., Haußmann, A., & Eng, L. M. (2019). Real-Time 3D Imaging of Nanoscale Ferroelectric Domain Wall Dynamics in Lithium Niobate Single Crystals under Electric Stimuli: Implications for Domain-Wall-Based Nanoelectronic Devices. *ACS Applied Nano Materials*, *2*(9), 5787–5794. https://doi.org/10.1021/acsanm.9b01240

[8] Nassau, K., Levinstein, H. J., & Loiacono, G. M. (1966). Ferroelectric lithium niobate. 1. Growth, domain structure, dislocations and etching. *Journal of Physics and Chemistry of Solids*, *27*(6–7), 983–988. https://doi.org/10.1016/0022-3697(66)90070-9

[9] Jun, D., Wei, J., Png, C. E., Guangyuan, S., Son, J., Yang, H., & Danner, A. J. (2012). Deep anisotropic $LiNbO_3$ etching with SF_6/Ar inductively coupled plasmas. *Journal of Vacuum Science and Technology B:Nanotechnology and Microelectronics*, *30*(1), 011208. https://doi.org/10.1116/1.3674282

[10] Wang, M., & Yao, J. (2013). Multitap microwave photonic filter with negative coefficients based on the inherent birefringence in a $LiNbO_3$ phase modulator. *IEEE Photonics Journal*, *5*(3), 5500709. https://doi.org/10.1109/JPHOT.2013.2265981

[11] Chen, Y., Chen, X., Zeng, X., Wu, F., Chen, L., Wang, Y., Xie, S., Xia, Y., & Chen, Y. (2000). First-order quasi-phase-matched second harmonic generation in bulk periodically poled $LiNbO_3$. *Proceedings of SPIE - The International Society for Optical Engineering*, *4223*, 65–68. https://doi.org/10.1117/12.401754

[12] Kämpfe, T., Wang, B., Haußmann, A., Chen, L.-Q., & Eng, L. M. (2020). Tunable non-volatile memory by conductive ferroelectric domain walls in lithium niobate thin films. *Crystals*, *10*(9), 1–11. https://doi.org/10.3390/cryst10090804

[13] Wolba, B., Seidel, J., Cazorla, C., Godau, C., Haußmann, A., & Eng, L. M. (2018). Resistor Network Modeling of Conductive Domain Walls in Lithium Niobate. *Advanced Electronic Materials*, *4*(1), 1700242. https://doi.org/10.1002/aelm.201700242

[14] Schröder, M., Haußmann, A., Thiessen, A., Soergel, E., Woike, T., & Eng, L. M. (2012). Conducting domain walls in lithium niobate single crystals. *Advanced Functional Materials*, *22*(18), 3936–3944. https://doi.org/10.1002/adfm.201201174

[15] Zahn M. P. (2022). "Nonlinear electronic conductivity in lithium niobate domain walls", Master's Thesis, Technische Universität Dresden, Dresden.

[16] Lu, H., Tan, Y., McConville, J. P. V., Ahmadi, Z., Wang, B., Conroy, M., Moore, K., Bangert, U., Shield, J. E., Chen, L.-Q., Gregg, J. M., & Gruverman, A. (2019). Electrical Tunability of Domain Wall Conductivity in $LiNbO_3$ Thin Films. *Advanced Materials*, *31*(48), 1902890. https://doi.org/10.1002/adma.201902890

[17] Weis, R. S., & Gaylord, T. K. (1985). Lithium niobate: Summary of physical properties and crystal structure. *Applied Physics A Solids and Surfaces*, *37*(4), 191–203. https://doi.org/10.1007/BF00614817

[18] Abrahams, S. C., Reddy, J. M., & Bernstein, J. L. (1966). Ferroelectric lithium niobate. 3. Single crystal X-ray diffraction study at 24 °C. *Journal of Physics and Chemistry of Solids*, *27*(6–7), 997–1012. https://doi.org/10.1016/0022-3697(66)90072-2

[19] Haußmann, A. (2006) "UV-unterstützte Erzeugung ferroelektrischer Domänenmuster in Lithiumniobat zur selektiven Abscheidung von Adsorbaten", Diploma Thesis, Technische Universität Dresden, Dresden.

[20] Halliburton, L.E. (1989). "Properties of lithium niobate", EMIS Data Review Series. London INSPEC Institution of Electrical Engineers.

[21] Shur, V. Ya. (2013). Domain nanotechnology in ferroelectric single crystals: Lithium niobate and lithium tantalate family. *Ferroelectrics*, *443*(1), 71–82. https://doi.org/10.1080/10584587.2013.794638.

[22] Sones, C. L., Mailis, S., Brocklesby, W. S., Eason, R. W., & Owen, J. R. (2002). Differential etch rates in z-cut $LiNbO_3$ for variable HF/HNO3 concentrations. *Journal of Materials Chemistry*, *12*(2), 295–298. https://doi.org/10.1039/b106279b

[23] Haußmann, A. (2018). "Geometry-controlled ferroelectric domain-wall conductivity in $LiNbO_3$ single crystals", Ph. D. Thesis, Technische Universität Dresden, Dresden.

[24] Werner, C. S., Herr, S. J., Buse, K., Sturman, B., Soergel, E., Razzaghi, C., & Breunig, I. (2017). Large and accessible conductivity of charged domain walls in lithium niobate. *Scientific Reports*, *7*(1), 9862. https://doi.org/10.1038/s41598-017-09703-2

[25] Schröder, M., Chen, X., Haußmann, A., Thiessen, A., Poppe, J., Bonnell, D. A., & Eng, L. M. (2014). Nanoscale and macroscopic electrical ac transport along conductive domain walls in lithium niobate single crystals. *Materials Research Express*, *1*(3), 035012. https://doi.org/10.1088/2053-1591/1/3/035012

[26] Zhang, W., Wang, C., Lian, J.-W., Jiang, J., & Jiang, A.-Q. (2021). Erasable Ferroelectric Domain Wall Diodes. *Chinese Physics Letters*, *38*(1), 017701. https://doi.org/10.1088/0256-307X/38/1/017701

[27] Rhoderick E. H. & Williams R. H. (1988). Metal-semiconductor contacts, No. 19 in Monographs in electrical and electronic engineering, Oxford: Clarendon Press.

[28] Colinge, J-P., Cynthia A. Colinge. (2005). Physics of semiconductor devices. Springer Science & Business Media.

[29] Sharma, B. L. (1984). Metal-Semiconductor Schottky Barrier Junctions and their Applications. Plenum Press.

[30] Sze, Simon M., Yiming Li, & Kwok K. (2001). Physics of semiconductor devices. John Wiley & Sons.

[31] Saito, A., Matsumoto, H., Ohnisi, S., Akai-Kasaya, M., Kuwahara, Y., & Aono, M. (2004). Structure of atomically smoothed $LiNbO_3$ (0001) surface. *Japanese Journal of Applied Physics, Part 1: Regular Papers and Short Notes and Review Papers*, *43*(4 B), 2057–2060. https://doi.org/10.1143/JJAP.43.2057

[32] Sanna, S., & Schmidt, W. G. (2017). $LiNbO_3$ surfaces from a microscopic perspective. *Journal of Physics Condensed Matter*, *29*(41), 413001. https://doi.org/10.1088/1361-648X/aa818d

[33] Tabata, K., Choso, T., & Nagasawa, Y. (1998). The topmost structure of annealed single crystal of $LiNbO_3$. *Surface Science*, *408*(1–3), 137–145. https://doi.org/10.1016/S0039-6028(98)00177-0

[34] Shur, V. Y., Akhmatkhanov, A. R., & Pelegova, E. V. (2016). Self-organizing formation of dendrite domain structures in lithium niobate and lithium tantalate crystals. *Ferroelectrics*, *500*(1), 76–89. https://doi.org/10.1080/00150193.2016.1229114

[35] Hölscher, R., Sanna, S., & Schmidt, W. G. (2012). Adsorption of OH and H at the $LiNbO_3$ (0001) surface. *Physica Status Solidi (C) Current Topics in Solid State Physics*, *9*(6), 1361–1365. https://doi.org/10.1002/pssc.201100534

[36] Ostendorf, F., Torbrügge, S., & Reichling, M. (2008). Atomic scale evidence for faceting stabilization of a polar oxide surface. *Physical Review B - Condensed Matter and Materials Physics*, *77*(4), 041405. https://doi.org/10.1103/PhysRevB.77.041405

[37] Hölscher, R., Schmidt, W. G., & Sanna, S. (2014). Modeling $LiNbO_3$ surfaces at ambient conditions. *Journal of Physical Chemistry C*, *118*(19), 10213–10220. https://doi.org/10.1021/jp502936f

[38] Yun, Y., Li, M., Liao, D., Kampschulte, L., & Altman, E. I. (2007). Geometric and electronic structure of positively and negatively poled $LiNbO_3$ (0001) surfaces. *Surface Science*, *601*(19), 4636–4647. https://doi.org/10.1016/j.susc.2007.08.001

[39] Yang, W.-C., Rodriguez, B. J., Gruverman, A., & Nemanich, R. J. (2004). Polarization-dependent electron affinity of $LiNbO_3$ surfaces. *Applied Physics Letters*, *85*(12), 2316–2318. https://doi.org/10.1063/1.1790604

[40] Sanna, S., Hölscher, R., & Schmidt, W. G. (2014). Temperature dependent $LiNbO_3$ (0001): Surface reconstruction and surface charge. *Applied Surface Science*, *301*, 70–78. https://doi.org/10.1016/j.apsusc.2014.01.104

[41] Johann, F., & Soergel, E. (2009). Quantitative measurement of the surface charge density. *Applied Physics Letters*, *95*(23), 232906. https://doi.org/10.1063/1.3269606

[42] Sanna, S., & Schmidt, W. G. (2010). Lithium niobate X -cut, y -cut, and Z -cut surfaces from ab initio theory. *Physical Review B - Condensed Matter and Materials Physics*, *81*(21), 214116. https://doi.org/10.1103/PhysRevB.81.214116

[43] Lushkin, A. Ye., Nazarenko, V. B., Pilipchak, K. N., Shnyukov, V. F., & Naumovets, A. G. (1999). The impact of annealing and evaporation of $LiNbO_3$ crystals on their surface composition. *Journal of Physics D: Applied Physics*, *32*(1), 22–28. https://doi.org/10.1088/0022-3727/32/1/005

[44] Vogel, U., Gemming, T., Eckert, J., & Oswald, S. (2014). Analysis of surface pre-treatment for SAW-substrate material ($LiNbO_3$) and deposited thin films of Ta/Ti using ARXPS. *Surface and Interface Analysis*, *46*(10–11), 1033–1038. https://doi.org/10.1002/sia.5430

[45] Choso, T., Kamada, M., & Tabata, K. (1997). The effects of heat treatments upon NO adsorption for a single crystal of $LiNbO_3$. *Applied Surface Science*, *121–122*, 387–390. https://doi.org/10.1016/S0169-4332(97)00340-1

[46] Hu, H., Ricken, R., Sohler, W., & Wehrspohn, R. B. (2007). Lithium niobate ridge waveguides fabricated by wet etching. *IEEE Photonics Technology Letters*, *19*(6), 417–419. https://doi.org/10.1109/LPT.2007.892886

[47] Argiolas, N., Bazzan, M., Bernardi, A., Cattaruzza, E., Mazzoldi, P., Schiavuta, P., Sada, C., & Hangen, U. (2005). A systematic study of the chemical etching process on periodically

poled lithium niobate structures. *Materials Science and Engineering B: Solid-State Materials for Advanced Technology*, *118*(1), 150–154. https://doi.org/10.1016/j.mseb.2004.12.088

[48] Wang, L., Wang, K.-M., Wang, X.-L., Chen, F., Jiang, Y., Jia, C.-L., Jiao, Y., Lu, F., Shen, D.-Y., Ma, H.-J., Ma, H.-J., & Nie, R. (2007). Selective etching in $LiNbO_3$ combined of MeV O and Si ion implantation with wet-etch technique. *Surface and Coatings Technology*, *201*(9-11 SPEC.), 5081–5084. https://doi.org/10.1016/j.surfcoat.2006.07.145

[49] Wang, T.-J., Huang, C.-F., Wang, W.-S., & Wei, P.-K. (2004). A novel wet-etching method using electric-field-assisted proton exchange in $LiNbO_3$. *Journal of Lightwave Technology*, *22*(7), 1764–1771. https://doi.org/10.1109/JLT.2004.829229

[50] Eliseev, E. A., Morozovska, A. N., Kalinin, S. V., Li, Y., Shen, J., Glinchuk, M. D., Chen, L.-Q., & Gopalan, V. (2009). Surface effect on domain wall width in ferroelectrics. *Journal of Applied Physics*, *106*(8), 084102. https://doi.org/10.1063/1.3236644

[51] Eliseev, E. A. (2015). The structure of a 180-degree domain wall near the surface of ferroics. *Ukrainian Journal of Physics*, *60*(7), 627–632. https://doi.org/10.15407/ujpe60.07.0627

[52] Lee, W. T., Salje, E. K. H., & Bismayer, U. (2002). Surface structure of domain walls in a ferroelastic system with a domain wall pressure. *Journal of Physics Condensed Matter*, *14*(34), 7901–7910. https://doi.org/10.1088/0953-8984/14/34/308

[53] Choudhury, S., Li, Y., Odagawa, N., Vasudevarao, A., Tian, L., Capek, P., Dierolf, V., Morozovska, A. N., Eliseev, E. A., Kalinin, S., Chen, L.-Q., & Gopalan, V. (2008). The influence of 180° ferroelectric domain wall width on the threshold field for wall motion. *Journal of Applied Physics*, *104*(8), 084107. https://doi.org/10.1063/1.3000459

[54] Daimon, Y., & Cho, Y. (2007). Cross-sectional observation of nanodomain dots formed in both congruent and stoichiometric LiTaO3 crystals. *Applied Physics Letters*, *90*(19), 192906. https://doi.org/10.1063/1.2737906

[55] Cho, Y., & Daimon, Y. (2006). Cross-sectional observation of nano-domain dots formed in congruent single-crystal LiTaO3. *Materials Research Society Symposium Proceedings*, *966*, 180–185. https://doi.org/10.1557/proc-0966-t09-03

[56] Tian, L., Vasudevarao, A., Morozovska, A. N., Eliseev, E. A., Kalinin, S. V., & Gopalan, V. (2008). Nanoscale polarization profile across a 180° ferroelectric domain wall extracted by

quantitative piezoelectric force microscopy. *Journal of Applied Physics*, *104*(7), 074110. https://doi.org/10.1063/1.2979973

[57] Reichenbach, P., Kämpfe, T., Haußmann, A., Thiessen, A., Woike, T., Steudtner, R., Kocsor, L., Szaller, Z., Kovács, L., & Eng, L. M. (2018). Polaron-mediated luminescence in lithium niobate and lithium tantalate and its domain contrast. *Crystals*, *8*(5), 214. https://doi.org/10.3390/cryst8050214

[58] Mitin, V. V., Kochelap V. A., & Stroscio M. A. (2008). Introduction to nanoelectronics: science, nanotechnology, engineering, and applications. Cambridge University Press.

[59] Voigtländer, B. (2015). Scanning probe microscopy: Atomic force microscopy and scanning tunneling microscopy. Berlin: Springer.

[60] Baranovski, S. (2006). Charge transport in disordered solids with applications in electronics. John Wiley & Sons.

[61] Nandi, U., Jana, D., & Talukdar, D. (2015). Scaling description of non-ohmic direct current conduction in disordered systems. *Progress in Materials Science*, *71*, 1–92. https://doi.org/10.1016/j.pmatsci.2014.12.001

[62] Staebler, D. L., & Wronski, C. R. (1977). Reversible conductivity changes in discharge-produced amorphous Si. *Applied Physics Letters*, *31*(4), 292–294. https://doi.org/10.1063/1.89674

[63] Kravchenko, S. V., Mason, W. E., Bowker, G. E., Furneaux, J. E., Pudalov, V. M., & Diorio, M. (1995). Scaling of an anomalous metal-insulator transition in a two-dimensional system in silicon at B=0. *Physical Review B*, *51*(11), 7038–7045. https://doi.org/10.1103/PhysRevB.51.7038

[64] Hipps, K. W., & Mazur, U. (1993). Inelastic electron tunneling: An alternative molecular spectroscopy. *Journal of Physical Chemistry*, *97*(30), 7803–7814. https://doi.org/10.1021/j100132a004

[65] Scudiero, L., Barlow, D. E., Mazur, U., & Hipps, K. W. (2001). Scanning tunneling microscopy, orbital-mediated tunneling spectroscopy, and ultraviolet photoelectron spectroscopy of metal(II) tetraphenylporphyrins deposited from vapor. *Journal of the American Chemical Society*, *123*(17), 4073–4080. https://doi.org/10.1021/ja0100726

[66] Kim, Y., Song, H., Strigl, F., Pernau, H.-F., Lee, T., & Scheer, E. (2011). Conductance and vibrational states of single-molecule junctions controlled by mechanical stretching and material variation. *Physical Review Letters*, *106*(19), 196804. https://doi.org/10.1103/PhysRevLett.106.196804

[67] Reed, M. A. (2008). Inelastic electron tunneling spectroscopy. *Materials Today*, *11*(11), 46–50. https://doi.org/10.1016/S1369-7021(08)70238-4

[68] Kim, Y., Hellmuth, T. J., Bürkle, M., Pauly, F., & Scheer, E. (2011). Characteristics of amine-ended and thiol-ended alkane single-molecule junctions revealed by inelastic electron tunneling spectroscopy. *ACS Nano*, *5*(5), 4104–4111. https://doi.org/10.1021/nn200759s

[69] Ratzenberger, J. (2022). Towards reproducible electronic transport properties in lithium niobate domain walls, Master's Thesis, Technische Universität Dresden, Dresden.

[70] A. S. Lofty. (2021). Investigation of the factors that affect the stability of enhanced domain wall conductivity in single-crystalline lithium niobate, Master's Thesis, Technische Universität Dresden, Dresden.

[71] Eliseev, E. A., Morozovska, A. N., Svechnikov, G. S., Gopalan, V., & Shur, V. Y. (2011). Static conductivity of charged domain walls in uniaxial ferroelectric semiconductors. *Physical Review B - Condensed Matter and Materials Physics*, *83*(23), 235313. https://doi.org/10.1103/PhysRevB.83.235313

[72] Shur, V. Ya., Akhmatkhanov, A. R., & Baturin, I. S. (2015). Micro- and nano-domain engineering in lithium niobate. *Applied Physics Reviews*, *2*(4), 040604. https://doi.org/10.1063/1.4928591

[73] Turygin, A., Alikin, D., Alikin, Y., & Shur, V. (2017). The Formation of Self-Organized Domain Structures at Non-Polar Cuts of Lithium Niobate as a Result of Local Switching by an SPM Tip. Materials, 10(10), 1143. https://doi.org/10.3390/ma10101143

[74] Gambhir, S., Arvind, & Singh, M. (2018). Intrinsic Nonlinearity of a PN-junction Diode and Higher Order Harmonic Generation. *Physics Education* 34 (2), 3.

Acknowledgment

I gratefully acknowledge the following people for their numerous contributions to this work:

- **Prof. Dr. Lukas Eng**, for promoting the topic of domain wall conductivity and supervising this thesis.
- **Dr. Elke Beyreuther**, for the enormous amount of work she had done during discussions of the content of this work and its revisions and corrections, and her constant support.
- **Dr. Michael Rüsing**, for sharing his extensive knowledge on the topic and helping with finding the direction of the experiments and their interpretation.
- **Prof. Dr. Holger Fritze**, for being the secondary reviewer of this thesis.
- **Manuel Zahn** and **Julius Ratzenberger**, for introducing me to the topic of the conductive domain walls in lithium niobate, teaching me the handling of numerous setups and equipment (including but not limited to the poling setup, cryostat, AC measurements setup, etc.), and constantly answering my questions and resolving the software problems.
- **Dr. Uliana Yakhnevych**, for conducting the lengthy annealing procedure of LNO crystals.
- **Dr. Lili Ding**, for showing me the basics of the AFM use and software for it, and for obtaining nice AFM scans used in this work.
- **Boris Koppitz**, for doing the CSHG images, presented in this work.

Eidesstattliche Erklärung

Hiermit erkläre ich, dass ich diese Arbeit im Rahmen der Betreuung am Institut für Angewandte Physik ohne unzulässige Hilfe Dritter verfasst und alle Quellen als solche gekennzeichnet habe.

Iuliia Kiseleva Dresden, 03.01.2023